Northumbria University
NEWCASTLE

An Integrated Open Source Acoustofluidic Platform using Surface Acoustic Waves for Biomedical Applications

Jethro Vernon

PhD

2022

An Integrated Open Source Acoustofluidic Platform using Surface Acoustic Waves for Biomedical Applications

Jethro Vernon

A thesis submitted in partial fulfilment of the requirements of The University of Northumbria at Newcastle for the degree of Doctor of Philosophy

Research undertaken in the
Faculty of Engineering and Environment

April 2022

Abstract

Surface acoustic wave (SAW) devices using thin film technology are increasingly used in lab-on-a-chip, point-of-care and a wide variety of biomedical applications, due to their multi-functionalities and low cost. These thin film devices not only have both acoustofluidic sensing and actuation functions, but also have been produced with commonly used semiconductor manufacturing techniques. These allow the acoustic devices to be made on many different substrates, such as aluminium plate and foils, glass, silicon, polymers and plastics, which provide a wide variety of properties enabling many new directions and opening up new applications.

However, acoustic wave technology still requires benchtop lab equipment and experienced operators to utilise these SAW devices because of a lack of hardware integration and autonomous control, resulting in a higher-cost system than the proposed platform. Most SAW interfacing setups are bulky and complex to use. There are currently many studies exploring the uses of mobile phones, cameras and attempting to use open-source electronics to generate and control acoustic waves. In this thesis, we combine SAW microfluidics and sensing with Raspberry-Pi hardware, making a full use of its digital imaging capabilities.

This thesis focuses on integrating surface acoustic wave devices and open-source hardware and software to overcome the challenges with a digitally controlled acoustofluidic platform. The aim of this modular platform is to perform acoustofluidic functions autonomously, such as droplet transportation, mixing, heating and sensing. The basis of this platform is a Raspberry Pi, together with piezoelectric thin films on metallic substrates, 3D printed housing and additional electronics for SAW device control. The setup is then used to demonstrate these functions applied in a variety of biomedical applications, such as disease diagnostics, breathing disorder monitoring and cell culturing.

Table of Contents

List of Figures

List of Tables

List of Abbreviations

AFM	Atomic Force microscopy
AlN	Aluminium Nitride
Ar/O_2	argon/oxygen
BaTiO3	Barium Titanate
BAW	Bulk Acoustic Wave
bpm	breaths per minute
CAD	Computer Aided Design
CMOS	Complementary Metal-Oxide Semiconductor
CSI	Camera Serial Interface
CSV	Comer Separated Variable
CVD	Chemical Vapour Deposition
Db	Decibels
DC	Direct Current
DI	Deionised
DMEM	Dulbecco's Modified Eagle's Medium
DSI	Display Serial Interface
FBS	Fetal Bovine Serum
GPIO	General Input Output Pins
GUI	Graphical User Interface

IDLE	Integrated Development and Learning Environment
IDT	Interdigital Transducers
KCF	Kernelized Correlation Filter
LAMP	Loop-mediated Isothermal Amplification
$LiNbO_3$	Lithium Niobate
LOC	Lab-On-A-Chip
MEMS	Microelectromechanical Systems
P/S	Penicillin Streptomycin
PBS	Phosphate Buffer Saline
PCB	Printed Circuit Board
PCR	Polymerase Chain Reaction
PDMS	Polydimethylsiloxane
PIV	Particle Image Velocity
PLD	Pulsed Laser Deposition
PSG	Polysomnography
PZT	Lead Zirconate Titanate
QCM	Quartz Crystal Microbalance
RF	Radio Frequency
SAW	Surface Acoustic Wave
SEM	Scanning Electron Microscope
SH-SAW	Shear Horizontal Surface Acoustic Wave

SPUDT	Single Phase Unidirectional Transducer
TCF	Temperature Coefficient of Frequency
USB	Universal Serial Bus
XRD	X-Ray Diffraction
ZnO	Zinc Oxide

List of Publications

List of journal and conference papers

- Ran Tao, Shahrzad Zahertar, Hamdi Torun, Yi Ru Liu, Meng Wang, Yuchao Lu, Jing Ting Luo, **Jethro Vernon**, Richard Binns, Yang He, Kai Tao, Qiang Wu, Hong Long Chang, and Yong Qing Fu "Flexible and Integrated Sensing Platform of Acoustic Waves and Metamaterials based on Polyimide-Coated Woven Carbon Fibers," *ACS Sens*, vol. 5, no. 8, pp. 2563–2569, 2020, doi: 10.1021/acssensors.0c00948.
- Yong Wang, Qian Zhang, Ran Tao, Dongyang Chen, Jin Xie, Hamdi Torun, Linzi E.Dodd, Jingting Luo, Chen Fu, **Jethro Vernon**, Pep Canyelles-Pericas, Richard Binns, Yong-Qing Fu, "A rapid and controllable acoustothermal microheater using thin film surface acoustic waves," *Sensors and Actuators, A: Physical*, vol. 318, p. 112508, Feb. 2021, doi: 10.1016/j.sna.2020.112508.
- **Jethro Vernon**, Pep Canyelles-Pericas, Hamdi Torun, Xuewu Dai, Wai Pang Ng, Richard Binns, Krishna Busawon, Yong-Qing Fu, "Acousto-Pi: An Opto-Acoustofluidic System using Surface Acoustic Waves controlled with Open Source Electronics for Integrated In-Field Diagnostics," *IEEE Transactions on Ultrasonics, Ferroelectrics, and Frequency Control*, pp. 1–1, 2021, doi: 10.1109/TUFFC.2021.3113173.
- **Jethro Vernon**, Pep Canyelles-Pericas, Hamdi Torun, Richard Binns, Wai Pang Ng, Yong-Qing Fu, "Apnoea-Pi: Sleep disorder monitoring with open-source electronics and acoustics," 2021 26th International Conference on Automation and Computing (ICAC), 2021, pp. 1-5, doi: 10.23919/ICAC50006.2021.9594073.

- Shahrzad Zahertar, Ran Tao, Hongzhe Wang, Hamdi Torun, Pep Canyelles-Pericas, Yang Liu, **Jethro Vernon**, Wai Pang Ng, Richard Binns, Qiang Wu, Jingting Luo, Yong-Qing Fu, "Integrated sensing and acoustofluidic functions for flexible thin film acoustic wave devices based on metallic and polymer multilayers," *IEEE Sensors Journal*, pp. 1–1, 2022, doi: 10.1109/JSEN.2022.3160282.
- **Jethro Vernon**, Pep Canyelles-Pericas, Hamdi Torun, Richard Binns, Wai Pang Ng, Qiang Wu, Yong-Qing Fu, "Breath monitoring, sleep disorder detection, and tracking using thin-film acoustic waves and open-source electronics," *Nanotechnol. Precis. Eng.* 5, 033002 (2022); https://doi.org/10.1063/10.0013471

List of conference and SIG meeting presentations

- Flash Presentation and poster, Droplets 2021, 16th to 18th August, Virtual Conference, Technical University of Darmstadt, Darmstadt, Germany
- Poster Presentation, Droplets 2019, 15th to 18th September 16th to 18th September, Durham university, Durham, UK
- Poster Presentation, 7th UKFN SIG Acoustofluidics Forum and Olympics, 26th and 27th June 2019, University of Bristol, Bristol, UK.
- Poster Presentation, Early Career Researcher Workshop 8th April 2019, Nottingham Trent university, Nottingham, UK

Acknowledgments

First, I would like to express my sincere gratitude to my principal supervisor, Prof. Richard Fu, for providing this great opportunity to pursue a PhD, and constantly providing strong support, regular communications and thorough guidance throughout my PhD study.

Secondly, I am extremely grateful for the continuous support of Dr Pep Canyelles-Pericas and Dr. Ran Tao. Pep initially helped before the start of my PhD, in mentoring me in the field and in laboratory procedures and has continued to provide periodic feedback and supervision during the length of this research. Throughout my PhD, both Pep and Ran have been invaluable by providing constant guidance in research and publication, a constant source of inspiration and in providing valued discussions on potential applications.

I am also grateful for my second supervisor Dr Richard Binns for his support guidance and discussions throughout the PhD, in addition to the five years previous support and guidance across my undergraduate degree. I appreciate all the academic supervision team (Dr. Xuewu Dai and Dr. Davina de Camargo Madeira Simoes Vogiatzis), my friend and colleague Christopher Markwell and the support staff that have been friendly and supportive.

Thank you to my Mom and siblings for their strong support and reassurance in helping me combat my dyslexia. A special thank you, to my late father who enabled my interest in engineering, providing me with many skills which are still useful to this day.

Finally, thank you to Northumbria University for supporting me in a studentship.

Author's declaration

I declare that the work contained in this thesis has not been submitted for any other award and that it is all my work. I also confirm that this work fully acknowledges opinions, ideas and contributions from the work of others. Any ethical clearance for the research presented in this thesis has been approved. Approval has been sought and granted by the University Ethics Committee on 30th August 2019.

I declare that the word count of this thesis is 29195 words.

Name: Jethro Moses Vernon

Date: 06/04/2022

Chapter 1. Introduction

1.1. Research motivation

Surface Acoustic waves (SAW) technology has found a wide range of applications in radio frequency (RF) filters for telecommunications and more recently sensing, acoustofluidics, lab-on-a-chip (LOC), and biomedical applications [1]. Recent developments in SAW materials have opened up the possibility of thin film and flexible devices [2]. Acoustic waves have unique advantages for lab-on-chip, and they are able to both actuate and sense. A sensor is used to detect changes of signals, which are understood as a stimulation or a process through which some physical variables of the device become different. The environmental variations are captured by the sensor and are usually outputs as an electrical signal, which can be recorded and processed [3]. An actuator is used to mechanically move parts of a system. For example, electric motors are actuators, as they convert electricity into mechanical torque. These can be used as a pump to move fluids or linear actuators, for example, to drive syringes for precise amount of liquids [4]. SAW can manipulate small samples of fluid (e.g., in a microlitre scale) [5]. SAW microfluidics includes advanced functions such as pumping, mixing, stirring, nebulisation and jetting, all of which are controllable with the input signal. Acoustic waves can be utilized for sample preparations such as cell sorting/separation, cell lysis, heating and polymerase chain reaction (PCR) [6][7]. Therefore, major sample preparation tasks could be completed solely based on acoustic waves [8][9][10][11]. This significantly reduces the complexity of the system by performing sample preparation and heating with the same device instead of separate mixing and thermal cycling machines. operation costs are also reduced because of less components required in the overall system and small quantities required to perform the same assays.

Most acoustic devices have been made from these bulk piezoelectric materials but are often expensive and cannot be easily integrated with electronics for control and signal processing. In addition, they are also generally brittle and fragile when polished into very thin structures for high-frequency applications. Recently, piezoelectric thin films including zinc oxide (ZnO) and aluminium nitride (AlN) have found a wide range of lab-on-chip applications These include pumping, mixing, nebulisation, jetting, biosensing, cell concentrating and patterning, [12].

Piezoelectricity is a phenomenon that an electric charge is produced when a mechanical stress is applied to a piezoelectric material. The piezoelectric effect describes the phenomenon where the non-centrosymmetric materials can generate electric fields under an external mechanical stress. It is a reversible process that the material will be deformed with an external electric field [3][4].

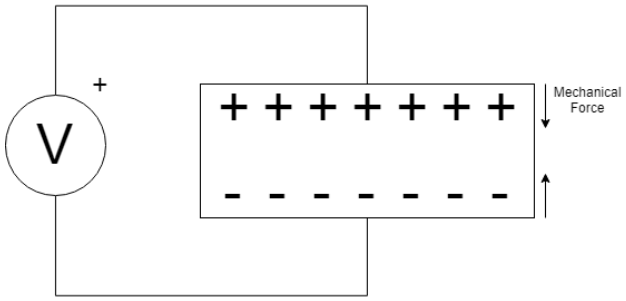

Figure 1.1 a piezoelectric material under stress producing electrical energy

There are both naturally occurring piezoelectric materials and manmade compounds. Some natural piezoelectric materials are crystals such as Quartz. Piezoelectric properties are also found in some organic materials such as bone, tendons and DNA [13]. A fibre-like structure of the protein collagen is found in found in bone and cartilage and is piezoelectric, when force is applied to the bone the collagen fibres slide past each other and generate charge

[14][15]. It is said that piezoelectricity in the bone potentially has a role in regeneration, alongside fluid flow to contribute to bone heling [16]. Some engineered piezoelectric materials are lithium niobate ($LiNbO_3$), zinc oxide (ZnO), aluminium nitride (AlN) and lead zirconate titanate (PZT).

Zinc oxide has found a wide range of lab-on-chip applications, due to its good semiconducting and piezoelectric properties [1]. It is used in electronics photonics, acoustic and sensing applications [17]. The basic structure of a ZnO Thin film SAW device that can be used for microfluidics and sensing consists of a substrate, a ZnO thin film layer and interdigital transducers (IDTs).

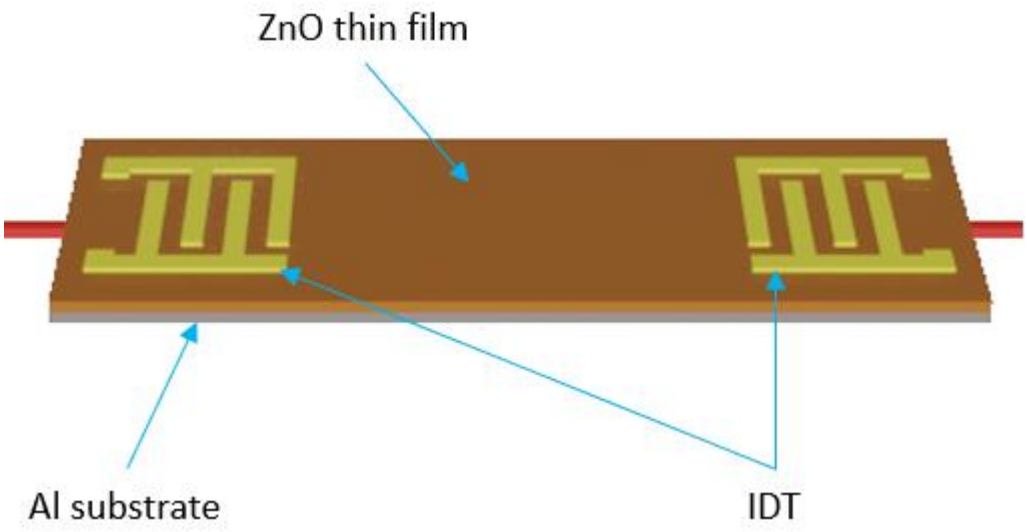

Figure 1.2 A common ZnO thin film SAW device, with a substrate, ZnO thin film and IDTs

Figure 1.2 shows a typical thin film SAW device. The substate could be one of many materials including, silicon, ceramics, glass, polymers and metals [12]. This study is mainly focused on using aluminium substrates of various thicknesses. Aluminium was chosen for its low cost, ease of manufacture and mailability especially for flexible/bendable thinner substrates. ZnO/Al substrates do not exhibit the problems of bulk substrates such as

inflexibility, brittleness, and difficulty to control different wave modes [18]. The next layer is the piezoelectric ZnO film that is grown on the substrate. Lastly, on the surface are the IDTs with the shape shown in Figure 1.2, and they are designed to generate an acoustic wave that propagates along the length of the substrate.

Devices such as the one shown in the Figure 1.2 and the other ultrasonic transducers such as PZT devices are being used in acoustofluidic and biomedical applications [19]. These methods have significant advantages compared with the conventional benchtop equipment, with reduced size and cost. These devices have also been shown to be able to manipulate much smaller sample sizes in microliters and with a lower amount of human contact. These advantages allow for lower sample consumption, an increase in the number of experiments or tests that can be performed and a reduction in human handling, thus reducing the likelihood of contamination and exposure to hazardous situations [20].

Researchers in these fields have begun to investigate more advanced and precise control of particles and droplets. These tasks are being performed with SAW devices or ultrasonic transducers to create standing waves so that particles are located in low pressure nodes. The movement is created by shifting the phases of the waves that interact with the particles. Such methods have employed cameras to track particles and create feedback loops, which enables more precise and automatic control of the position of microparticles or polystyrene beads [21][22]. These methods are focused on controlling small single particles such as biological cells and organisms. Some studies have also involved the combination of sensing and actuation to detect the position of a droplet and transport it to a new position in the X or Y directions [23]. They create a stage made of lithium niobate with IDTs surrounding an area of more than two inches across. They transmit waves that propagate across a large area and

are received by the opposite IDTs. If the waves are obstructed by the droplet, they will be severely attenuated, which can be used to reveal the position of the droplet.

Ultrasonic transducers are often operated at lower frequencies [19]. These devices are often integrated with mobile phones, Bluetooth speakers or microcontrollers and small scale PCs such as a Raspberry Pi [22]. Raspberry Pis are particularly interesting as they are small and low cost. They are fully functioning credit card sized computers, provided with a dedicated Linux operating system [24]. Often found in prototypes and makers projects, they are capable of a wide range of applications and useful for data-logging, processing information, graphical user interface management and internet of things integration. They can also be very easily interfaced with external electronics and equipment, such as sensors, actuators and benchtop lab equipment.

1.2. Aims and objectives

Whilst the SAW technology has seen significant advances in its ability to actuate and sense for biomedical applications, there still remains a gap in the research field whereby the hardware and software have yet to be integrated. The operation of current devices still requires experts with the knowledge to complete tasks with expensive laboratory equipment to hand. There is a critical need for low cost, but effective open source electronics for operation and control of such devices.

The key aim of this thesis is to develop a modular Raspberry Pi based platform capable of controlling SAW devices to perform the actuation and sensing functions required for multiple biomedical applications. This will include droplet movement, mixing and heating

as well as temperature and humidity sensing. ZnO thin film on aluminium substrates is to be the main device structure used and it is to be enhanced by raspberry pi functionality, such as external sensor and cameras being integrated, this enables laboratory equipment to be phased out achieving the goal of developing the field further in lab on chip and point of care devices.

In order to achieve this aim, I have the following objectives in this project:

1. Develop an integrated testbed involving electronics, optics and acoustics to apply to various biomedical applications
2. Explore the use of various ZnO on Al devices with various thicknesses and a range of IDTs
3. Study the ability for the system to manipulate various types of biological liquids
4. Use the platform to perform disease diagnostics, using PCR and Loop-mediated Isothermal Amplification (LAMP) based DNA amplification methods
5. Investigate the platform's ability to track breathing and detect sleep apnoea
6. Apply the platform for cell culturing, to create a cell growth and monitoring system

1.3. Thesis outline

This thesis consists of eight chapters. These describe the process, development and applications of the acoustofluidic platform.

Chapter One introduces surface acoustic waves, piezoelectricity, Raspberry Pi and opensource, and the aims and objectives.

Chapter Two expands on the introduction by reviewing the literature and introducing the theoretical background behind piezoelectricity and common materials, especially ZnO,

SAW actuation, droplet transportation, heating and mixing, as well as SAW sensing. The theory and background of opensource and Raspberry Pi are also explored and explanations of biomedical applications such as cell and tissue engineering, DNA and disease detection using PCR and LAMP, as well as sleep apnoea.

Chapter Three explains in detail the experimental methodology used during this research. This includes ZnO Thin film deposition, SAW device fabrication and characterisation. The development of the acoustofluidic platform and experimental setups for droplet transportation, mixing, heating and temperature, humidity sensing and breath tracking are introduced.

Chapter Four demonstrates digital acoustofluidics using the developed platform. Droplet movement, mixing and heating are discussed. This chapter also talks about the ability to control droplet movement on multiple axis, different liquids with various properties and SAW multiplexing.

Chapter Five evaluates the platform as it is applied to the application for in-field diagnostics. This involves performing all the required steps to complete PCR and LAMP diagnostics. Temperature control, thermal cycling and fluorescence detection are discussed.

Chapter Six looks at using the platform to analyse human breathing and detect sleep Apnoea. This involves the investigations of the effects of humidity and temperature during breath tracking. Development of algorithms to negate the environmental influences and detect breathing rates from the recorded data.

Chapter Seven applies the platform for cell culturing and explores the ability to control the SAW devices to stimulate cell proliferation. This chapter also investigates the SAW platform as an automated cell growth and monitoring system.

Chapter Eight is the final chapter that contains the conclusions and recommended future work.

Chapter 2. Literature review

This chapter contains the introduction of fundamental principles and review of surface acoustic waves and open source electronics, Raspberry Pi hardware, software and in-depth background for the relevant biomedical applications.

2.1. Introduction

The ZnO material has become popular because of its piezoelectric and semiconductor properties. A thin film of ZnO can be grown on a wide range of substrates and can be produced using semiconductor processes, creating the possibility of low-cost SAW devices [25]. As a result of the usages of ZnO films, flexible substrates and devices become possible, creating an influx of flexible, bendable and wearable SAW sensing devices being developed [26]. A range of different flexible ZnO thin film SAW devices have been explored and developed on substrates such as aluminium foil, polymers and plastics [12] and more recently polyimide-coated woven carbon fibres [27]. Aluminium foil allows for flexibility, good wave propagation and low cost, therefore preferred throughout this work.

Acoustic waves are generated by applying alternating current waveforms in the (Megahertz to Gigahertz range) to the IDTs dispirited on the surface of a piezoelectric material. The mechanical waves produced are useful and allow integrated LOC devices developed for diagnostic assays, tissue engineering, or drug development and delivery applications [28][29][30]. Different acoustofluidic functions in microfluidics, including generation, pumping, splitting, jetting, mixing and heating of droplets have been realised [12].

More recently various acoustofluidic functions are being developed with a more controlled approach, using electronics and software to precisely manipulate liquids or particles [23]. This can be used to develop new medical devices, replacing lab-based equipment, reducing the cost and increasing the portability [31].

In this chapter, I will review piezoelectricity, acoustic waves, thin film SAW devices alongside the open source technology with Raspberry Pi. I will also cover biomedical applications, such as cell culture, PCR, LAMP and breathing disorders.

2.2. Piezoelectricity and acoustic waves

2.2.1 Background

The word piezoelectric is derived from the Greek word “piezein” meaning press. The piezoelectric effect was first introduced in 1880 by the Curie brothers and the converse effect was mathematically proven by Lippman in 1881 [32]. Piezoelectricity is the ability to convert mechanical energy into electrical energy and also the reverse effect. Piezoelectricity is possible in certain materials and chemical compounds such as quartz, lithium niobate ($LiNbO_3$), zinc oxide (ZnO), aluminium nitride (AlN) and lead zirconate titanate (PZT). These materials have the ability to convert mechanical stress into electrical charge. This effect is also reversible meaning when a voltage is applied, the crystal lattice will be changed thus resulting in the deformation in the atomic structures [32]. The ability to convert electrical energy into mechanical energy and the reverse is known as the electromechanical

coupling coefficient. The electromechanical coupling factor (k^2) is written in the following equation [12].

$$K^2 = \frac{e_{31}^2}{C_{11}\,\varepsilon_{33}} \tag{2-1}$$

where e_{31}^2 is the electric field, C_{11} is the elastic constant of the material and ε_{33} is the permittivity at a constant strain.

Crystalline structures of the piezoelectric material are non-symmetrical, but with neutrally electrical charges [33]. However, when the material has an applied mechanical pressure, a charge is produced, and equally the reverse is possible. Figure 2.1 shows the principles for piezoelectric effects and charge states. Figure 2.1 (a) shows the piezoelectric material in an initial state where there is no electrical charge produced. Figure 2.1 (b) shows when a mechanical force is applied, a positive charge is generated which is able to be measured across the material. Figure 2.1 (c) shows a mechanical stress in the opposite direction producing a negative charge. Figure 2.1 (d) shows the converse effect. An applied voltage causes the material to be deformed. Figure 2.1 (e) shows that a negative charge being applied causes the material to be deformed in the opposite direction.

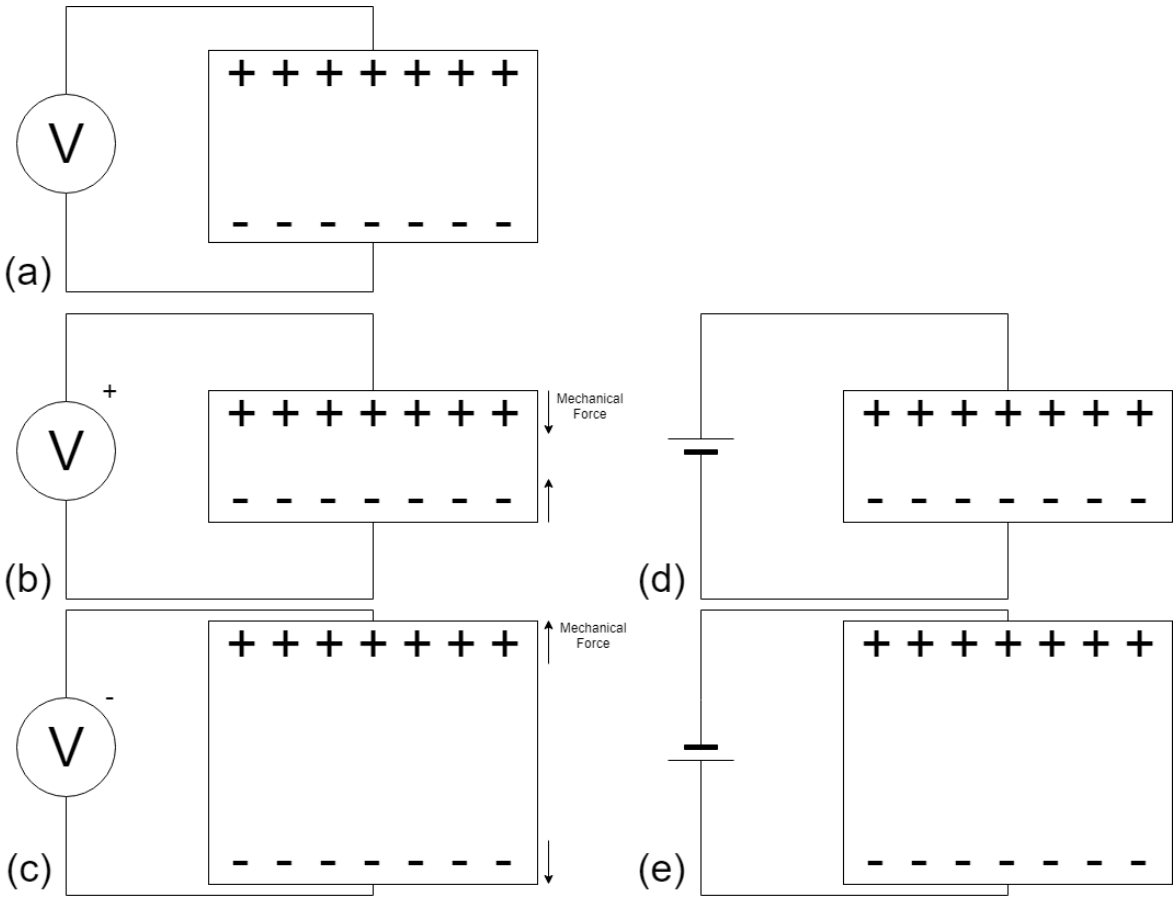

Figure 2.1. The principles for piezoelectric effects and charge states (a) piezoelectric material in equilibrium (b) Piezoelectric material under pressure producing potential difference (c) Being stressed in other direction producing a negative potential (d) Reverse effect of applying voltage to deform material (e) Applying an opposite polarity to deform in different direction

2.2.2 Piezoelectric Materials

For a material to be piezoelectric, it requires the non-symmetrical crystal structure to exhibit the piezoelectric effect properties [33]. There are a wide range of materials from crystals, biological, organic and engineered materials, which have piezoelectric properties. The first material that was discovered by the Curie brothers was quartz. One of the oldest applications of piezoelectricity was in World War 1 as the sonar. A quartz transducer was used to emit high frequency pulses into water, measuring the time taken for the reflections to return which enables the calculation of distance to objects [34]. More recent applications include observing mass changes by measuring frequency changes of a quartz crystal resonator

known as quartz crystal microbalance (QCM) [35], other materials include topaz and Rochelle salt. Rochelle salt was later used as a replacement for quartz in sonar applications due to its better electromechnical coupling coefficient [36].

Due to the special structure of many organic and biological materials, piezoelectric properties have been discovered in many of them. Some of these include cellulose (plant cell walls used in the manufacture of paper) [37], silk [38] which is being research for wearable thin film based pressure sensors[39], bone [40] being investigates in tissue engineering applications [41] and DNA used in biosensors generating electrical signals for analytical devices [42].

There has been a lot of research interest in engineering synthetic piezoelectric materials. The aim for synthesizing these materials is to outperform naturally formed piezoelectric materials with much better physical properties [43]. The physical properties of these materials include their better ability to convert between mechanical and electrical energy, their stability with changing environmental factors such as temperature and being reproducible, and their easy manufacture at low costs [44]. The first engineered piezoelectric material was barium titanate ($BaTiO_3$), which firstly gained practical interest in the 1940s due to its ferroelectric and piezoelectric properties [45]. Barium titanate is chemically and mechanically stable with low loss characteristics. It was firstly used in applications such as capacitors, and then the doped barium titanate was used in semiconductors, thermistors and piezoelectric devices [45], such as small microphones [46]. PZT was later discovered and used due to its good piezoelectric properties [47]. PZT has been found to have better properties when compared to barium titanate. It has a higher electromechanical coupling coefficient and curie temperature, which makes it more efficient and more stable, and also easier to fabricate at a

lower cost [48][49]. It has been used in a wide array of applications. One of the applications is the pressure sensor [50] made onto cantilevers for atomic force microscopy [51]. PZT has also been investigated for energy harvesting [52], which has been explored in the form of electricity generating flooring [53] and even dance floors [54]. One key biomedical application is ultrasound. Using a PZT device on the human tissues, the vibrations are sent through the human body, and the reflections are recorded and processed to create images inside, such as those used for scanning of unborn babies [55]. PZT thin films have been used with microelectromechanical systems (MEMS) and complementary metal-oxide semiconductor technology (CMOS), paving the way for small scale applications such as micro-robotics [56]. PZT can be deposited onto substrates such as silicon and used for actuation in microfluidic devices [57].

Environmental concerns were raised about lead based nanomaterials such as PZT [58], due to the toxicity of lead alternative materials, especially for biomedical and environmental applications [59][60]. Attractive alternatives to PZT are bismuth sodium titanate and alkali niobates. It was shown that these piezoelectric materials are stable but do not have the overall performance of PZT [61]. Another attractive alternative is the synthetic crystal of lithium niobate, used in high speed optical communication and RF frequency filtering in mobile phones [62]. Lithium niobate is also used in acoustofluidic and biomedical applications [12].

Other alternatives include thin films of ZnO and AlN, which have recently been developed for microfluidics and biosensing. They have found a broad range of lab-on-chip applications such as biosensing, particle and cell concentrating, sorting and patterning, pumping, mixing, nebulisation and jetting [12]. Integrated acoustic wave sensing/microfluidic devices have been fabricated by depositing these piezoelectric films onto several substrates such as

silicon, ceramics, diamond, quartz, glass, and more recently also polymer, metallic foils and bendable glass/silicon for making flexible devices. These thin-film acoustic wave devices have potential for implementing disposable or flexible lab-on-a-chip devices for various sensing and actuating applications [12].

2.2.3 Acoustic waves

Lord Rayleigh in 1885 firstly explained mathematically that an earthquakes energy travels via surface waves, traveling along the elastic solid surfaces [63]. The surface waves generated in earthquakes is traveling on the surface instead of bulk and allow the energy to be absorbed efficiently on the surface structures. This same principle is used on the nanoscale with ultrasonic wavelengths instead of the low frequency infrasonic oscillation produced during earthquakes. Acoustic devices are powered by alternating current waveforms, and a radio frequency signal is applied to the interdigital transducer, as shown in Figure 2.2.

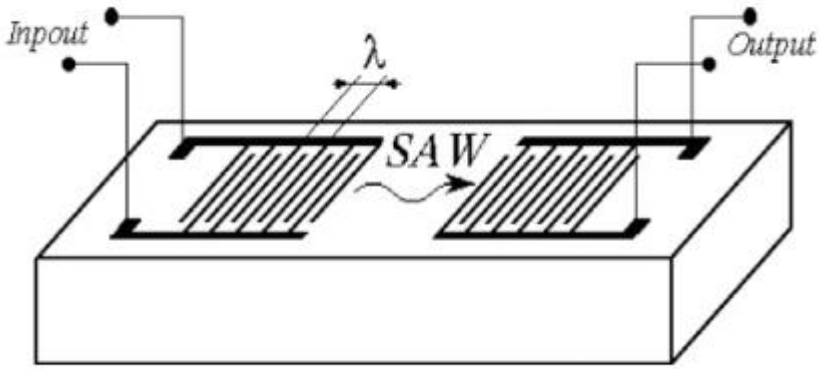

Figure 2.2 Surface acoustic wave device with input and output IDTs [12]

A mechanical wave is generated from the piezoelectric material. There are multiple types of acoustic devices [1]. When the wave propagates into the material, this is known as a bulk acoustic wave (BAW). Quartz crystal microbalances are the most common device used with bulk waves. For SAWs, the wave propagates along the surface of the substrate. This can be a vertical wave known as Rayleigh wave, a high energy wave with rapid attenuation with high absorption in liquid on the surface, or a shear horizontal surface acoustic wave (SH-SAW) [12].

Every acoustic device has a fundamental resonant frequency at which the device performs optimally. In the case of surface acoustic waves, both the IDTs and the substrate play roles in deciding this resonant frequency. The fundamental resonant frequency (f_r) can be calculated using the following equation:

$$f_r = \frac{v}{\lambda} \tag{2-2}$$

where v is the velocity of sound in the substrate and λ is the SAW wavelength. This is calculated by the distance between two IDT fingers[12].

The resonant frequency can be verified by the measurement using a vector network analyser. This is done by performing a frequency sweep and monitoring the reflected wave. The optimate frequency will have minimal reflections showing a large drop in reflected decibels (dB).

Acoustic waves were begun to be used in industry for communications and automotive applications since the 1960s [11]. White and Voltmer first proposed the IDT design in 1965, when they had a transmitting electrode connected to a pulsed oscillator and a receiver across a crystalline quartz bar [64]. Throughout the 1970s and 1980s, the IDT based SAW devices became increasingly used with higher frequencies above 1 GHz for sensing applications [65]. In 1977 Williamson reviewed 45 types of SAW devices that had been developed to identify the performance of each one [66]. These devices became very useful in military applications [67] and telecommunication and later in wireless communication [68].

A range of different IDT designs have been produced. Figure 2.3 shows a few key examples of the IDT designs. Figure 2.3 (a) is a typical design of IDTs with the addition of reflectors. Reflectors are among the electrodes and serve as a hard surface which reflect back some of the waves to increase the wave strength in the desired direction [69]. Figure 2.3 (b) is a split IDT, designed and used for reflecting back some of the waves. Figure 2.3 (c) is an angled or slanted design and changing the frequency will change the focused point along this IDT where the SAW waves enable the adjustment of streaming patterns in liquids or droplet movement. Figure 2.3 (d) is a curved design, which is able to create a focal point for the SAW energy. Figure 2.3 (e) is a single phase unidirectional transducer (SPUDT) design. This is an alternative method with the aim of amplifying the wave propagation in a single direction using internal reflectors within the IDT tunes to create a unidirectional wave. [1]

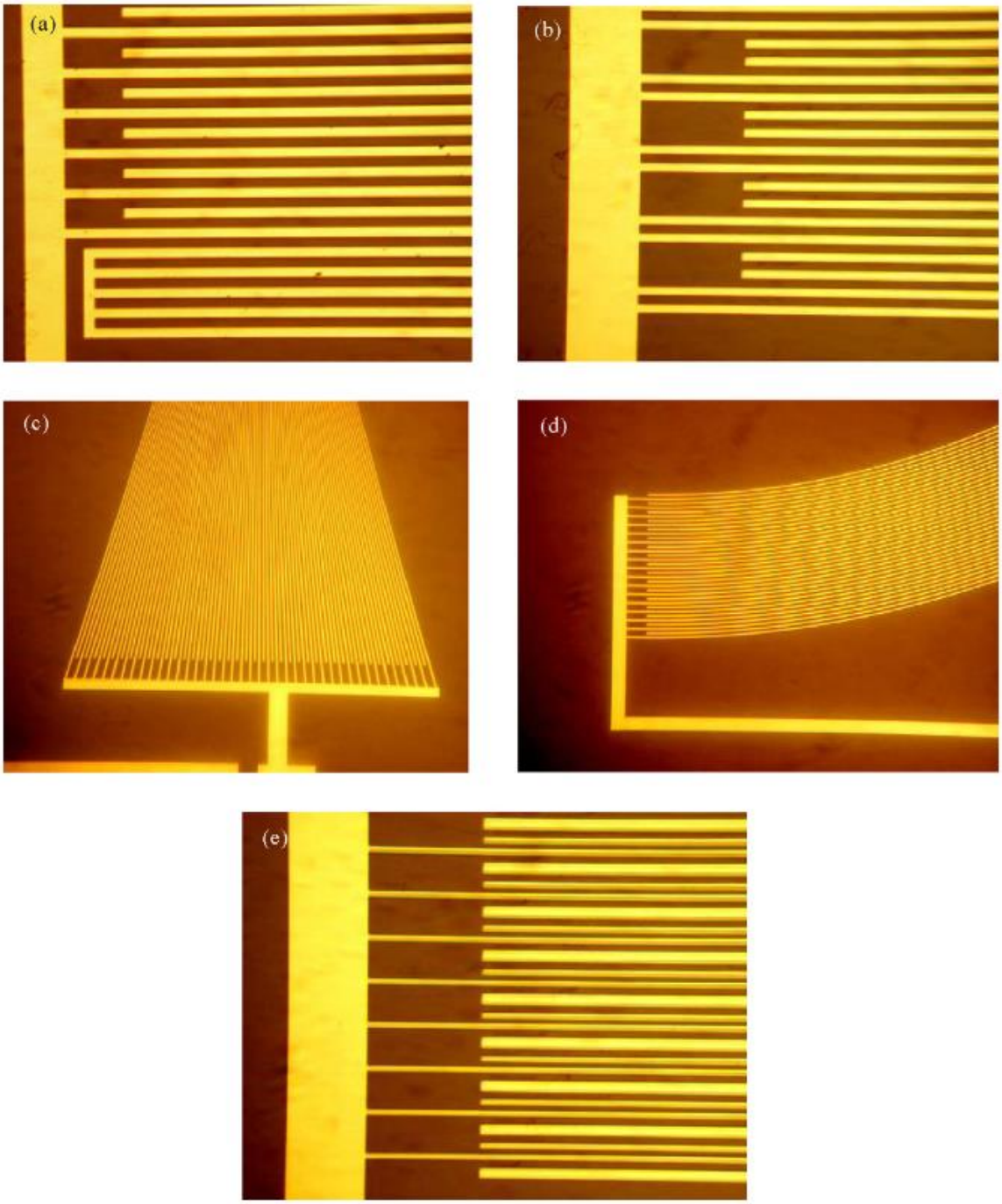

Figure 2.3 SAW IDT designs. (a) SAW IDT with reflector; (b) split IDT; (c) angled IDT; (d) curved IDT; (e) SPUDT IDT design [1]

2.2.4 Acoustofluidics

Acoustofluidics is a field that is a combination of acoustic devices and microfluidics. It is about the manipulation of small amounts of fluids in the range of 10^{-9} litres [70], often flowing in channels. SAW was first used to manipulate liquids in the 1980s [71]. It was discovered that when SAW propagates along a surface with a liquid droplet in contact, the energy would radiate into the liquid creating movements within the droplet. Additionally increasing the power beyond a threshold, the liquid would begin to move in the direction of the acoustic waves.

Figure 2.4 is an illustration of the interaction of surface acoustic waves propagating across a substrate and into a liquid droplet on top of the device. This shows the wave generated at the IDT and travel through the material, thus causing a streaming effect inside the droplet.

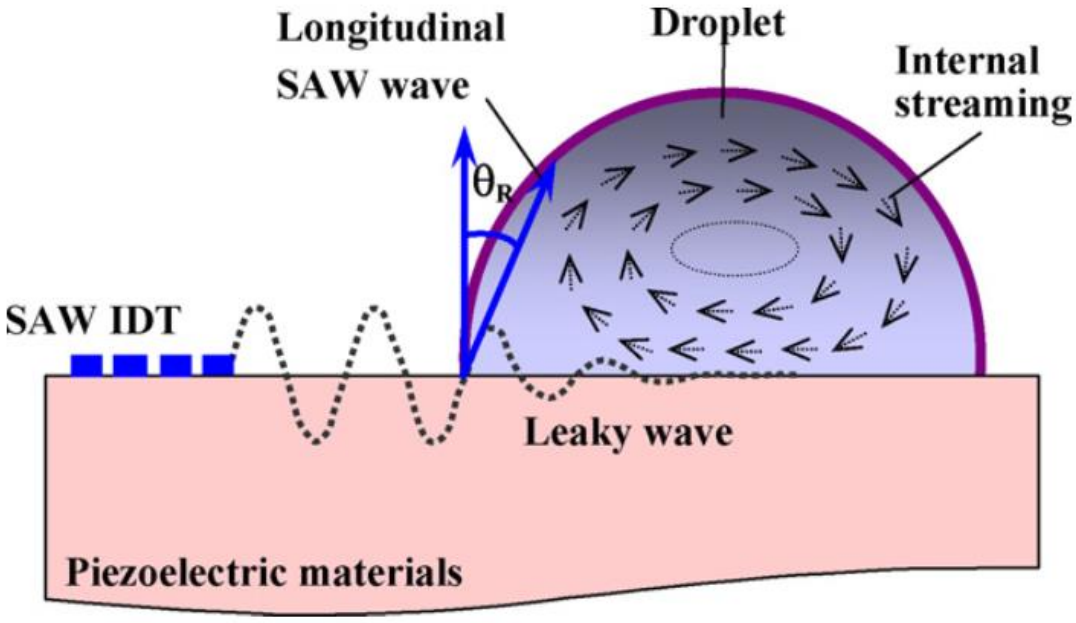

Figure 2.4 Interaction between propagating surface acoustic wave and a liquid droplet causing acoustic streaming inside droplet [1]

When a surface acoustic wave interacts with a liquid, the energy is transferred at a Rayleigh angle θ,

$$\theta = sin^{-1}\left(\frac{v_t}{v_s}\right) \tag{2-3}$$

where v_t is the velocity of the longitudinal wave in the substrate and v_s is the velocity of the longitudinal wave in the liquid[1].

A number of different acoustofluidic functions have been realised. These include, generation, pumping, splitting, jetting, atomisation, mixing and heating of droplets. Pumping is the movement of a body of liquid once the power has surpassed a threshold. Splitting is the ability for the SAW to manipulate the volume of droplets using the slanted-finger IDTs in a channel [72]. Jetting is the ability to propel the droplet from the surface of a SAW device. This requires a greater power to overcome a threshold where the energy not only moves the droplet but propels it away from the surface at the Rayleigh angle[12]. This requires a hydrophobic surface. Atomisation occurs when enough energy is put into a droplet on a non-hydrophobic surface, and thus it breaks up into significantly smaller droplets whilst travelling into the environment [1]. Mixing is the ability to create movement in the form of streaming inside a droplet, and this allows for different chemicals or particles to mix much like mechanically stirring a liquid on a smaller scale. When the SAW device is active, the movement also generates heat that is transferred in droplets on top of the device, enabling the ability to have small scale controllable heaters [73]. SAW heating is an important part of

a lab-on-a-chip system. Higher temperatures are often needed for reactions in biochemical analysis. This means that there is a demand for small scale integrated heating and temperature control [74]. When the SAW device is active the mechanical energy causes rapid temperature increases with a high input electrical power. Therefore, adjusting the power input to the device can vary the temperature of samples. The SAW heating can be integrated alongside other microfluidic functions such as pumping and mixing, making this a very useful tool for biomedical applications.

In recent years, interest has been raised surrounding biomedical applications and acoustofluidics. One particular application is using SAW at specific frequencies to target specific sized particles in a flowing channel. SAW was used to separate E. coli from blood cells sending them down separate micro channels [75]. Red blood cells separated from E. coli showed a 96% purity. Other applications include using SAW devices for micro scale mixing which is a difficult task with conventional mixing approaches [76]. Microscale mixing has been shown to mix proteins and enzymes for a reaction [77].

One research group used a mobile phone, a Bluetooth speaker and a sharp-edge based acoustofluidic device to move and mix droplets [70]. Modifying the Bluetooth speaker and connecting it to a device that operates at 6 KHz, they could send sinewaves generated by the mobile phone to induce acoustic streaming in a PDMS channel under a microscope [78]. Another group used mobiles phones with the attached macro-lenses to monitor particles in an acoustofluidic channel with a PZT acoustic device [19].

Multiple methods of using SAW devices have been used to control and manipulate small quantities of liquids. Using SAW devices can also generate waves in any direction surrounding liquids or particles, and this has been done with four IDTs equating to one pixel of a device, enabling large distance control in X and Y axis [20]. Another group used a camera, laptop and Matlab in a closed loop to move a trapped microparticle to the targeted location [21]. An alternative method of detecting a droplet position on a substrate was achieved by using the SAW devices themselves. In this method an array of five IDTs on each side of the substrate were used and emitted a wave that travelled from one side of the substrate to the other. If a droplet was in the path the wave would be obstructed indicating the location of the droplet [23][50]. Using flexible SAW device acoustofluidics has been proven to perform on curved and inclined substrates, propelling droplets around a loop and on the underside of a device [80].

SAW can be used for drug development and delivery [28][29][30]. This happens when a high power is applied to a SAW device, and the liquid applied to the surface can be atomised for drug delivery in the form of a mist that can be inhaled.

Another research group used surface acoustic waves to control the precise rotation of Caenorhabditis elegans, which are microscopic creatures that act as a parasite 1 mm in length [81]. Microfluidic devices using the SAWs and focused IDTs separated tumour cells from red blood cells [82]. $LiNbO_3$ SAW devices have been used to detect the position and manipulate droplets[23].

2.2.5 Sensing

SAW devices are sensitive to physical or chemical activities on the device's surface, such as temperature, UV and mass loading.

Temperature can be obtained from the changes of SAW device's resonant frequency, whether it is due to the changes in ambient temperature, using a heat source on the device or itself generating the heat. These all affect the material's properties that make up the SAW device. As states in equation (2.2), the frequency is dependent on two factors the IDT electrode spacing and the speed of sound through the material [83]. When the temperature is increased, the material expands increasing the distance between the individual IDT fingers and effects the speed of sound in the aluminium substrate increases. in most cases the SAW wavelength λ increases more than the speed of sound in the material, resulting in the resonant frequency lowering for the device [84][85]. SAW devices need to be characterised, by monitoring the frequency shift whilst the temperature is varied. The temperature coefficient of frequency (TCF) can be calculated as:

$$TCF = \frac{1}{f_0}\frac{\delta f}{\delta T} \tag{2-4}$$

where f_0 is the fundamental resonant frequency measured at room temperature, δf is the change in frequency and δT is the change in temperature [84]. A large TCF value is desirable for many cases for temperature sensing but might not be desirable for other types of sensing.

Acoustic wave device can be very sensitive to small mass changes, or a liquids density and viscosity [86]. One sensitive matter that can be easily accumulated on the surface of a SAW device is water vapour. The mass of water that can be held in the air is dependent on the air, known as relative humidity. When the water molecules are accumulated on a SAW device, the frequency of the device shifts. The higher the relative humidity, the lower the frequency shifts [87]. SAW devices with treated surfaces and reflectors have proven to boost sensitivity to relative humidity [88]. They have also been used to detect different microorganisms such as E. Coli [89] and particles or bacteria in flowing liquids [90].

2.3. Thin film based SAW devices

ZnO and AlN thin films have gained attention in a wide range of LOC applications. Some of these include particle manipulation, cell sorting and patterning, droplet manipulation and biosensing [12]. ZnO was found to be piezoelectric in the 1960s and later in the 1970s the first ZnO thin film SAW devices were produced. These thin films play a major role in the future of acoustofluidics and LOC devices, and they can be produced at lower costs and are not as brittle as the other SAW devices such as lithium niobate [91].

There are a wide range of thin film deposition methods, including direct current (DC) and RF magnetron sputtering, chemical vapour deposition (CVD) and pulsed laser deposition (PLD) [92]. ZnO has good properties for piezoelectric, acoustic and sensing applications. It has a better piezoelectric coupling coefficient compared to AlN. Good film crystallinity can be obtained without substrate heating, which makes deposition much easier. In addition, it has low film stress and good adhesion to most substrates including glass and polymers [27].

Natural Zinc resources are available for hundreds of years [93] and the material is also suitable for biomedical applications, with the major downside of the material being unstable when exposed to moisture over long periods of time, thus requiring a surface protection [12].

AlN on the other hand has good mechanical properties, allowing it to remain a stable piezoelectric material in higher temperatures. Due to its high wave propagation properties, it enables generation of higher frequencies, and is also suitable for sensing in a harsh environment [12]. AlN is however more difficult to work with, requiring higher temperatures for deposition.

2.4. Open source electronics

2.4.1 What is open source

Open source is a term used for something that is readily available for anyone to use, share and modify. In the 1990s open source started to emerge alongside the internet which became the main means of distribution, allowing for a global audience. This enables free software/hardware that can be globally distributed and aid others in their work and projects, thus reducing costs of licensing and copyright. Open source enables access to designs and source codes that are then modified into new versions to be applied in niche projects or systems that the original version was not suited [94].

2.4.2 Open source software

Software is used to interface and control the hardware and components that make up a system. These are programmed in editors which are converted to machine language using a compiler or interpreter and designed to run on specific computers or embedded systems. A

programmer produces code that is a set of numerical instructions. Then a computer follows to complete tasks. These instructions are running continuously behind the scenes on every application and operating system in order for them to function [95]. The term opensource software refers to applications and operating systems which are free to use, modify and redistribute. The modification allows for the user to modify existing work and adapt it to work with theirs, saving time and money from having to start from nothing. The free distribution allows for other to also access modified versions to use for further enhancement. Open source creates software with a potential for huge number of authors and versions to suit many different environments [96].

Python is an interpreted programming and object-orientated language, which means that python is focused on data instead of logic and function like the compiled language C [97][98]. Python is easy to use and quick for producing scripts. This makes python ideal for prototyping, datalogging and interfacing with components, sensors and benchtop lab equipment. Python supports modules, which are made to specific purposes and often made by the large community surrounding the language. Amongst these modules, there are some for the purpose of numerical data storage and manipulation [99], interfacing and communicating with equipment, processing images [100]. Machine learning and AI is readily available to implement [101].

Python modules are installed using pip, which is a repository that holds the majority of modules made by companies and the community. The python modules used throughout the projects are as follows:

- **OS.** Miscellaneous operating system interfaces, OS is used to perform operation system functions such as setting file paths as well as opening and closing files. This is mainly used for saving comer separate variable (CSV) files and config files [102].
- **Rpi.GPIO.** This module enables python to interface with the Raspberry Pi GPIO pins. Pins can be assigned as an input or output, then set or monitored within the program during operation. This is used to control external boards and sensors [103].
- **Kivy.** Kivy is an opensource cross platform GUI design module. This allows the creation of widgets such as buttons, text fields, dropdown menus and live graphs to plot data such as the temperature over time or a frequency spectrum. Kivy is used in every project as the intermediary between the user and the back end code, allowing operators without any python or programming knowledge [104].
- **Time.** Time is used where delays or counting in seconds is required [105].
- **Datetime.** Datetime is used in a similar way to the module time but has the function to return the exact date with attributes such as year, month, day, hour, minute, second and microsecond [106].
- **PySerial.** This module is fundamental in communicating with sensors and lab equipment using serial over USB. This allows ASCII characters in strings to be transmitted and received [107].
- **PyVISA.** PyVISA is a python package for easier interfacing with benchtop lab equipment. By incorporating the features from PySerial and the ability to communicate with GPIB RS232 and ethernet connections, PyVISA is able to search for available device from a range of manufacturers such as National instruments, Keysight, Agilent, Tektronix and Keithley. This handles the connection and in the event of a network error the reconnection automatically occurs once a device is selected from a list of devices connected [108].

- **OpenCV.** OpenCV is a computer vision library known for its ability to process images and live video. It contains hundreds of computer vision algorithms such as those used in object tracking and detection [70].
- **SimplePID.** This module is the implementation of a PID controller where input, outputs and the proportional, integral and differential values can be set [109].
- **OpenPIV.** This module is an opensource particle tracking program used for particle image velocity (PIV) and can show flow patterns and vortices [110].
- **Pillow.** Pillow is an image processing library allowing for colour and file format changes [111].
- **NumPy.** NumPy is a numerical computing module designed for python. This enables the creations and manipulations of complicated arrays and matrices [112].
- **Matplotlib.** This module is essentially similar to Matlab in the ability to create static, animated and interactive figures and data in python [113].
- **Pickle.** Pickle is the ability to convert python data into byte streams. In this case the binary files are used as config files, storing parameters such as PID values, frequency and camera setting for when a user reopens the GUI [114].
- **PyLepton.** This module is made by the company Lepton along with Flir as a development kit to communicate with their miniature thermal imaging camera [115].
- **Sys.** System-specific parameters and functions used to report and recording the system errors [116].
- **Decimal.** This module is used to correctly round decimal floating point arithmetic [117].
- **Threading.** This module is fundamental in running multiple operations in parallel and preventing the GUI from freezing during main loop operation. Threading is effective creating subprocesses in addition to the main process of the script. Without

it everything would have to happen sequentially, whereas in these projects a camera needs to be operated whilst graphs have live updates and droplets are manipulated [118].

- **Picamera.** This module is used to communicate with any Raspberry Pi camera connected in the CSI port and some USB webcams [119].
- **Pynput.** This enables keyboard functions and shortcuts to be usable in the running python scripts [120].
- **Collections.** This module offers alternative data types in containers, such as a convenient method to create an array with a max length and new data will displace the oldest value in the array [121].
- **Math.** This module provides access to mathematical functions [122].
- **Imutils.** Imutils has various functions for basic image processing [123].
- **Argparse.** The module provides the ability to use command line arguments in a python script [124].

2.4.3 Open source hardware

Hardware is the physical components that build up a computer or microcontroller. These consist of integrated circuits, one or more central processing units, dedicated graphics processing units, memory and many other external peripherals via USB such as mouse, keyboard and a display. Microcontrollers also include input/output connection to interface with components or other hardware [125]. Much like open source software, schematics and designs are put into an open source licence, which enables widespread adoption and adaptation of systems to suit specific applications.

Open source electronics and additive manufacturing are now being used to produce scientific equipment at a lower cost [126]. For instance, expensive syringe pumps have been designed and can be 3D printed with the use of open source libraries, this resulted in a lower cost to build below £100 [127].

2.4.4 Raspberry Pi, embedded systems and their applications

Raspberry Pi is a small and low-cost computer with a footprint with the size of a credit card [24], and it is used in prototyping and maker projects. The Raspberry Pi's first appearance was in 2012 after a British engineer previously worked on protypes of small computer for 6 years [128]. The idea was initially designed to combat high computer prices in the UK education system. The Raspberry Pi foundation was registered as an educational charity to help students learn programming, part of the name "Pi" is in reference to coding [129] [130] [131].

Raspberry Pi has great performance for its compact size and price, especially the most recent model 4b. Like a conventional computer, the Raspberry Pi has a universal serial bus (USB) port for connections of any devices including mouse and keyboard. It also contains an ethernet port for internet access, and USB-C for the power input. The Raspberry Pi also contains general input output pins (GPIO), which are the type of connections seen on microcontrollers for embedded systems and not commonly on complete computers. These open up a wide range of applications and components that can be integrated with the Raspberry Pi. Micro HDMI can be used for video output and USB for web cameras. Alternatively the Raspberry Pi also has ports commonly used in mobile phone applications for displays and cameras. These connections are called the Camera Serial Interface (CSI)

port and the Display Serial Interface (DSI) port [132][133]. The default operating system for the Raspberry Pi is Raspberry Pi OS formally Raspbian, and a free operating system based Debian which uses a Linux kernel. It is optimised to be used on raspberry pi hardware [134].

The original design was meant for prototyping and education [135]. Raspberry Pi however has an increasing market in commercial and industrial uses [136]. Raspberry Pi is being used for internet of things based automation at a low cost in industry [137][138]. The Raspberry Pi began to create devices for industry [139], and the foundation supplies another board known as the compute module [140]. This is capable of being embedded into products, specifically designed for industrial applications.

2.4.5 Potential for Interfacing and controlling SAW with opensource electronics

Advanced microscopy setups are currently being developed using open source (Raspberry Pi) platforms ([141][142][143][144][145]). Acoustofluidic research applications are starting to be implemented with open-source platforms, due to their advantages discussed in the previous section. One example is Ultraino, this system uses ultrasonic transducers in a phased array to suspend samples in a 3D space with applications in 3D particle manipulation and 3D images. This system uses an Arduino Mega with a driver board that connects many ultrasonic transducers, delaying the transmitted or received signals. The system is controlled using a computer connected to the Arduino, this performs the calculations to map the ultrasonic field, highlighting pressure nodes and then manipulating them to control the position of a sample [146].

In another electronic interfacing system [78], mobile phones are used to generate and amplify signals using Bluetooth-connected speakers connected to a piezoelectric transducer (e.g., PZT). These acoustic waves are used to induce acoustic streaming in a polydimethylsiloxane (PDMS) chamber. Images are then gathered using the mobile phone in a microscope setup [78].

Another open source acoustofluidic system [147] has applied a low cost multifunction system. This system works with audible frequency range devices controlled with Arduino microcontrollers and it is able to manipulate fluids flowing in microchannels while rotating particles. Multiple platforms have targeted portability as a key part into integrating these devices for real world situations. For instance, handheld acoustofluidics [148] to combat hurdles such as removing the need for benchtop lab equipment, miniaturizing and running the platform with battery power, but capable of mixing liquids, nebulization and particle alignment. One system in particular uses a Raspberry Pi to interface ultrasonic transducers [149] that are used to position small scale objects on water or free moving on a surface. However the feedback processing is made on a separate laptop running MATLAB software.

Python, commonly used with Raspberry Pi is very good for prototyping as libraries are readily available, quick and easy to implement. Being a high level interpreted language it automatically controls a lot of things such as memory management and communication between devices [150]. This however comes with some sacrifices to performance, and it is most notable when working with computer vision libraries as camera frame rates can be low and fluctuation is significant whilst performing object tracking. Alternative could be C which is compiles and would yield much higher frames rate. It would, however, take significantly

more time to implement as a lot more work has to be done behind the scenes to get fully functioning programs [150].

Raspberry Pi being a fully fledges computer makes it more powerful and better suited than Arduino for these applications. Arduino is simpler but would require an additional computer to communicate with it, setting up an interface would require much more work before the protype can function. Raspberry Pi with python allows for very quick control of instruments, sensors and GUI prototyping.

2.5. Biomedical applications to be explored with SAWs

Surface acoustic wave devices are increasingly applied in life science, biology, and point-of-care applications due to their combined acoustofluidic sensing and actuating properties. SAW energy can be transferred into a liquid in contact with the device's surface to generate different functions for bio-sampling and biosensing [78][19].

This following section describes some of the applications explored throughout this thesis.

2.5.1 Cell culturing

There are two cell lines that have been used in this study, therefore, we will discuss a bit more here. The first is a muscle cell, C2C12 is a myoblast line extracted from a mouse leg in 1977 by Yaffe and Saxel at the Weizmann Institute of Science in Israel in 1977 [151]. These cells have been very useful in biomedical research and studying cell cycles. and are capable of rapid proliferation. The cells are kept in Dulbecco's Modified Eagle's Medium

(DMEM) a widely used medium for supporting the growth of cells. They are grown on surfaces coated with fibronectin or Poly-lysine hydrobromide to promote adhesion [152].

The other type of cell is Normal Human Dermal Fibroblasts, which are extracted from human skin and used in various studies. These are responsible for tissue growth and wound healing [153]. This cell is cultured with the same method as C2C12. The cell care procedure is explained in the methodology section chapter 3.

2.5.2 PCR and LAMP

The most established techniques for medical diagnostics based on nucleic acid (DNA and RNA) detections are PCR and LAMP [154]. Both the PCR and LAMP facilitate biological reactions that result in exponential amplification of targeted DNA [155].

PCR is widely accepted as the gold standard diagnostic method of detection of viral DNA/RNA, including COVID-19 [156], whereas LAMP is emerging as an alternative technique that offers comparable performance [157]. The PCR requires thermal cycling processes between 60 to 90 °C for around 40 cycles [158][159] and use thermal cycles with vials that contain 200 to 500µl for the reaction often using Peltier's underneath to control the temperature [160]. meanwhile LAMP is an isothermal process, commonly involving a constant temperature of 65 °C in the region of twenty to thirty minutes [161][162][159]. SAW technology has been used to realise PCR and LAMP functions for detection of malaria [163], sexually transmitted pathogens [164] and salmonella [165][166][167][168].

For DNA detection, the reagents involve producing a bound marker that is typically fluorescent to be optically measured in real time during the amplification reaction. The luminescence level results in a positive or negative detection which is based on a predetermined threshold value. The markers that bind to the DNA are from a dye that is mixed among the reagents. Two common dyes are SYBR Green and Propidium Iodide [169]. Fluorescent materials have excitation and emission wavelengths. Fluorescence is the absorption of light by fluorophores. The additional energy creates an unstable state, then the excess energy is emitted as light in a different wavelength until it returns back to ground-state [170]. For SYBR Green the excitation wavelength is 497 nm with the excitation peak at 520 nm [171]. Propidium Iodide has the excitation and emission wavelengths of 535 nm and 617 nm [172].

2.5.3 Breath tracking and breathing disorders

Breathing is when the body moves air in and out of the lungs to exchange gases. The most important gas inhaled is oxygen, it is required for biological cells to operate. When cells produce carbon dioxide, this needs to be expelled during exhalation. Breathing is an important vital sign that needs to be tracked in order to monitor a patient's health. The number of times in one minute a person breathes is known as the respiration rate. The average respiration rate is 12 to 20 breaths per minute (bpm) [173]. Breathing can be tracked by counting the number of breaths in one minute or by flow-rate sensors and extracted from an electrocardiogram[174][175]. Breathing problems can cause a range of health issues, such as cardiac arrest and increased risks of a stroke [176].

Some of the breathing disorders include hyperventilation, which is when a person is breathing faster than normal, often due to emotional distress. This over breathing gets rid of too much carbon dioxide, thus causing dizziness and shortness of breath [177]. Other conditions are Bradypnea and Tachypnea where the person is breathing slower or faster than normal. These can prevent enough oxygen in the blood or be signs of limited air capacity in the lungs [178].

Apnoea is a sleep disorder that affects an increasing number of adults causing harm from fatigue to a growing chance of heart problems. Apnoea tracking is vital to help keep patients healthy. Sleep Apnoea can cause a number of conditions such as fatigue, high blood pressure, an increased risk of type 2 diabetes and can affect liver functionality. Apnoea is suffered by 2 to 4 percent of adult society [179]. There are two types of sleep Apnoea. The first one is obstructive sleep apnoea [176], which occurs when the muscles in the throat relax causing the airways to narrow while preventing enough air to keep adequate oxygen levels. The second one is less common and called central sleep apnoea [180], which happens when the brain fails to send signals to the muscles required for breathing causing shortness of breath. It is also possible to have both types of apnoea simultaneously.

Polysomnography (PSG) is commonly used for diagnosis of sleep disorders. It is a comprehensive technique that monitors brain waves, blood oxygenation, heart rate and limb movements during sleep. This results in a complex setup where the patient wears multiple sensors overnight, typically spent in a clinical facility [181]. Multiparametric sleep monitoring presents several disadvantages such as discomfort of use and the impossibility of home monitoring. Complementary technologies are being implemented such as wearable sensors [182] [183], or other sensors for breath pattern monitoring during sleep [184] [185].

New unobtrusive technologies are being developed to improve patient comfort and facilitate home use, including the use of cameras for video-based photoplethysmography and near-infrared temperature measurements [186] [187]. These approaches lack an effective gas flow sensor to match the recorded data with breathing patterns.

Surface Acoustic Wave devices have been used for respiratory monitoring applications [1][188][189], the principles are based on the mass loading and temperature changes. SAW device have demonstrated fast response and good sensitivity [190], including devices fabricated with thin film piezoelectric approaches [12]. Recently we have developed a platform that combines SAW with open-source electronics using Raspberry Pi [191], with potential to be used for sleep disorder diagnostics and monitoring [192]. The platform includes thermal and standard imaging that could integrate video-based photoplethysmography and near infrared monitoring.

2.6. Summary

SAW devices are increasingly applied in life science, biology, and point-of-care applications. However, there are critical issues such as lack of the ability to interface with hardware to meet real word applications and facilitate them with high performance and low cost. Therefore, in this work, I will focus on these areas.

1. An opensource platform using surface acoustic waves for in field diagnostics controlling multiple droplet functions to meet the requirements to perform PCR and LAMP
2. A cell culturing platform that can increase proliferation and automate cell counting.
3. A system that is capable of monitoring patient breathing at a low cost and portable.

Chapter 3. Experimental methodology

3.1. Thin films and SAW devices

3.1.1. Thin film deposition and characterisation

ZnO is the piezoelectric material used for the SAW devices due to the potential low cost deposition on substrates such as aluminium. ZnO film was deposited on either plate of 1.6 mm thickness or foil 50 μm thick made from aluminium. This was done using a physical vapour deposition (PVD) method, e.g., sputtering. A Nordiko direct current (DC) magnetron sputtering system was used with a zinc target with 99.99% purity for a high quality deposition. Aluminium plate with an area of 10 cm^2 was put into the puttering machine on the holder for sputtering. When foils were used, they were placed on glass wafers and secured with Kapton tape. The surfaces of foil and plates were cleaned with acetone, which then removed by ethanol, rinsed with deionised (DI) water and dried with nitrogen. The aluminium wafers were placed 20 cm away from the targets and the holder was rotated at 4 rpm. A flow of argon/oxygen (Ar/O_2) with a ratio of 10/15 mixture was generated with the gas pressure at 4 mbar and the DC power at 400 W. This deposition would achieve a uniform film at the rate of 5.6 nm/min with a thickness of the ZnO film at 10 μm. These parameters for the deposition process were chosen based on the surface quality and film thickness.

The surface morphology and images of the cross section were captured using the scanning electron microscope (SEM). The ZnO thin film orientation, structure and crystallinity were characterised using x-ray diffraction (XRD). The ZnO thin film surface roughness was characterised using atomic force microscopy (AFM).

3.1.2. SAW device fabrication and characterisation

Once the ZnO thin film was deposited the next step to create the SAW device was the creation of the IDT. The IDT is either an aluminium or gold electrode, sputter coated to a thickness of 200 nm and prepared using conventional photolithography and lift-off processes. The IDTs were designed using computer aided design (CAD) software to create a mask to transfer the patterns on the device wafer. The samples were cleaned with acetone, by ethanol, rinsed with DI water and dried with nitrogen. A photoresist (S1813 Rohm and Haas) was applied to the surface of the device using spin-coating with the Laurell 650M spin coater. The procedure was 10 rpm for 10 seconds, then constantly accelerated by 3,700 rpm for 60 seconds. The devices were then placed on a hot plate for the soft bake. This was set to a temperature of 95 ^{o}C for up to 10 minutes for foil samples. The mask (shown in Figure 3.1) was then placed on the sample using the EVG620 mask aligner with an exposure of 90 mJ dose. The next stage was required to use MF319 developer solution for 1 minute to develop the applied photoresist. After this, the sample was rinsed with DI water and dried with nitrogen. The photoresist patterns were checked under a microscope for defects.

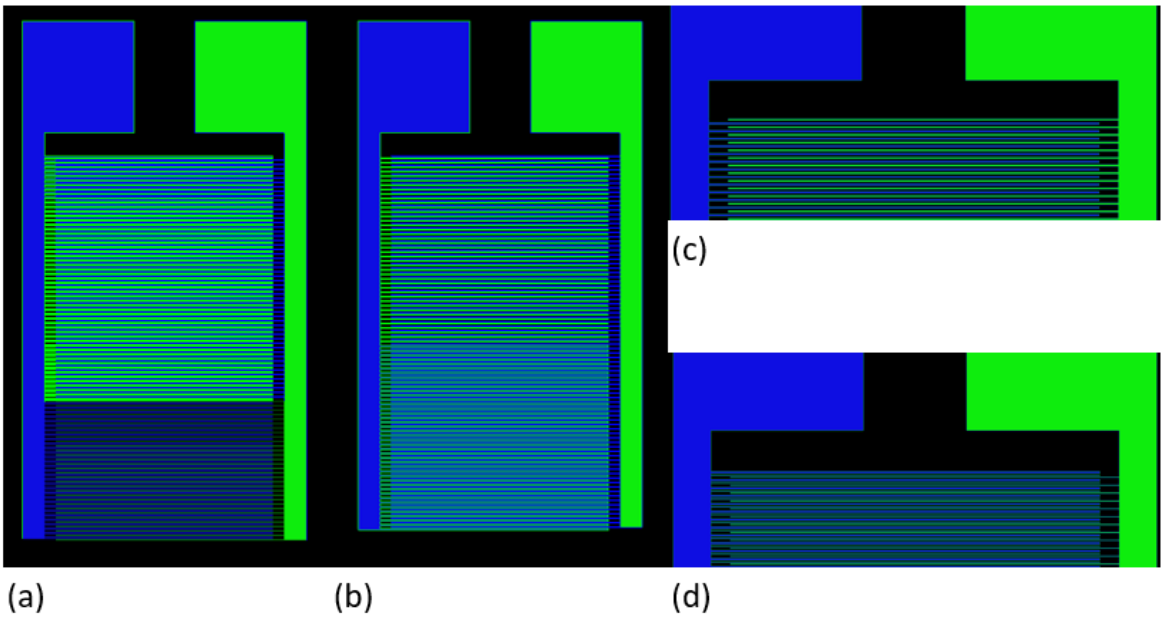

Figure 3.1 IDT design mask (a) 200µm (b) 200µm SPUDT (c) magnified view 200µm (d) magnified view 200µm SPUDT. Mask designed by Pep Canyellas Pericas

This mask (Figure 3.1) was 5 inches in height and length and had 6 designs of IDTs. The main difference between these devices was the frequency at which they were designed to operate. The most commonly used devices throughout the work were 200 µm with 84 pairs of fingers and the SPUDT 200 µm design, with an aperture of 5 mm. These operated at approximately a 14 MHz Rayleigh wave. The designed SAW IDTs also faced one another to allow liquid actuation in multiple directions and sensing through S21 transmission across the delay line area.

The samples were then placed in a Moorfield electron beam evaporation cluster system with a pressure of 2×10^{-7} mbar. This was used to deposit an Al or gold (with Cr as adhesion layer) IDTs with a thickness of 200 nm or 80 (20) nm. The sample was submersed in acetone solution for several minutes, then lift-off was performed in an ultrasonic bath. Sometimes the samples were required further rubbing with acetone to remove the remaining photoresist

that remained in deeper scratches. The samples were once again rinsed with ethanol, DI water and then dried with nitrogen.

The aluminium plate samples have a higher yield when compared to foil samples. The foil has more defects, higher surface roughness and easier to damage and scratch. This has an effect on the ZnO thin film and the IDTs on the substrate. Defects in the IDT reduce the quality of the acoustic wave, resulting in less efficient devices. After examination, the devices were split from one another on the large wafer. Plate samples required the use of a metal guillotine whilst foil samples were cut with scissors. The devices were electronically measured using a vector network analyser (Keysight N9913A FieldFox portable vector network analyser). The frequency spectra of the devices were measured. The S parameters of the SAW devices were recorded. S11 is the most common S parameter used throughout this work often used for characterising RF electronic circuits. This measures the input reflection coefficient using a single network analyser port on a singular IDT. A frequency sweep with a range near the estimated frequency is performed. The frequency at with there is minimal reflected voltage (shown as a trough in dB as the frequency sweeps) is considered the fundamental resonant frequency of the device at room temperature. S21 is the forward voltage gain, a signal is sent from port 1 and measured at port 2, transmitted from one IDT a mechanical wave is received by another across the substrate. Again, a frequency sweep is performed and the point where minimal loss has occurred (revealed as a peak in the recorded spectrum) is the optimal frequency to operate at. Other S parameters include S12 reverser voltage gain, transmission from port 2 to port 1 and S22 output port reflection coefficient [193][194].

3.2. Hardware design and building

A platform was developed as a basis for each application. The backbone of the testbed was a Raspberry Pi. Initially a raspberry pi model 3 b+ was used and later it was exchanged for the model 4 b for applications required more processing power such as those involving computer vision image processing. A comparison of both modules used is shown in Table 3.1. Raspberry pi was chosen for the performance with its low cost, ease of use with a wide community available for support and readily integrated OS and Python. It allowed for the control of hardware using the GPIO pins and USB, with the possibility to store, process and transmit data to the cloud or other devices. Both models of Raspberry Pi were used with open source electronics and bench top lab equipment to create a modular system that can be adapted for the target applications.

Table 3.1 Raspberry Pi model 3 b+ and 4 b specification comparison

Raspberry Pi Model	RPi model 3 B+	RPi model 4 B
CPU	ARM Cortex-A53	ARM Cortex-A72
CPU	4 × 1400 MHz	4 × 1500 MHz
RAM	1GB - LPDDR2	1GB, 2GB, 4GB, 8GB - LPDDR4
Wifi	2.4GHz and 5GHz	2.4GHz and 5GHz
Bluetooth	Bluetooth 4.2	Bluetooth 5.0
Wired connection	Gigabit Ethernet (max 300Mbit/s)	Gigabit Ethernet
GPIO	40 pin header	40 pin header
Video out	HDMI at 1080p DSI display port	2 × micro-HDMI at 4K 2-lane MIPI DSI display port
Camera	CSI port	CSI port

	USB webcam	USB webcam
USB	4 × USB 2.0	2 × USB 2.0 2 × USB 3.0
Storage	Micro SD port	Micro SD port

3.2.1. Digital Acoustofluidics and in-field diagnostics

The first aim of the platform is to manipulate droplets using surface acoustic wave devices and further adapted to integrate fluorescence and temperature control. An illustration of the setup is shown in Figure 3.2. In this version of the testbed the Raspberry Pi was upgraded to the model 4 b when it was released during the year 2019. The Raspberry Pi was connected to a signal generator (Tektronix, AFG1062) and microfluidic pump (Cellix, ExiGo microfluidic syringe pump) via USB. The signal generator was connected to two amplifiers (Mini-Circuits ZHL-20W-13+), which was amplified and connected to RF switches (Teledyne CCR-33S1O) capable of switching the high power to one of four IDTs (Figure 3.2).

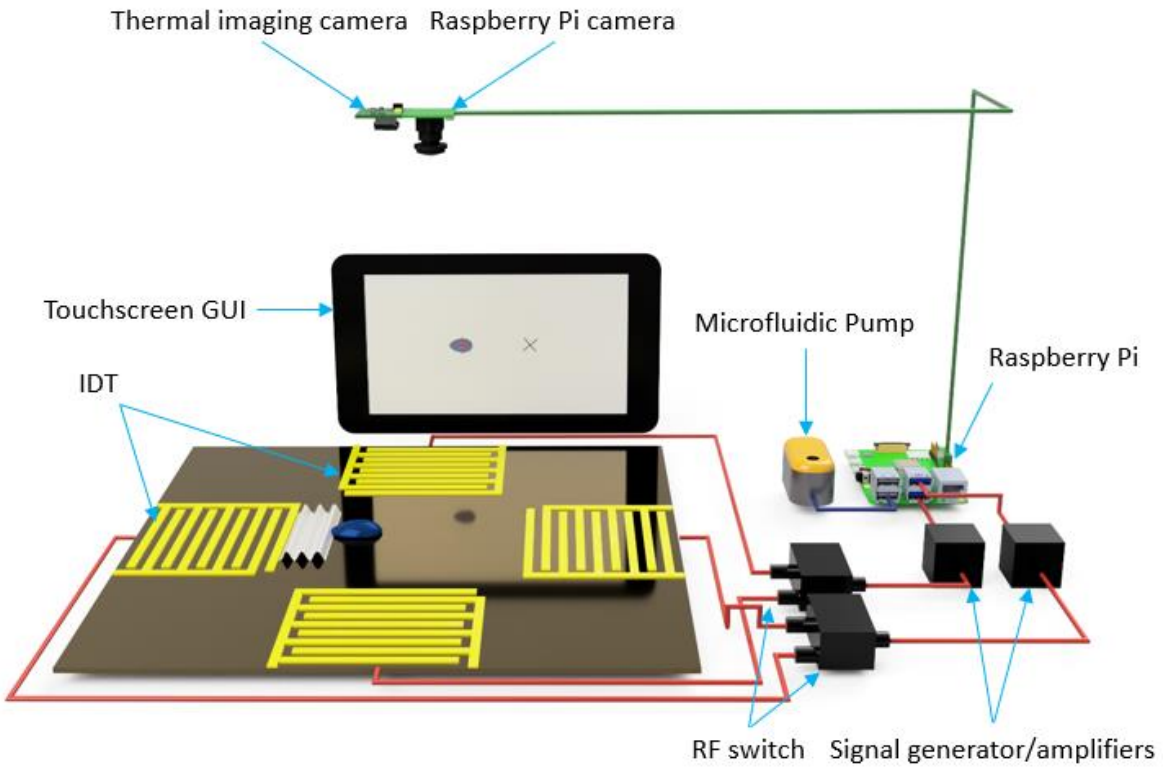

Figure 3.2 An illustration of SAW platform integrated with a Raspberry Pi controlling signal generators, amplifiers, RF switches, visible and thermal cameras interfaced through a touchscreen [191]

A Raspberry Pi camera (Raspberry Pi Camera Module V2) was connected using a ribbon cable to the Camera Serial Interface (CSI) port. A touchscreen display (Official Raspberry Pi 7") was used with a Display Serial Interface (DSI) port. A monitor was connected to HMDI. A mouse and keyboard were connected to USB ports in the programming or debugging setup. A thermal imaging camera (Flir Lepton® Series model 2.5) socketed in a breakout board (FLIR Lepton® Camera Breakout Board v2.0) was connected to the GPIO pins. The pinout is displayed in Figure 3.3 where the clock, data and power are connected. GND and Vin were used for the supply of 3.3 V, and CS pin was used to set the camera to a slave. The CLK and SCL were the clock pins required in serial communication. MOSI and MISO were used for sending data from master to slaves and slave to master. Finally in this setup in order to control which SAW device was active, the RF switches were controlled by

sending high and low signals from GPIO pins. The relays required a 12 V supply which was switched using transistors where the base was supplied with 3.3 V. UV LEDs were connected to the 5 V pin and GND (Figure 3.3).

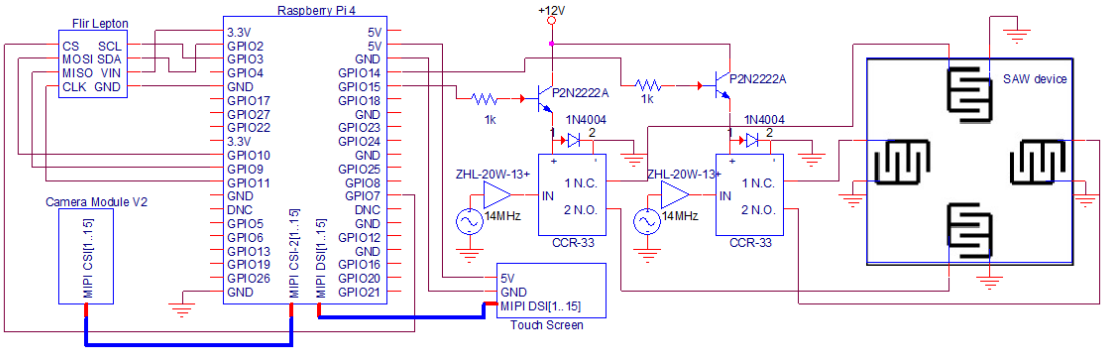

Figure 3.3 Circuit diagram of Raspberry Pi pinout and SAW control using an RF switch [191]

Costume 3D printed part was designed in Solidworks and printed using a 3D printer (Creality Ender 3 pro). Thor labs optical bench was used alongside parts designed by Thor labs, which were compatible to secure components such as the visible and thermal cameras in place above the SAW substrate (Figure 3.4 (b)). A 3D structure was designed to hold the substrate in place and provided electrical connection through spring loaded pins and custom printed circuit boards (PCBs) designed in Eagle AutoCAD. This allowed four IDTs to be connected for droplet actuation and multiple directions on the substrate in the central position between all IDTs, as shown in Figure 3.4 (c). SMA or BNC cables and connectors were used among the signal generator, amplifiers, RF switches and the SAW device mounting PCBs. Five UV LEDs and resistors were mounted on a circuit board and pointed at the droplets and powered by 5 V output from the Raspberry Pi GPIO (Figure 3.4 (a)).

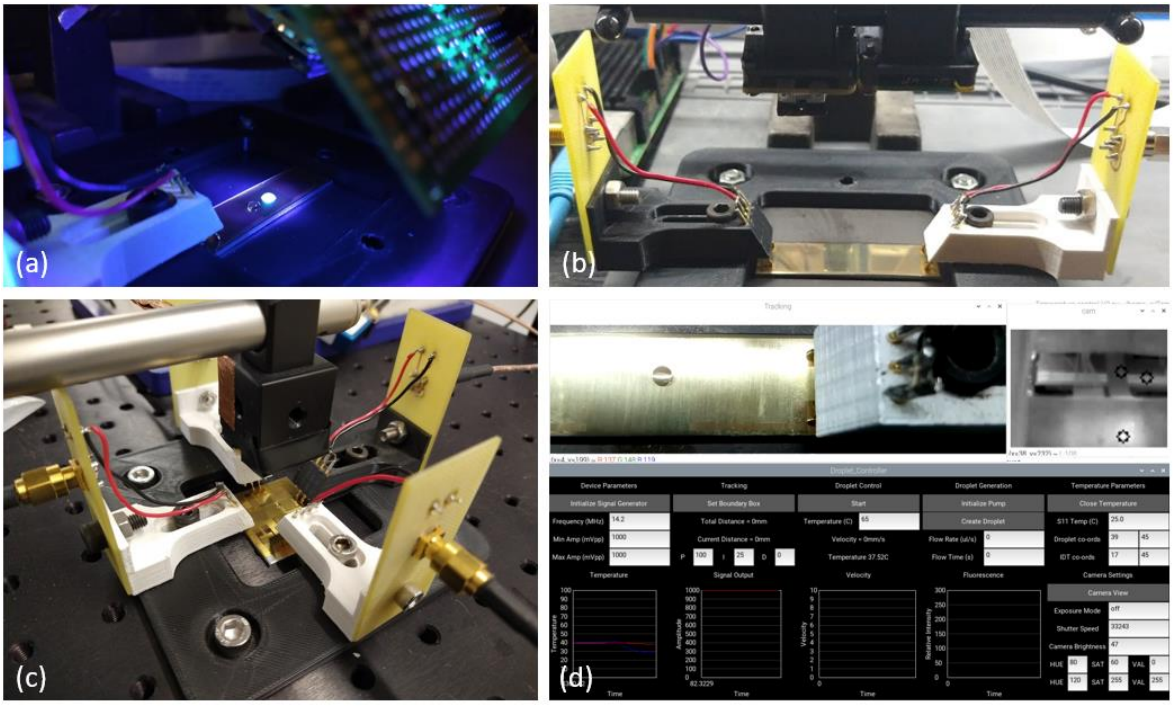

Figure 3.4 (a) Fluorescent droplet on SAW device (b) single axis two IDT SAW device and 3d mounted cameras (c) 2 axes 4 IDT mounted SAW device (d) GUI as seen on screen in overall setup [191]

Applications of Digital Acoustofluidics are explored in Chapter 4 and Chapter 5

3.2.2. Breath analysis and Apnoea detection

The platform for breath analysis had the same underlying core components as with the previous setup. The system used a Raspberry Pi, model 4, as embedded processor. The SAW device was used to measure humidity in the form of water vapour from the user's nose. The device was mounted with the same device holder shown in Figure 3.4 (b) and is shown in Figure 3.7. Optionally, the devices had small wires bonded to the electrode pads using silver paint or silver epoxy (MG Chemicals 8331 Liquid Adhesive). This was performed by securing the device and wires in place using a soldering helping hand tool, then applying silver paint to the pad and leaving to cure.

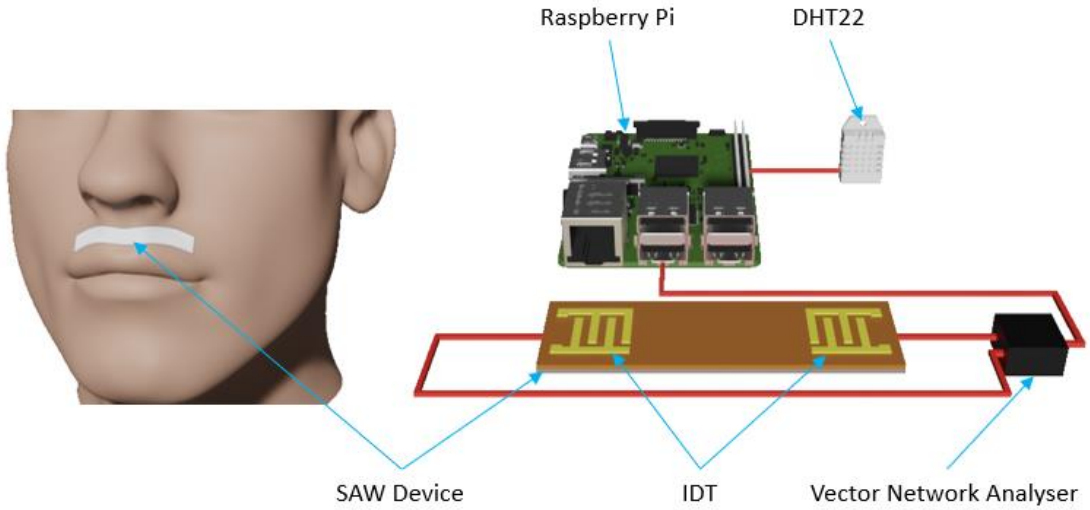

Figure 3.5 Illustration of the proposed Apnoea-Pi Platform [192]

A combined humidity and temperature sensor (DHT22) was integrated with a DATA pin to the GPIO pins for serial communication. VDD and GND were applied with a 3.3 V supply (Figure 3.6) and were used to monitor ambient changes. A vector network analyser (Keysight FieldFox Handheld RF and Microwave Network Analyzer) was connected via the ethernet port. The SAW device was connected in the same methods as shown in Figure 3.7.

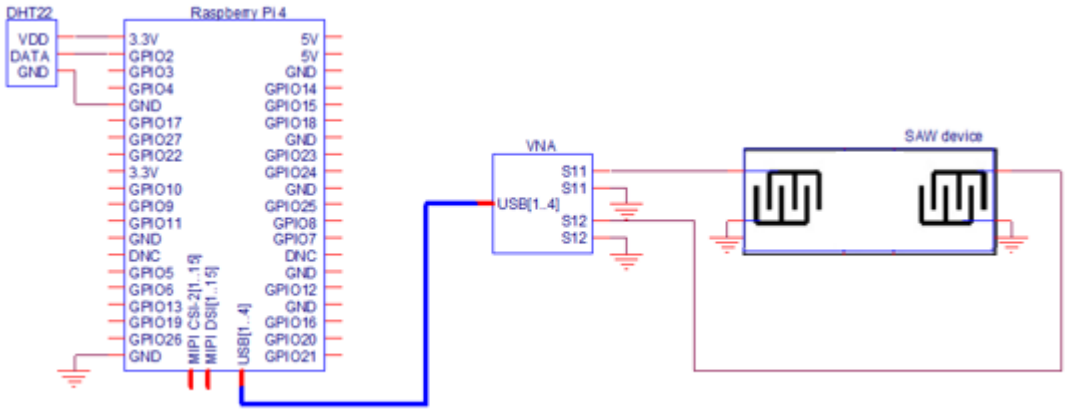

Figure 3.6 Circuit diagram of Raspberry Pi pinout and SAW control [192]

The DHT22 was kept close to the SAW device when used to assess the humidity and temperature of the air flowing over the device as shown in Figure 3.7. in this instance the shape of the humidity data is important, should the precise relative humidity be required, the sensor will need calibrating in a controlled humidity chamber.

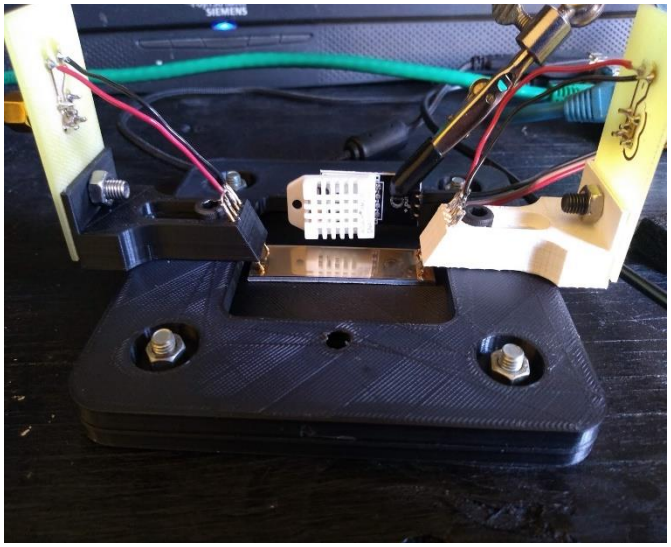

Figure 3.7 SAW device and DHT22 setup [192]

Application of breath analysis setup is shown in Chapter 6

3.2.3. Cell Stimulation

In this project, there are two methods for two types of cells investigated under the acoustic stimulation. The first type of cell is C2C12 myoblast, which was stimulated in a plate of 96 wells. The SAW stimulation was applied through the underside of the wells. The SAW device was acoustically connected with ultrasound gel as a medium. The SAW device was wired bound with silver paint connected to an SMA connector first, and then connected to a signal generator (Keysight 33220A Function / Arbitrary Waveform Generator). The signal generator was then connected to a Raspberry Pi 3 b+ and controlled from a mobile phone over the wifi.

The other cell line was the fibroblast one, which was able to be grown on a glass slide. A PDMS chamber was made using a 3d printed mould to contain the cell medium. The slide was then placed on the SAW device substrate and coupled with ultrasound gel. The SAW device had wires bound with silver paint and connected to a signal generator (Aim-TTi TGF3162 Function Generator). The signal generator was then connected to a multiplex PCB, and this was connected to the Raspberry Pi 3 b+ and controlled from a mobile phone over the wifi.

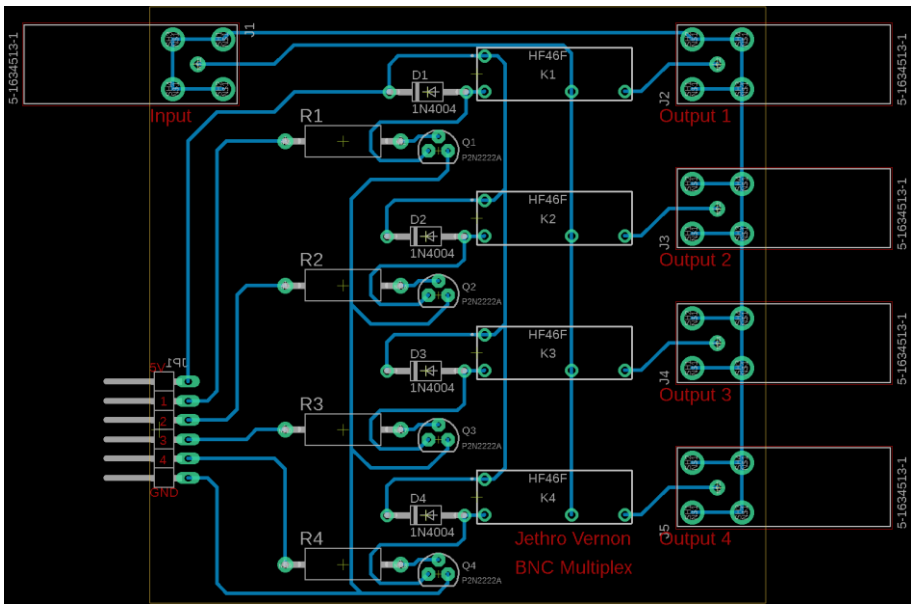

Figure 3.8 Raspberry Pi controlled BNC connection multiplex board

Application of Cell setup is explored in Chapter 7, culturing of cells is explained in 3.8

3.3. Software design and programming

The raspberry Pi uses the Raspbian operating system. This is standard and installed on an SD card inserted into the Raspberry Pi to function as the storage and boot section. Python is the preferred language and is used to integrate with equipment, run calculations and image process whilst producing a GUI that runs in parallel displaying all the information. Python is programmed in the integrated development and learning environment (IDLE) interpreter

provided with python on the Raspberry Pi. There are many python modules used to help fulfil the requirements of each project.

3.3.1. Digital Acousto fluidics

The first project involved the largest amount of equipment and sensors to be integrated and run simultaneously. The main process was the GUI, which was the setup by arranging widgets on the screen. The widgets contained the text, buttons and text fields as shown in Figure 3.9. The GUI was designed to have everything needed to control droplets and monitor them. The example shown in Figure 3.9 was designed for a single axis droplet movement.

Two separated threads were started alongside the GUI, which was designed to read the Raspberry Pi camera and the lepton thermal imaging camera. They were then displayed in separate windows, and the top left in Figure 3.9 is the visible light camera. This camera was used to track the droplet position using OpenCV and displayed in the tracking window. This window also showed the droplet when measuring fluorescence. The thermal imaging camera was displayed in a smaller window due to its low resolution and was placed at the top right in Figure 3.9. The camera was converted to greyscale where the brighter the pixel, the hotter the temperature.

The lower part of the screen was the GUI made using Kivy. Multiple sections produced the parameters used in droplet control. The first section was labelled as the device parameters. This section required the input of the measured fundamental resonant frequency of the SAW device and the minimum and maximum voltage ranges were set as the outputs from the

signal generator used whilst actuating. This also displayed a button “initialise signal generator”, which was used to connect the signal generator ready to receive further commands.

The next section was called tracking, which had a button to select the position of the droplet by clicking its location on the camera view. This displayed the distance of the droplet from the target location and also selected by clicking on the camera. This also provided the inputs for the PID controllers for both the droplet movement and heating.

The next section was droplet control which has a start button to begin a movement command. Below this in Figure 3.9 was an input field for either velocity or temperature depending on which mode was selected. This also displayed the average velocity and the current temperature of the droplet.

The next section was about using the microfluidic to dispense a droplet. The Celix microfluidic pump was connected with the set-up via USB serial and controlled using the selected API commands. The droplet size was dependent on the flow rate and flow time set. For example to create a 10 μl droplet, a flow rate could be set as 10 μl with a time of 1 second.

Next we had temperature parameters on the far right in Figure 3.9. A button was used to change between droplet movement and droplet heating modes. Below this was the temperature display when the device frequency was measured, normally at room

temperature. This allowed for the compensation to maintain the best efficiency due to the IDT heating up. The co-ordinates of the droplet and IDT locations were also set here.

Below this was the camera setting for fluorescence measurements mode. This had the exposure mode, shutter speed and camera brightness. This section also had the value required to filter out other colours so that they did not interfere with the measurement results. The upper and lower bounds of hue, saturation and values were available to be set. The camera view button was toggled between filter and non-filtered view of the main tracking window.

To the left of camera settings in Figure 3.9, all the other parameters were live graphs of various functions recorded over time. Temperatures of the droplet and IDT were displayed firstly, and the droplet was displayed in blue and the IDT in red, in degrees Celsius. Next was the peak-to-peak voltage outputs from the signal generator, then velocity of the droplet in mm/s was displayed when the target droplet was in motion. Finally the fluorescence of the droplet was recorded and displayed as shown in Figure 3.9.

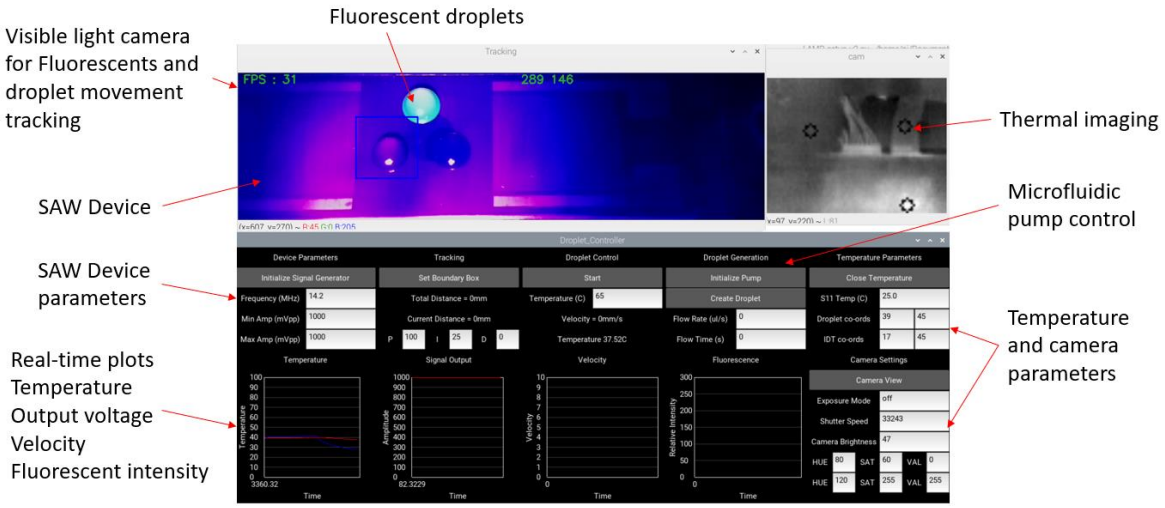

Figure 3.9 Print screen of GUI showing live graphs, videos and adjustable parameters [191]

The first function of the application was droplet movement. This was done with a feedback loop involving PID controller and object tracking. The position of the droplet was acquired using OpenCV. The OpenCV library offered eight options for object tracking algorithms. Among these options, the Kernelized Correlation Filter (KCF) [195] appears to be the best all-round tracker, offering a good compromise between accuracy and speed. This evaluated the pixel arrangement within the bounding box which was created around the droplet marked as a blue square as shown in Figure 3.9 and Figure 3.10. The KCF tracker worked firstly by the assignment of a bounding box that the user created around the object. The tracker took points from within the box and tried to calculate the motion by looking at the changes between frames. Once the new points were found, the box was recreated in the new co-ordinates. It was effectively watching the droplet moving, then predicted the new location and looked for the droplet in the direction, in which the droplet was supposed to travel. The position of the droplet was given in pixels and converted into mm using a reference on screen such as the background in Figure 3.10. Figure 3.10 shows an older version of the testbed solely focused on moving droplet in a single direction. The end position is shown as the green dot. The side view was a very early proof of concept, in order to get more accurate speed and position data, later versions include a top down view removing the parallax issue.

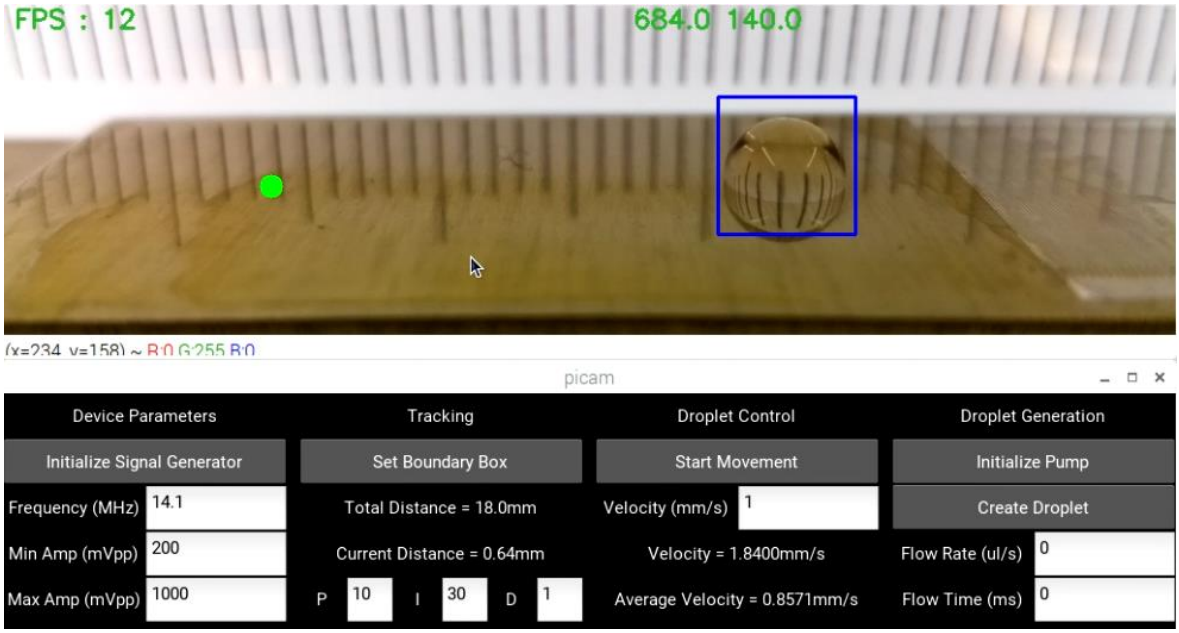

Figure 3.10 Testbed GUI side view showing droplet position and control parameters

Once the user selected the droplet position, the target destination for the droplet to move was set. The co-ordinates of the box centre were calculated and recorded. Once the droplet was moved, the co-ordinates were recorded again, and the velocity was calculated based on the time between positions and the number of pixels travelled. Using the reference scale, the velocity displayed in mm/s was converted from pixels/s and passed onto the embedded controller. A clear acetate ruler was placed on the surface and two points were select to make sure the number of pixels per millimetre was correct. The velocity for a single axis was calculated using the equation (3-1).

$$Velocity\ (mm/s) = \frac{(\frac{x_2 - x_1}{t})}{Pixels\ per\ mm} \tag{3-1}$$

where X_1 is the original position, X_2 is the new position and t is the sample time. This was then converted from Pixels to millimetres. The distance between the target position and the droplet's position can also be calculated using equation (3-2).

$$Distance\ to\ destination\ (mm) = \frac{x_2 - x_t}{Pixels\ per\ mm} \tag{3-2}$$

where X_t is the target position.

The controller changed (either increase or decrease) the power outputs of the radio-frequency signal on the forward line to maintain the target velocity and relocate droplet's new position so that the distance error was minimized. The loop process was operated in real time and was terminated when the distance errors in both X and Y directions were reaching zero, which means that the droplet has reached the target position. If the droplet was overshooting to another side, then the RF power was applied to the opposite IDTs, so that the droplet was driven back to the targeted position.

A PID controller was set to maintain a target velocity. Setting a target velocity kept the droplet from moving quicker than the frames per second of the camera, maintaining a better tracking reliability.

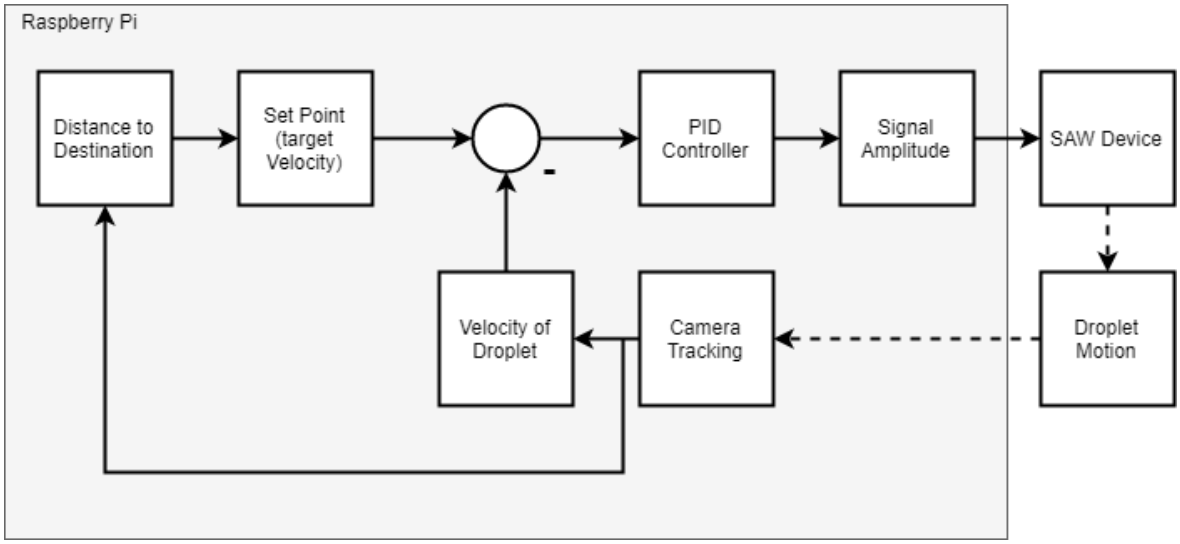

Figure 3.11 Singular direction SAW device feedback loop [191]

The PID controller was implemented using the python library “simple-pid”. To use the module, the input velocity parameter was set. The target was chosen as well as the output upper and lower limits, helping to protect the SAW device. Then the P, I and D values were set. This tuning was done manually. The gain values were chosen to reduce the time which took the droplet to build momentum and increase the accuracy of oscillation around the target velocity. Their values can be varied depending on the surface that the droplet is moving across. If the surface is very well treated with a uniform hydrophobic layer, the PID can be tuned to have a much smoother oscillation of the velocity.

In the multi-IDT touchscreen version of the platform, the additional component of exponential decay on the target velocity was added as shown in Figure 3.12. This made the droplet try and stay under the mouse position as the user dragged the cursor around. It is still allowed for velocity limits to be added to prevent too high speeds.

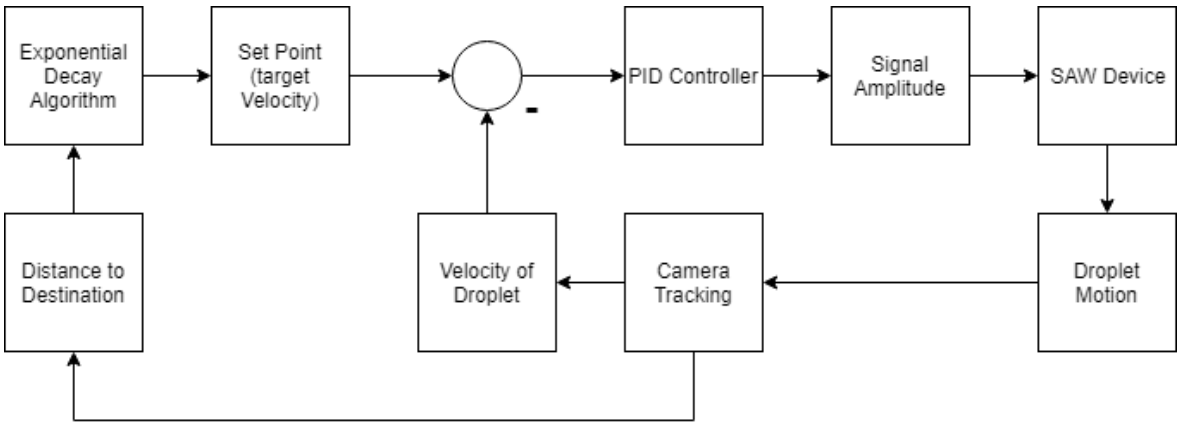

Figure 3.12 SAW feedback loop with touchscreen control

As the droplet target velocity was increased, the distance of the droplet from the user's curser/finger position on the screen was increased. This feedback loop was applied in both x and y axis simultaneously with a switch between two IDTs. Left and right IDTs controlled x-axis movement and up and down IDT controlled y-axis movement. The switching of IDT was controlled using relays switch based on the distance being positive or negative relative to the target location. As shown in Figure 3.13, a green line shows that the user is clicking to activate SAW power and direction of travel.

Figure 3.13 droplet 2 axis movement GUI

Application of Digital Acoustofluidics is explored in Chapter 4

3.3.2. In-field diagnostics

The next major component of the system after droplet movement is the diagnostics, which includes droplet heating and fluorescent measurements.

The thermal camera was used and allowed for temperature control in a similar manner to droplet movement. The thermal camera output relayed values from the droplet to another PID controller which was able to adjust the power until a target was met and maintained. A mask was created on thermal imaging camera video feed where the droplet was located, RAW number values were read from the thermal imaging camera and converted into temperature.

During the temperature cycling of the droplet, fluorescent measurements were taken from the droplet using the Raspberry Pi camera. It's important when measuring the fluorescence signals with a visible light camera to keep camera settings fixed. Exposer mode which affected white balance adjusted brightness levels automatically during droplet measurements. Shutter speed and camera brightness affected the brightness of the image. These were noted and kept content along with the fluorescent excitation source to have results comparable to each other.

Hue, saturation and value all have upper and lower bounds that can be set. These values were calibrated to the fluorescent droplet, by manually tuning the bounds. Hue was the main setting required for filtering out wavelengths that were not to be measured. Due to lab access unavailability, quinine was used as a replacement fluorescent sample instead of SYBR Green used in LAMP or PCR reactions. Quinine was readily available and biologically safe to use without needing the full DNA assay. The DNA bound dyes alongside quinine emit light in the visible light range where the conventional cameras were able to record the light [169]. Quinine's fluorescence excitation wavelength is 350 nm with an emission of 450 nm, this is within the blue and cyan range. The hue was tuned with a value range between 80 and 120,

which covered both blue and cyan. The saturation was set to a range of 60 to 255. The value was unfiltered with 0 to 255 set as the bounds.

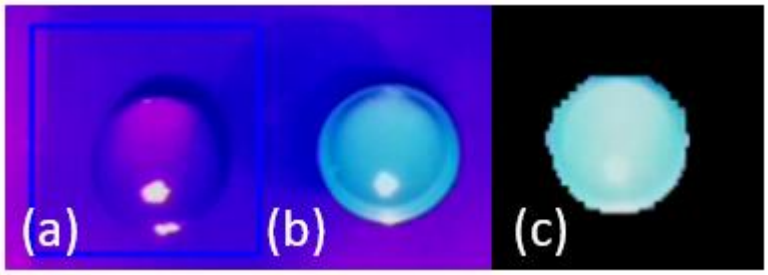

Figure 3.14 droplets under fluorescent light (a) DI water droplet (b) quinine solution fluorescing (c) fluorescing droplet with digital filter [191]

Application of Digital Acoustofluidics is explored in Chapter 5

3.3.3. Breath analysis and Apnoea detection

A user interface was also created for the breath analysis. This program was mainly focused on recorded frequency from the vector network analyser and the DHT22 combining both humidity and temperature sensors.

The PyVISA module was used to connect to the network analyser via the ethernet port, using a TCP protocol. The network analyser was the host acting as the router assigning an IP address to the Raspberry Pi. Queries were sent to the network analyser such as a request for the frequency spectrum data displayed on the screen. The network analyser then responded with the trace data for both dB and frequency. These were split and stored in arrays which were sent to the live plot on the GUI (as shown in Figure 3.15 in the bottom right plot) and used in finding and following the lowest value which was the resonant frequency. The resolution was set through the GUI labelled “number of samples”. The higher the value the longer it took for a full frequency sweep. For example, 801 data points took approximately 1 seconds to complete the spectrum shown on screen. The parameters for the network

analyser were set with start and end frequencies. This also included a button to apply changes and toggle between s11 and s21, when was the S21 mode. The highest value was recorded as the current frequency of the device. Options to save the spectrum and the frequency shift over time were also available on the bottom right of the GUI alongside the option to reset and clear all graphs.

The minimum value was recorded and displayed in a separate plot on the bottom right of the Raspberry Pi display. The Adafruit_DHT library was used to read the values from the DHT22. These values were recorded in arrays and displayed in the top left and right plots for temperature and humidity as a function of time.

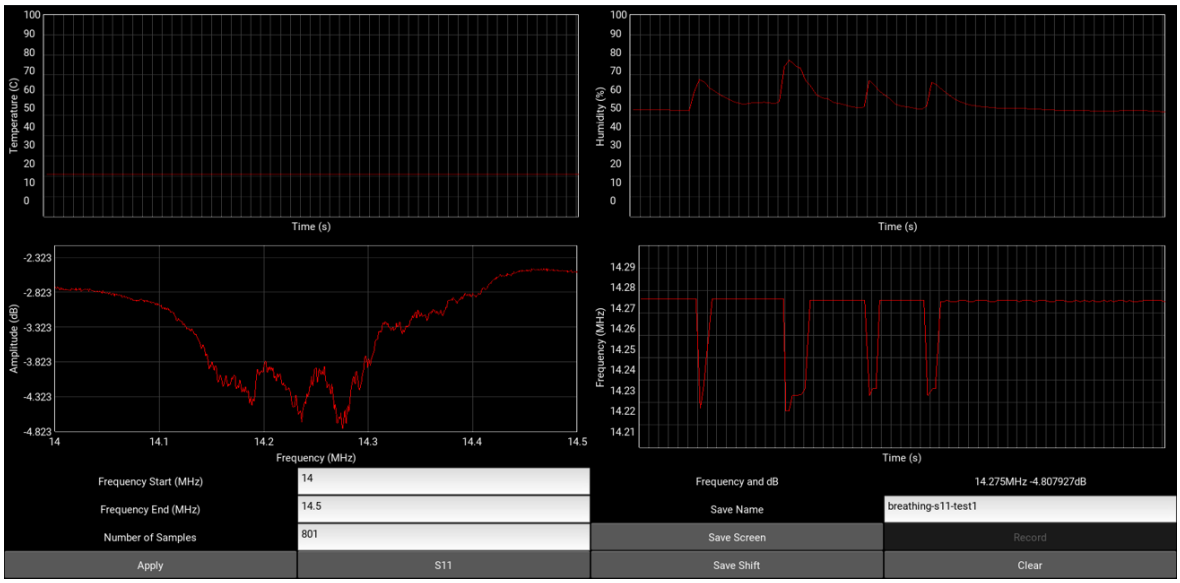

Figure 3.15 Print Screen of GUI showing frequency spectrum, temperature, humidity and frequency shift

Application of breath analysis setup is shown in Chapter 6

3.3.4. Cell Stimulation

Stimulation of both types of cells used GUIs to support automation of SAW actuation due to require multiple times over 2 days. Figure 3.16 shows both of the user interface versions. Both cell lines required very similar treatment, and the same method of stimulation was

applied. This program was designed to control signal generators and SAW multiplex boards for autonomous switching between SAW devices for stimulating cell samples. The signal generator was connected using the modules of PySerial and PyVISA. This enabled them to be switched on and off as the schedule requests. As shown in Figure 3.16 (a) and Figure 3.16 (d), the frequency of the devices being used was set as well as the amplitude. The numbers of cycles and pulses were applied to the cells. The pulses on and off durations were set in minutes and seconds. As shown in Figure 3.16 (c), the user had the choice to select the exact date (day, month and year) and time (hours and minutes) of the SAWs to actively stimulate the cells. These screens were sent to the user's phones which enabled the remote activation and information on the progress displayed in the information tab, as shown in Figure 3.16 (b).

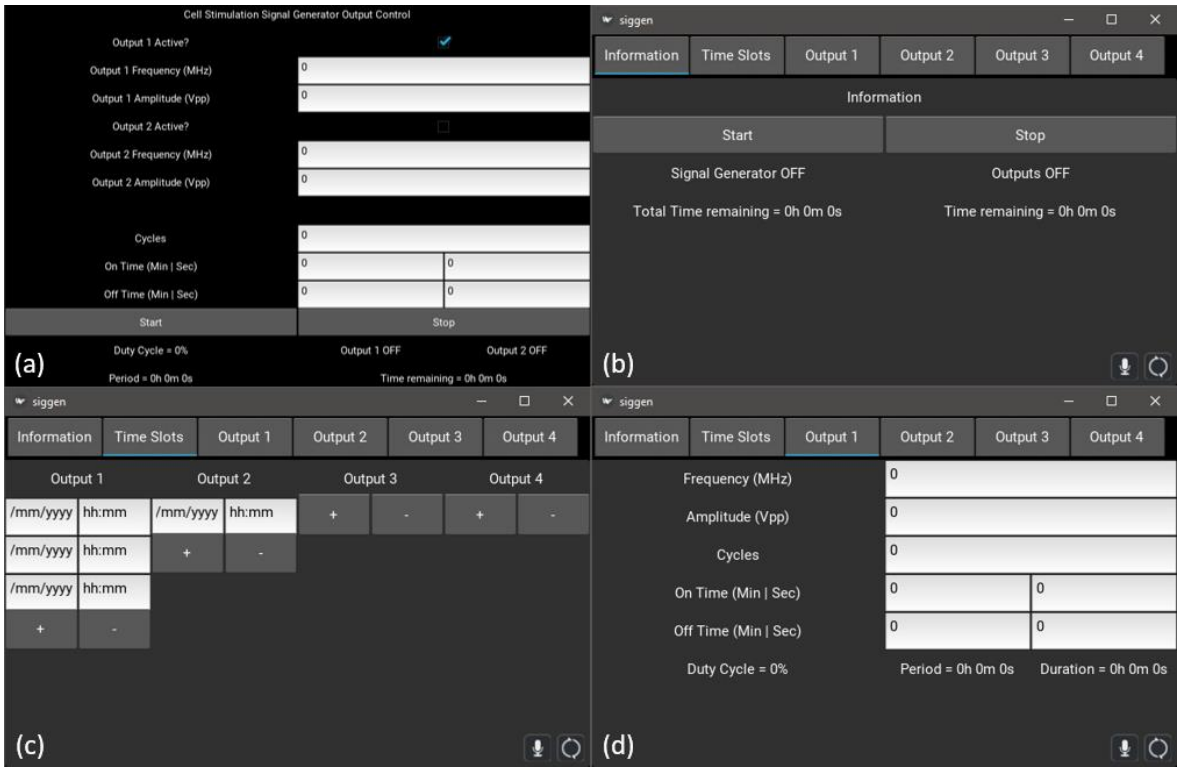

Figure 3.16 SAW cell stimulation GUI (a) older version used for myoblasts (b) information screen showing signal generator and time information (c) the ability to add time slots for up to four individual cell stimulations (d) parameters for each Saw device and stimulation settings

Application of Cell setup is explored in Chapter 7, culturing of cells is explained in 3.8

3.4. SAW acoustofluidics

For the majority of experiments, the chosen liquid was the DI water, which has a viscosity and density of 1.0016 mPa.s and 995.0 kg/m^3 respectively. We also tested 17.388 (wt%) aqueous glycerol solution to investigate the effect of higher viscosity for Newtonian fluids. The kinematic viscosity and density of this solution was 1.5631 mPa.s and 1039.8 kg/m^3, respectively.

To simulate the non-Newtonian behaviour of liquids such as blood, droplets of Xanthan solution (molecular weight, Mw ~ 10^6 g.mol^{-1}, Sigma Aldrich) [196] with concentration of 800 (ppm w/w) and density 995.4 kg/m^3 were used in the experiments. The power law ($\mu = 0.076\dot{\gamma}^{0.51}$, where $\dot{\gamma}$ is the shear rate in the flow) was used to calculate the viscosity of the solution. The volume of liquids was manually dispensed using pipets ranged from 1 µl to 20 µl. Commonly 5 µl and 10 µl volumes were applied.

When the SAW devices were used to actuate droplets (Figure 3.17), the substrate needed to be hydrophobic. CYTOP® (L-809A from AGC Chemicals) a biocompatible fluoropolymer coating was used to treat the device. CYTOP was dissolved in exclusive fluorine-based solvents, and it was used as a thin film coating with a thickness less than 1 µm. The solution was applied onto the area where liquid actuation was generated. This was either applied manually via a pipette or if available, using dip-coating. Dip-coating created a thicker and more uniform layer of CYTOP. Once applied, the CYTOP was then heated to 180 ^{o}C for 10 minutes. The hydrophobic level was manually inspected by examining the droplet contact angle to the substrate.

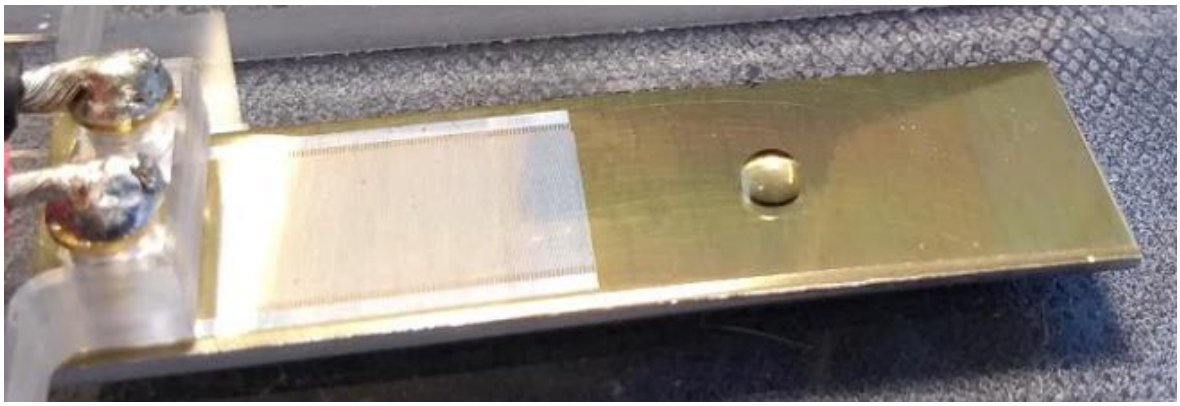

Figure 3.17 Thick plate aluminium SAW device with droplet on hydrophobic surface

3.5. Temperature sensing and SAW heating

The small FLIR lepton module was used for temperature sensing, and it was required calibration. These values were calibrated using another higher quality thermal imaging camera, pointed at the droplet and controlled the temperatures. The position of thermal imaging cameras was to be carefully selected. The surface of the SAW device was reflective and false temperature reading was often acquired from heat sources showing through the reflection. If the camera was perpendicular to the substrate, the reflection of the thermal imaging camera was seen interfering with temperature values.

When the droplet was heated up, it moved to the area that was less hydrophobic area. Methods were needed to prevent the droplet from moving as easily during the application of SAW power. Some experiments were performed with a PDMS or silicone rubber chamber to prevent movement. For droplet heating for long durations the droplet would be evaporated. To prevent this, a mineral oil coating could be placed over the droplet [197]. A

small number of tests were performed with a chamber with a germanium lens (mirror like disk) to prevent the reflection effect.

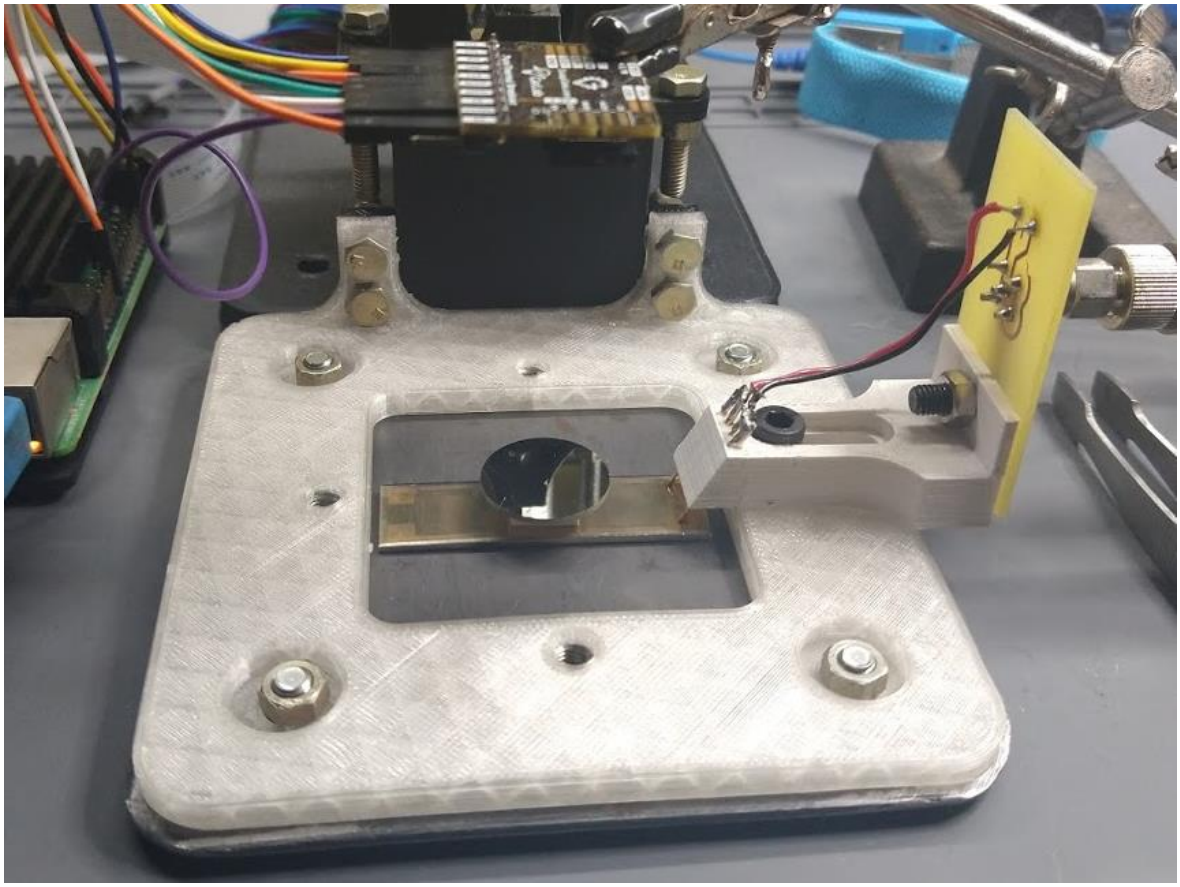

Figure 3.18 Image of SAW device in 3d printed holder with chamber and germanium wafer on top

3.7. Breathe analysis procedures

When performing the breath tests, the SAW device was placed close to the nose and the user would exhale onto the device. The device's distance from the nose was adjusted until the frequency shift was visible but not saturated during normal breathing. The DHT22 sensor was placed as close as possible when assessing humidity changes over the device.

3.8. Culturing of myoblast and fibroblast cells

For both types of cells, they had the same cell culture procedures, but with different proliferation durations. The procedure steps are explained below.

The testing area on the device was kept as clean as possible to prevent contamination. When working with the cells, all processes were handled in an extractor hood. Before using, the area was sterilised with UV lamp for 30 minutes, and anything passing into the extractor hood was disinfected with an ethanol/water mix 70/30 %. Anything non-metal to be disposed of was wiped down with Virkon.

3.8.1. Defrosting Cells

Cells were firstly taken from storage and defrosted. Cells recently defrosted can take double the time to grow initially for the first passage [198]. The cells were kept at -150 ºC and moved to -80 ºC whilst the other items were prepared. Fetal Bovine Serum (FBS) a growth supplement and Penicillin streptomycin (P/S), antibiotics for the cells were defrosted from -20 ºC. All the items should not be defrosted too quickly or not to be shaken excessively otherwise proteins became denatured. The FBS and P/S were held in water at approximately 37 ºC to avoid denaturing whilst defrosting. Once defrosted they were placed in an ice box alongside the growth medium DMEM. Finally the cells were defrosted.

3.8.2. Cell Passaging and Culturing

Firstly the DMEM was placed in the fume hood. Then 50 ml of FBS and 5 ml of P/S were added into the medium. Next 15 ml of the mixture was extracted using a pipette and placed

in a plastic container. Following this, a smaller pipette with a small tip was used to extract the cells and added them to the mixture. The mixture of DMEM, FBS and P/S was then labelled with the chemicals and the date when it was prepared. The container with the cells in medium was labelled inside the fume hood with the cell line, date and passage number. The lid to the container was secured and then released by half a turn to allow the CO_2 mix in the incubator to penetrate the container. After finishing this stage of the work, the workbench of the fume hood was then cleaned with the 70 % ethanol mix.

3.8.3. Subculturing Cells

Firstly the medium was removed from the container with a long pipette using the pipette gun. The medium was disposed of in a beaker containing Virkon. The cells that were attached to the container were then washed with Phosphate buffer saline pH.7 (PBS), which removed any medium remaining among the cells. The PBS was then removed with a pipette and disposed of in the Virkon beaker. Next 6 ml of Trypsin was used to release the cells adhering to the plastic container. The container was closed fully and placed in the incubator for 6 minutes as the enzyme worked best at 37 ºC. After this, the walls of the plastic flask were gently tapped to further detach the cells. The next step was to neutralise the mix of Trypsin and Cells using 6 ml of neutralising mixture of FBS, P/S and DMEM. If splitting the same passage number and the same pipette were used. The neutralised mixture in the bottle was washed out by putting pipette near the bottleneck and putting liquid inside where the cells were at around a 45 ° angle and the liquid was moved back and forth in the pipette 10 times. The cells were then placed in a clean vial. They were separated from the neutralised medium by placing them in centrifuge and making sure that the centrifuge was balanced before activating with the following settings: 1200 rpm for 5 minutes at 4°C. It was important not to shake the cells to remix them at this point. The following step was to remove

the supernatant from the vial without sucking up the cells resting at the bottom. If they accidently made it into the pipette, before transferring to the waste container, they had to be put back in the vial and centrifuged again. Next, 15 ml of the complete growth medium was added into each flask for passage 2 (P2) and 4 ml into cell vial. The cells were mixed into the fresh medium by gently pipetting. Finally 2 ml of the cell and medium mixture were then transferred into each P2 flask by pipette. The cells were then placed in the incubator and cultured at 37 ºC.

3.8.4. Freezing Cells

Firstly the medium with the pipette was removed and disposed of into a beaker containing Virkon. The attached cells were washed with 10 mL PBS. They were then rinsed by having the PBS move back and forth for the cell cultures. After this the PBS was removed with the pipette and disposed of into Virkon. Then 6 ml of Trypsin was added to the cells. The mixture was closed and placed in the incubator for 6 mins at 37 °C. The cells were further detached by gently tapping the flask walls. 6 ml of the neutralising mix was placed in the trypsin and cells. The cells were washed out by pipetting and the cells were placed in a clean vial. They were placed in the centrifuge to separate the cells at 1200 rpm for 5 minutes at 4 °C. The supernatant was removed from the vial and disposed of in Virkon. The cells were then resuspended in 1 ml of cryomedium and evenly distributed by pipetting the cells up and down. Finally the cells were placed in cryovial and labelled with cells and date, then stored at -80 °C.

3.8.5. Cell SAW stimulation setup

During the cell stimulation tests, the c2c12 cells were grown in a 96 well plate. Below the plate a thin foil SAW device was attached using ultrasound gel as a medium for the acoustic wave to propagate, as shown in Figure 3.19.

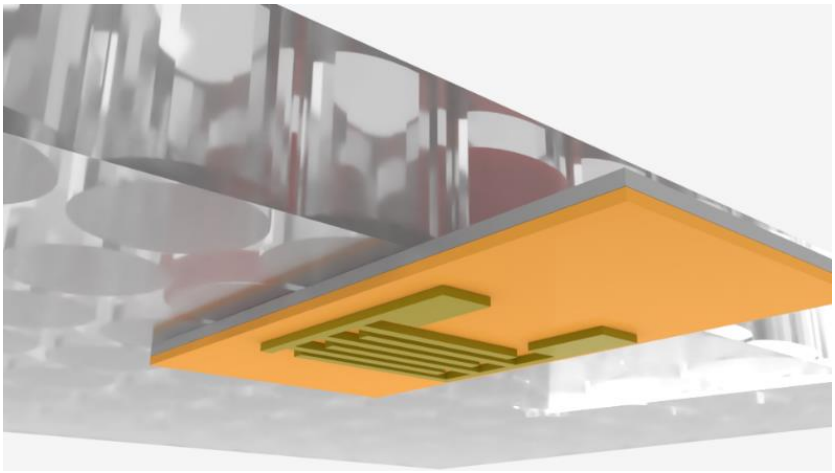

Figure 3.19 a SAW device placed under the 96 well plate

The cells were placed in an arrangement as shown in Figure 3.20. Three samples and a set of control wells were unstimulated by SAW. Each sample had 5 wells. The central well was situated directly above the IDT with one in front and one behind.

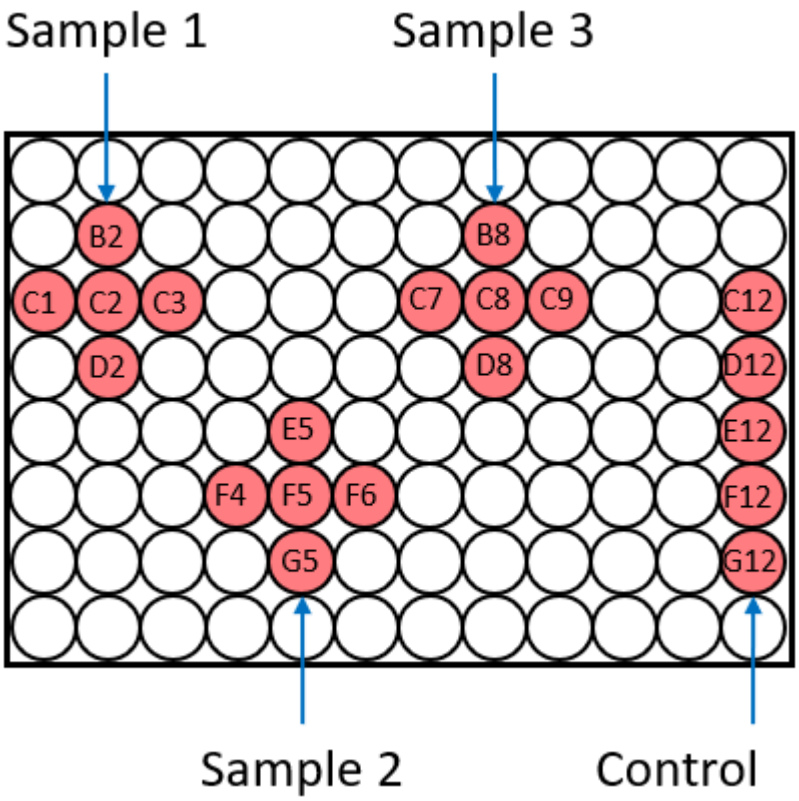

Figure 3.20 The cell arrangement in the 96 well plate

For the fibroblasts they were grown on a glass slide in a PDMS chamber as shown in Figure 3.21. The slide was connected to the substrate with ultrasound gel in front of the IDT.

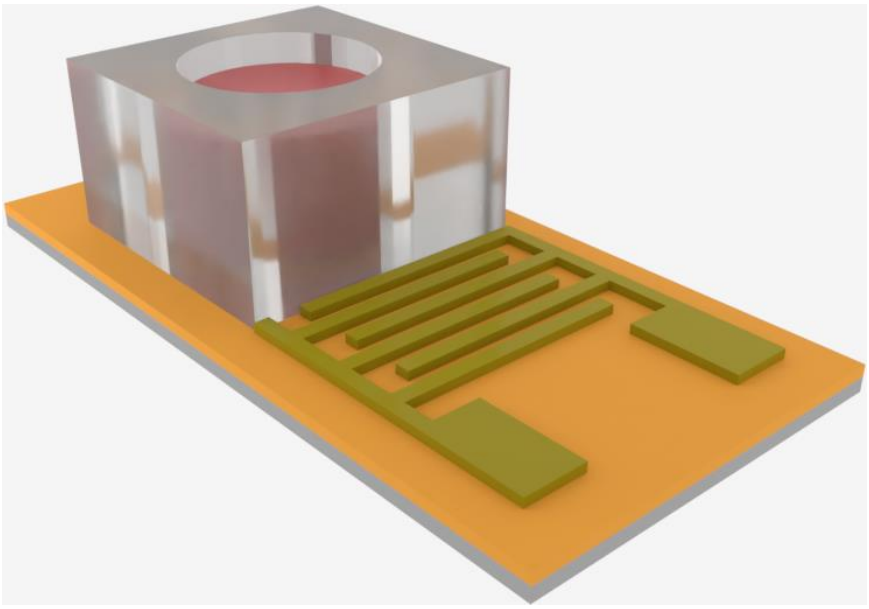

Figure 3.21 SAW and fibroblasts in PDMS chamber

Application of Cell setup is explored in Chapter 7

Chapter 4. Digital acoustofluidics with open source electronics

4.1. Introduction

Open-source platforms have made electronics more accessible. Platforms such as Arduino have reduced electronic processing for sensors and actuators. Raspberry Pi goes one step further, providing a computer-alike operating system and a customised ecosystem of plug and play hardware. In this PhD project, we demonstrated the suitability of combining SAW with Raspberry Pi embedded electronics to interface and control acoustic waves.

In this chapter, we investigate Raspberry pi SAW platform's ability to manipulate liquid samples. We demonstrated the remote-control functions of generation, pumping, moving, and mixing of single and multiple droplets. These liquid samples could be biomedical or hazardous and are often required automated manipulation to minimize human contact, contamination and errors. We tested the performance of the setup transporting droplets across surfaces, or on incline-angled surface, with various volumes and liquid types.

A description of the platform is in Chapter 3

4.2. Droplet transportation

Typically, fluidic handling technologies lack re-writability and re-programmability. Recently a contactless droplet transport mechanism and processing technique called digital acoustofluidic has been developed. It can execute reactions on overlapping, non-contaminated, fluidic paths and can also be scaled to perform massive interaction matrices within a single device. Droplet movement is crucial in digital acoustofluidics. Here we demonstrated accurate transport control using Raspberry Pi as the embedded processor.

4.2.1. Velocity and power

Figure 4.1 shows an example of controlled DI water droplet movement. Each droplet was propelled across a SAW substrate with the surface treated into hydrophobic. In these experiments, each droplet travelled 20 mm across the SAW device in a single direction. The power sent to the SAW device determined the acceleration and velocity of the droplets and was controlled by adjusting the voltage output of the signal generator. This voltage was controlled with a PID controller to maintain a speed of 1 mm/s, which was chosen due to the limited frame rate of the camera tracking the droplet. Running image tracking algorithms often caused large fluctuations in the frame rate due to the limited performance of the Raspberry pi in conjunction with python, an interpreted language. At higher velocities the tracking had a higher chance of losing the droplet position or the droplet was traveling faster than the framerate, thus resulting in the droplet appearing to skip frames and jumping across the screen and overshooting the destination.

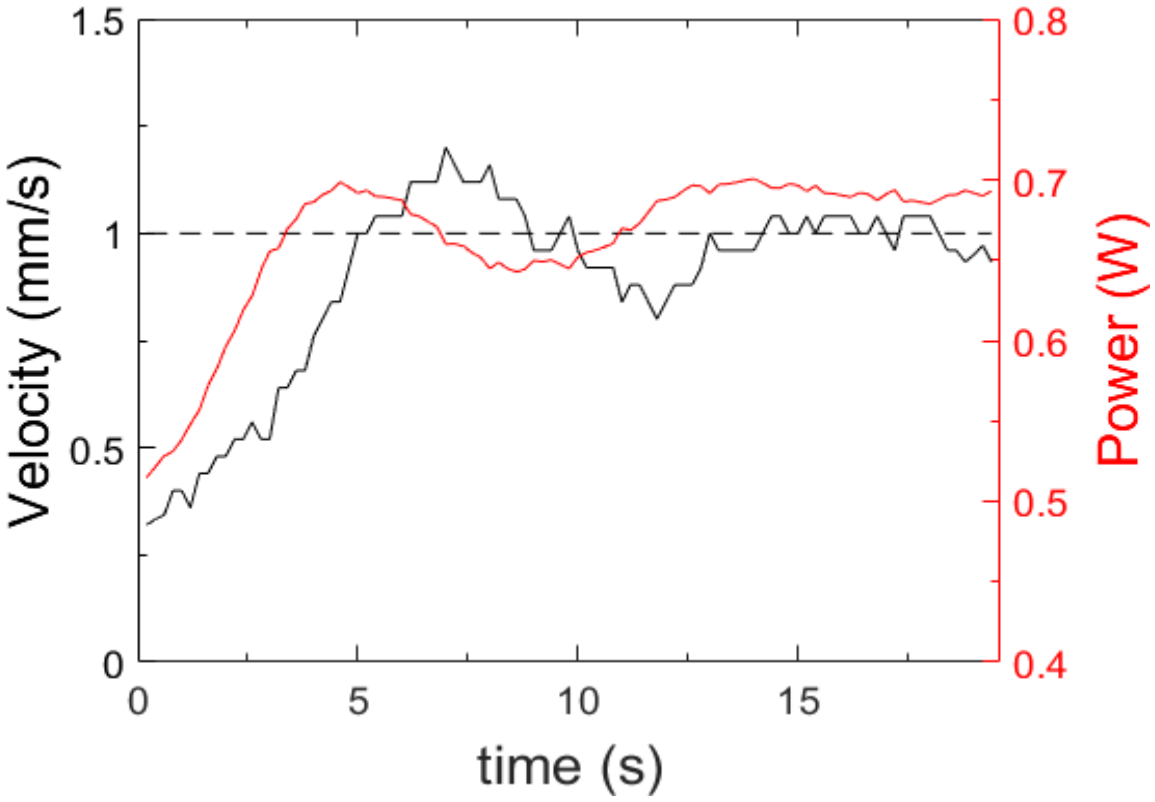

Figure 4.1 Typical examples of PID controlled movement [191]

For the droplet to gain momentum, the power would need to be rise higher to accelerate the droplet to the target velocity. The droplet then exceeded the target and the power was dropped, and this oscillation was continued but reduced overtime as the droplet began to settle at the target speed. In Figure 4.1, a 10 µl droplet movement is shown. This was the most common size used throughout tests. In this example the droplet was required between 0.6 and 0.7 W to maintain velocity. The droplet took 5 seconds to get up to speed and a further 20 seconds to stabilise. There was an initial overshoot of 0.2 mm/s after which the droplet oscillated around the target velocity with a speed of 0.2 mm/s. The droplet usually stopped within 0.5 mm of the destination.

Larger droplets took more time to reach the destination, mainly due to the initial power built up to start the movement of droplets. Adjustments in the minimum and maximum power as well as further tuning of the P, I and D values would reduce the deviation.

4.2.2. Increasing inclination angle of substrate

During on-field operations, for instance point of care testing, there might not be a flat surface to accommodate the setup. Thus, it is important to test the platform under the inclined angle operation along a slope. Figure 4.2 shows the transportation of a 2 µl droplet with increasing substrate tilting angles from 15º to 90º. As expected, the power required for droplet movement was increased with the increasing angle. However, after 60º the power increased rapidly, because of the significantly increased gravity component. This reveals that the SAW platform is capable of operating in situations that prevent the substrate from being level and create flexibility on design in applications requiring sample transportation.

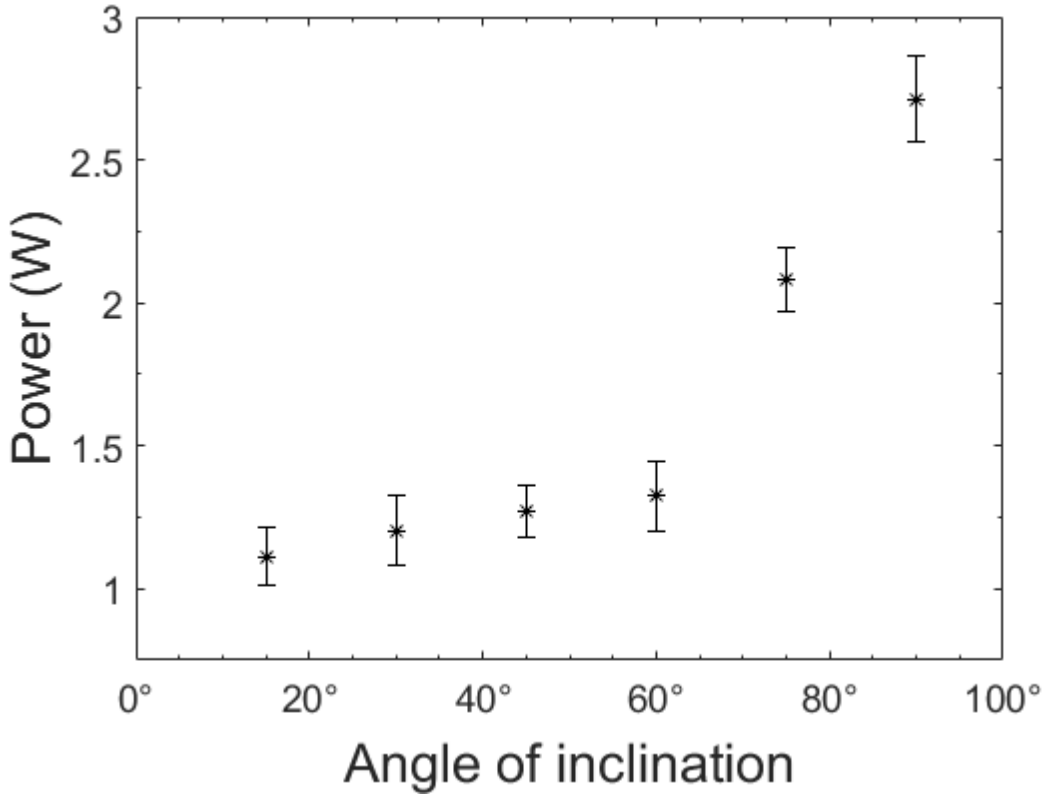

Figure 4.2 Power required to transport droplets across inclined surfaces [191]

4.2.3. The effect of droplet volume

Molecular diagnostics require a microfluidic protocol consisting in administering different volumes of fluid [199]. Typically washing buffers are much larger in volume than the sample, hence it is important to study the setup's performance under the influence of increased volume. Figure 4.3 shows the relationship between the average power to keep a droplet moving and the volume of a droplet. The average power was calculated from when the droplet started moving until it arrived at the end position. The set distance was 18 mm and the target velocity was 1 mm/s. As can be seen from this graph, when the volume of droplet was increased, the average power to keep the droplet moving was increased accordingly.

It is likely that droplets that need to be manipulated will not always be the same volume. Figure 4.3 represents the results showing the ability of the SAW device to not only move a fixed size, but also track the position of droplets as small as 1 µl. This is useful in reducing the quantity of samples and reagents needed in chemical and biological reactions. With the addition of the high quality raspberry pi camera and ability to mount a wide range of lenses including microscope objective lenses, it could be possible to work with nanofluidics, manipulating much smaller samples sizes.

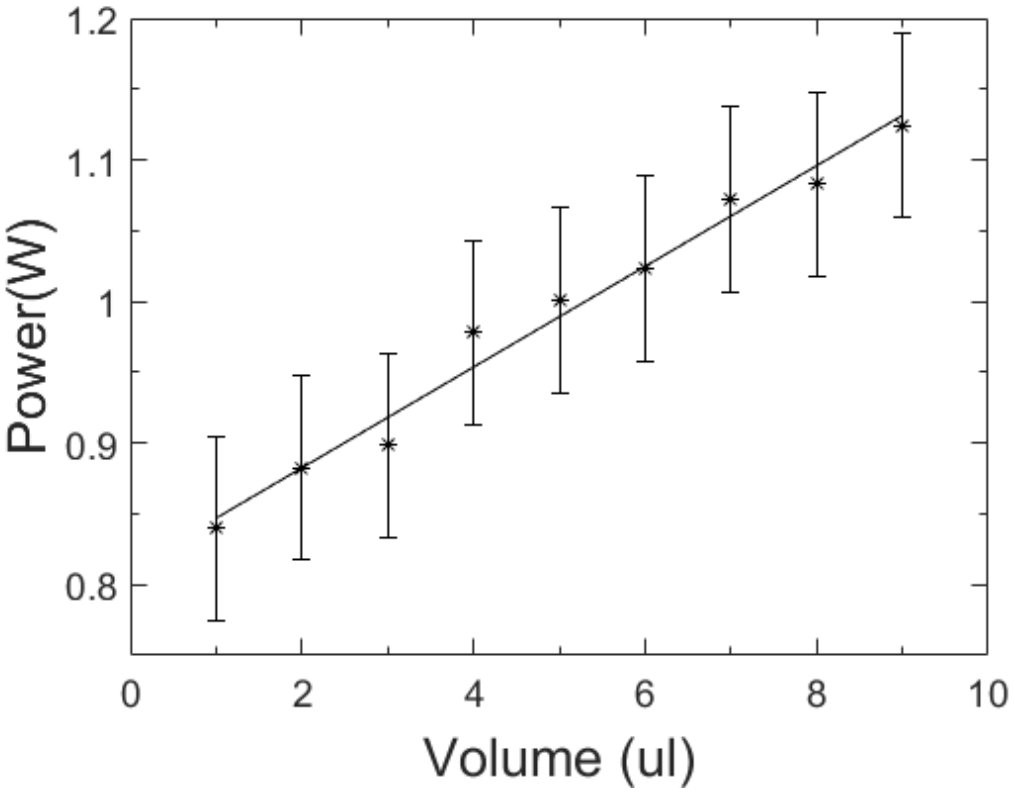

Figure 4.3 droplet transportation and droplet volume

4.2.4. Transporting different liquid types

Molecular diagnostics require the microfluidic handling of several fluids. Thus, we have further investigated the ability to control different liquids. The average powers required for different water droplets to be transported at different velocities have been realised. The results are shown in Figure 4.4. Water droplets have been used as a starting point. Once the functionality has been proved, diluted glycerin which is 1 part glycerin and 6 parts water, was used because of its higher viscosity. This can be clearly identified from the power readings as the higher viscous liquid samples at all volumes required more power to move along the surface as shown in Figure 4.4. A Xanthan-water solution [196] was also used. A mixed solution of 800 ppm was chosen as it is the closest to the properties of blood. Microfluidics is an attractive approach for blood plasma separation and preparation for medical diagnostics [200]. Xanthan is a non-Newtonian fluid, thus the longer the liquid is stressed, the less viscous it becomes. The Xanthan required similar power to water at lower volumes, and with the increase of power, it became close to that of the higher viscosity liquid as shown in Figure 4.4.

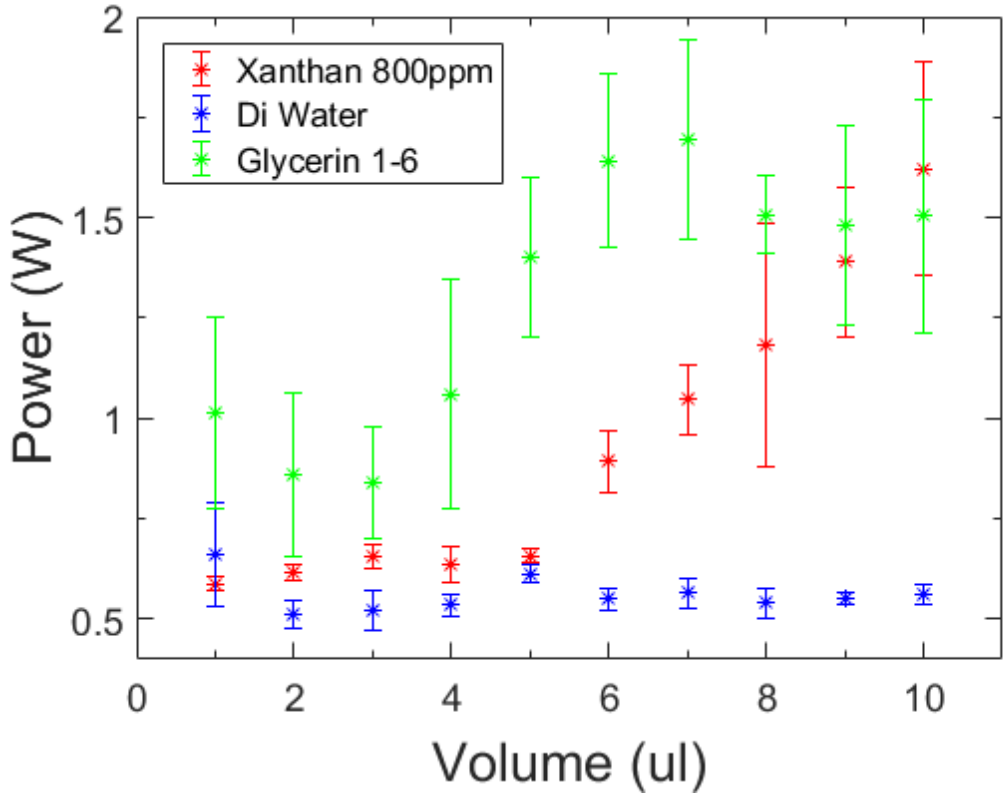

Figure 4.4 Average power requires for different liquids to be transported at a fixed velocity [191]

A large factor that was difficult to control was the hydrophobic treatment of the surface. Due to working from home during lockdowns with restricted lab access, the proper procedure of application was not followed. CYTOP® was applied and the heat treatment was done for quite a long time. The CYTOP surface quality degraded very quickly when under use, so it needs to repeat the dip or spin coating process. As the surface became degraded, the droplets required more power to gain the same momentum when compared to a freshly treated coating. This also created uneven or non-uniform surfaces where the droplet appeared to get stuck until an increase in power was applied to overcome this.

4.3. Sample mixing

We demonstrated remote controlled mixing functions that can be used for biological samples and reagents. One of the examples for droplet mixing is shown in Figure 4.5. One droplet was DI water and transported to mix with another one containing red polystyrene particles. To mix the polystyrene into the DI water thoroughly, the distribution of the particles in the droplet was monitored using the digital camera. The duration of the mixing was set arbitrarily to the point where the microparticles appeared evenly distributed in the droplet. This mixing protocol can be adjusted and optimised based on the applications or liquids used. During the remote controlled mixing process, the droplet of DI water was chosen as the tracking boundary and the droplet with red polystyrene as the destination. The DI water was pumped to the droplet with red polystyrene particles. These two droplets were merged into one larger droplet and then mixed. For this mixing example, one IDT was used. In this demonstration, the acoustic waves propagated from the right side of the screen. The DI water was in path of the wave absorbing the majority of the energy. Over a certain power threshold, the energy in the droplet becomes greater than the friction allowing it to move towards the other droplet. The droplet with the polystyrene beads had been moved slightly due to a small amount of SAW energy that had passed the DI water to this droplet.

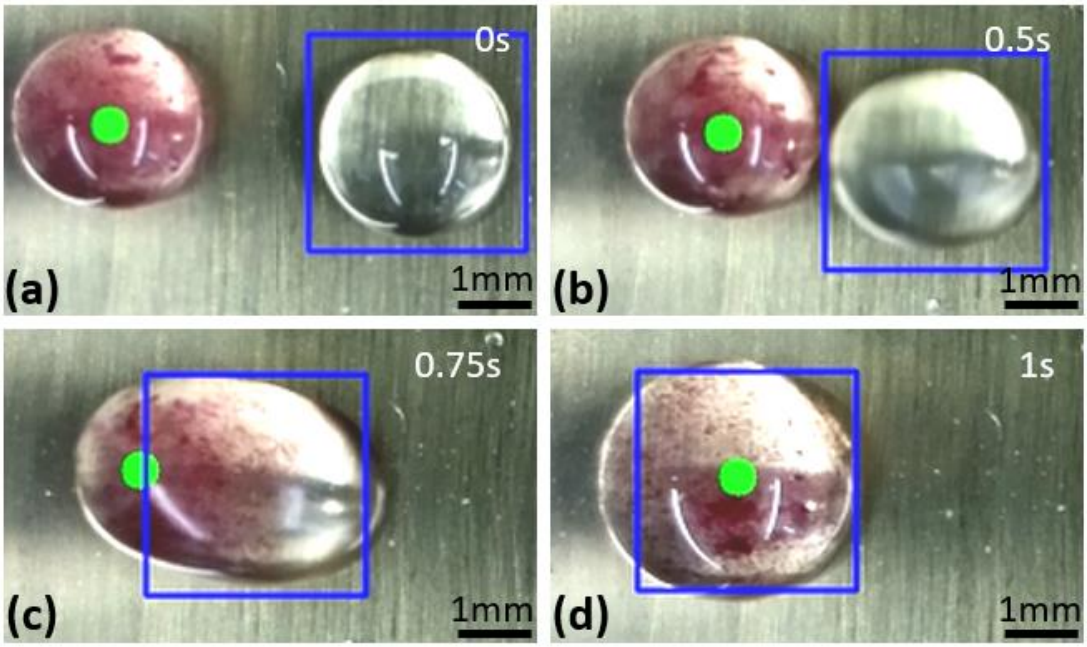

Figure 4.5 Droplet mixing of microparticles (a) no movement (b) 0.5 seconds into movement (c) droplet merging (d) droplet mixing [191]

4.4. Control on XY plane

Figure 4.6 represents an example of droplet movement in both X and Y directions over 5 seconds. Separate signal sources and PID controllers were used with multiple IDTs allowing the droplet to be propelled diagonally. This process used the touchscreen function. When the user clicked (or placed a finger on the screen), a trajectory green line appeared between the droplet and the curser location, and the droplet was transported along in this direction. Along both the X and Y directions, SAW devices would behave in the same way as represented in Figure 4.1.

Whilst movement in multiple axis was demonstrated, however, it remained a challenge for the smooth movement of droplets. This was believed to be largely dependent on the 4 IDTs on the device, as each of them had their own tolerances due to the fabrication processes.

Because of this tolerance, the frequency of each device was varied slightly as well as the sharpness of the peak which could affect the efficiency of the SAW device. This meant that applying the same power to two IDTs the output mechanical waves could have two different magnitudes. With this setup, two PID controllers were used for *x* and *y* axis running in parallel. In the future we will use the embedded electronics to implement individual PID controllers for each IDT. This would allow for droplet motion to appear the same, whilst the power applied to the SAW could vary significantly depending on the SAW device.

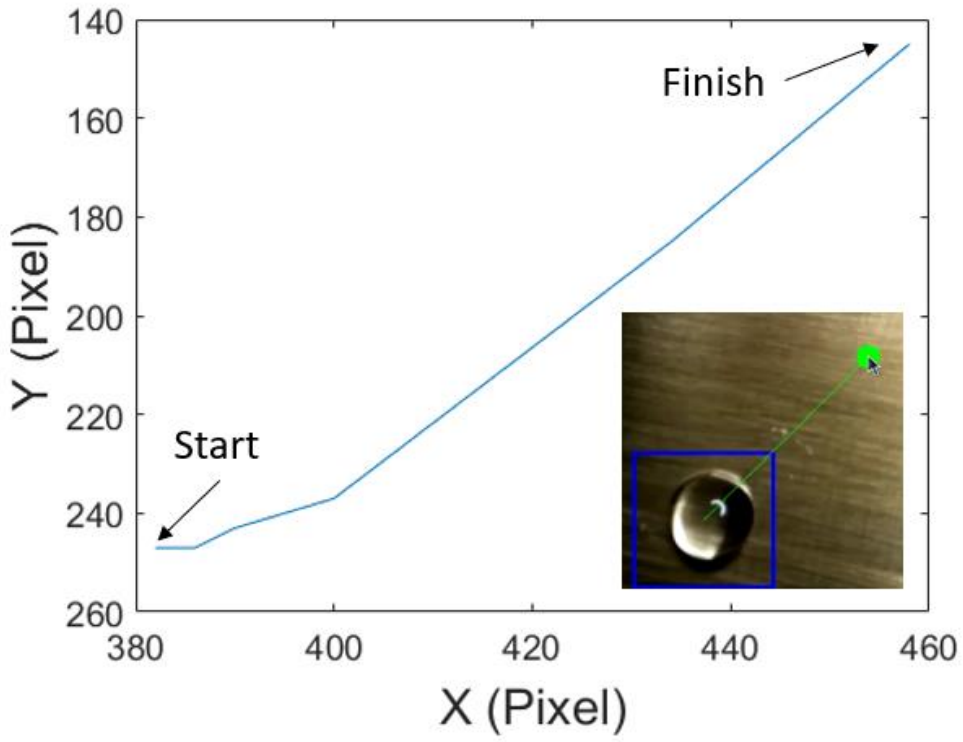

Figure 4.6 Droplet movement using multiple IDTs [191]

4.5. Acoustic heating

Figure 4.7 shows an example relationship between the changes of applied power and the temperature of the droplet during its transportation. As can be seen from the figure, the

droplet's temperature was increased during the entire movement as long as the power was applied. However, as the applied power was decreased slightly, the increase in the rate of temperature of the droplet became smaller. This is because as the velocity of the droplet reached the targeted value, the power was reduced in an attempt to maintain that speed. The droplet temperature was found to increase by 3 degrees during the movement, starting at room temperature. This shows that under normal operation the droplet temperature is not a large concern, however if higher power is required to move the droplet more heat with by generated potential causing the droplet to evaporate quicker.

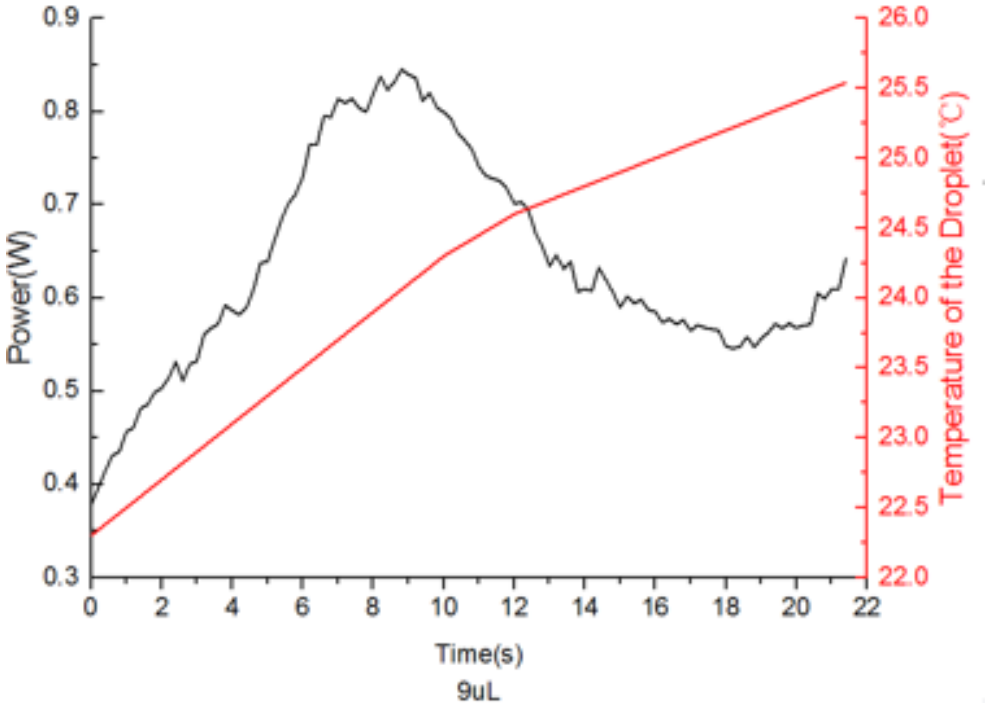

Figure 4.7 The relationship between applied power and the measured temperature change during the droplet transport

4.7. Summary

In this chapter, we have presented a SAW Raspberry Pi platform, showing ability to perform a number of acoustofluidic functions. We have demonstrated that we can successfully move droplets across a substrate to a target position using PID controller and camera tracking in a feedback loop. These droplets can be varied in size, varied in liquid properties and even successfully moved on inclined, deformed, or sloped substrate. The results showed that even without optimal PID tuning, the droplet was able to be transported across the surface without significant changes in velocity in the event of a non-uniformly treated surface. The setup was also capable of moving different liquids together and then mixing them using the vortices generated in the liquid, which could be used for mixing or reaction of biological samples and reagents. Using SAW devices with four inward facing IDTs we have also shown that the platform moved a droplet on an XY plane by the implementation of multiple PID controllers running in parallel on separate axis. This automated droplet manipulation could be used for biomedical or hazardous samples reducing human contact preventing contamination. It could be effective in small scale rapid mixing in biochemical analysis and drug mixing [77]. The next stage to improve the control of droplets would be a higher position sampling rate, this would require the control running in C instead of python increasing the frame rate of the camera. This would enable fast and more intricate manoeuvres with droplets. Another major development would be introducing more IDTs. With a greater number this would also add control of multiple droplets simultaneously, opening up the possible of multiplexing biological assays.

Chapter 5. In-Field medical diagnostics with open-source opto-acoustofluidics

5.1. Introduction

This chapter demonstrates SAW heating and optical detection with open-source electronics for PCR and LAMP applications. SAW devices are increasingly applied in life sciences, biology, and point-of-care applications due to their combined acoustofluidic sensing and actuating properties. As discussed in Literature Chapter 2, in recent years although there have been significant advances in acoustic devices, the technology still requires benchtop lab equipment and experienced operators to utilise these SAW devices because of a lack of hardware integration and autonomous control to facilitate a high performance and low-cost system. In this work, we presented a versatile and digitally controlled acoustofluidic platform by demonstrating heating functions using a closed-loop feedback control with image recognition as a detection method. Moreover, we integrated optical detection by demonstrating in situ fluorescence sensing capabilities with a standard camera and digital filters, bypassing the need for expensive and complex optical setups [191]. Quinine was used to demonstrate the DNA amplification in the testing of this system. For this we use a sessile droplet of DI water for the demonstration. These droplets were dispensed onto the surface where their locations were found, and then the target temperatures and control parameters were set. The optical camera was set to capture the area of the substrate just beyond the IDT where the droplet samples were positioned.

A description of the platform is in Chapter 3

5.2. SAW heating

Figure 5.1 shows the differences in recorded temperatures between the IDT surface and the droplet in front. The peak-to-peak voltage in the *x* axis refers to the input at the amplifier, showing that the SAW energy has been transferred into the droplet. Increasing the voltage resulted in an increase in power applied to the SAW device. When a droplet is excited by an acoustic wave, which may be for mixing or transportation, heat is produced in the substrate due to the mechanical movement of the waves. We can utilise this to transfer heat into a liquid on the surface to aid and control biological reactions in small samples. These values were recorded until the temperature began to reach a plateau for each voltage value. This showed that we can adjust the voltage and control the temperature of the droplet situated on the SAW device.

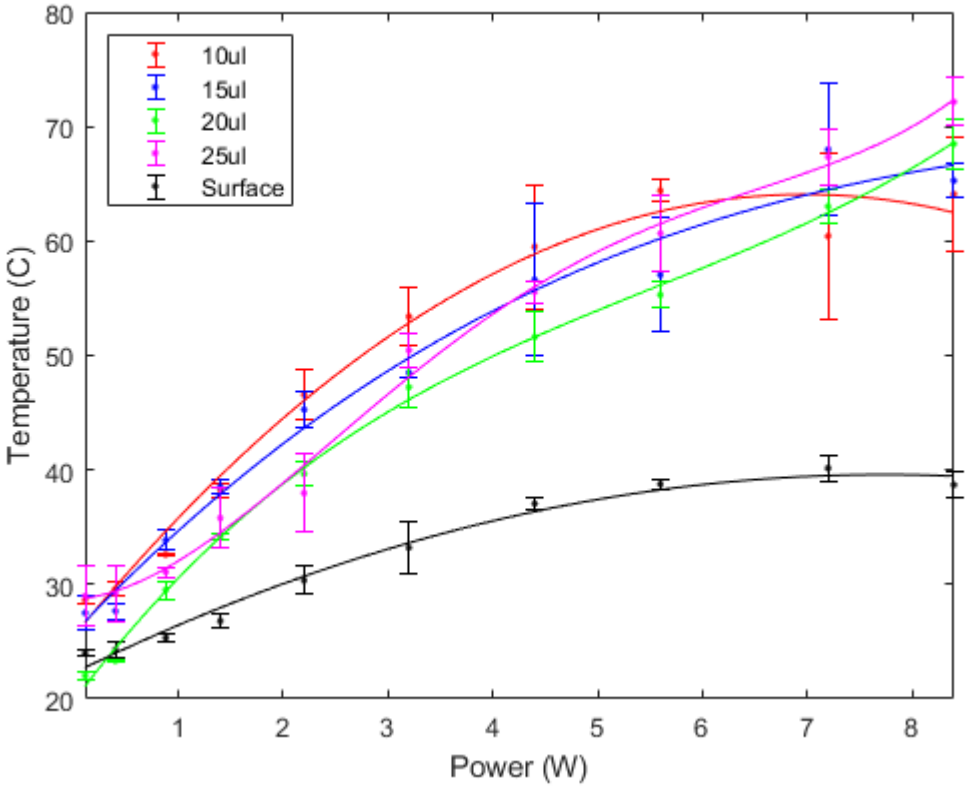

Figure 5.1 Temperature recordings for droplets at various sizes and surface using a constant input voltage (peak-to-peak)

During droplet manipulation, whether this is moving, mixing or heating, the surface shown in Figure 5.1 was heated up once the power was applied to the IDT. Heating of the IDT causes the electrodes to expand, thus increasing the distance between them, resulting in a change in the resonant frequency. As the distance between electrode fingers increases, the resonant frequency decreases. With a TCF value of -277.2 ppm, the SAW device driving frequency can be changed by 4 KHz per 1 ºC. When the temperature was increased up to 90 ºC during the PCR process, the frequency will be changed by -261.3 KHz. The signal generated is often fixed at the originally measured frequency at room temperature. In that case, the greater the temperature change, the worse the ability the SAW device to convert electrical energy into mechanical waves due to these significant frequency changes.

In order to mitigate this issue, the temperature change of the IDT was simultaneously monitored alongside the droplet's movement. This measurement data was used with the TCF value to calculate the change in frequency. This was then applied in real time to the IDT whilst the droplet was being heated. An example of the temperature and frequency changes is shown in Figure 5.2. This can be employed in any situation where the SAW device is being used to actuate, and thus reduces the load on the amplifier allowing for minor adjustment. Whilst this was using the thermal imaging camera that was already implemented in this platform, it is possible to adjust the frequency with any temperature measurement of the surface by a standard temperature sensor.

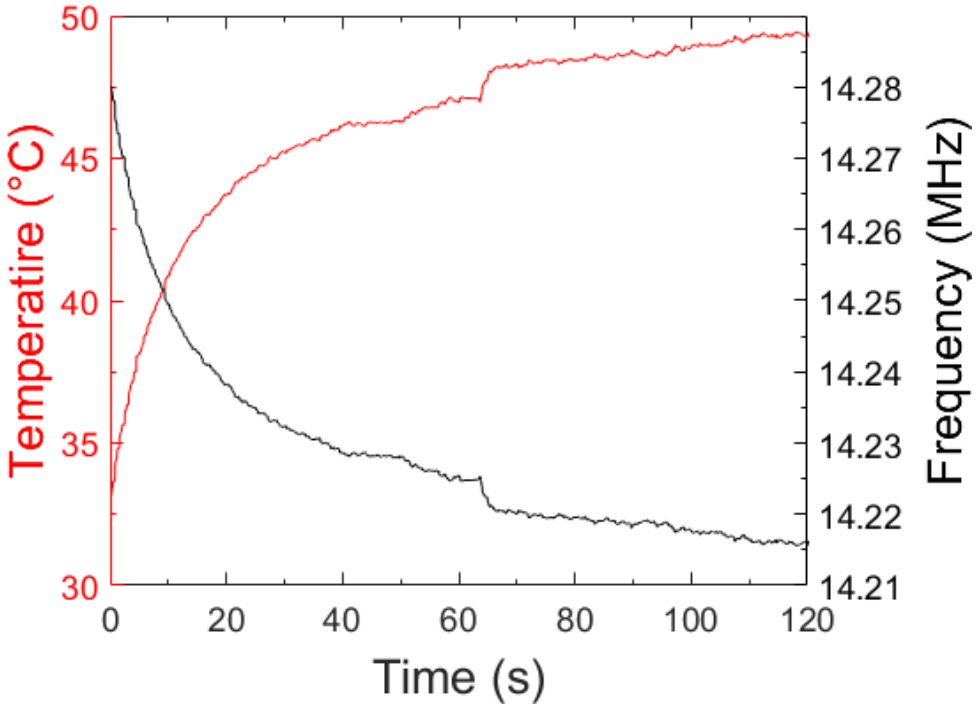

Figure 5.2 An example of temperatures controlled frequency [191]

5.3. PCR thermal cycling demonstration

The precision of this temperature control system allows for PCR to function and is capable of holding set points for 20 to 30 seconds. The set point can be automatically timed and changed as part of the Python program feeding into the PID controller. PCR requires high temperature and therefore it requires the application of a larger power output in order to rapidly gain temperature in each cycle. Using the full power of the 20 W amplifier, the droplet was able to reach 90 ºC in 30 seconds and then maintain for another 20 seconds. Once at the targeted temperature, its oscillations were found to be 2 to 3 ºC.

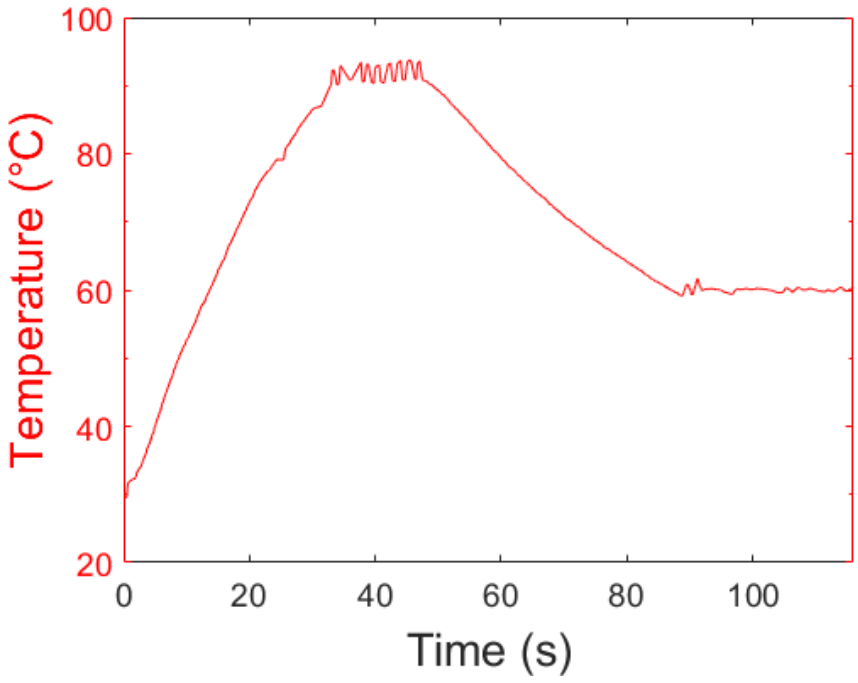

Figure 5.3 Single PCR cycle from room temperature to 90 ºC and down to 60 ºC

Accurate droplet anchoring methods were also necessary, as the use of high power would attempt to push the droplet out of the desired position. Some trails used a silicone rubber chamber in attempt to prevent the droplet position changing. Figure 5.4 shows the thermal

image capture on the GUI, and this image shows a chamber on top of a SAW device with a germanium lens placed on top to contain the liquid. Even with the chamber, the liquid has still been pushed to the far end of the substrate by the propagating acoustic waves. It should be noted that using germanium lens, which is thermally transparent and allows nearly 100% of the infrared ration through, there was some distortion making the temperature reading of the droplet difficult.

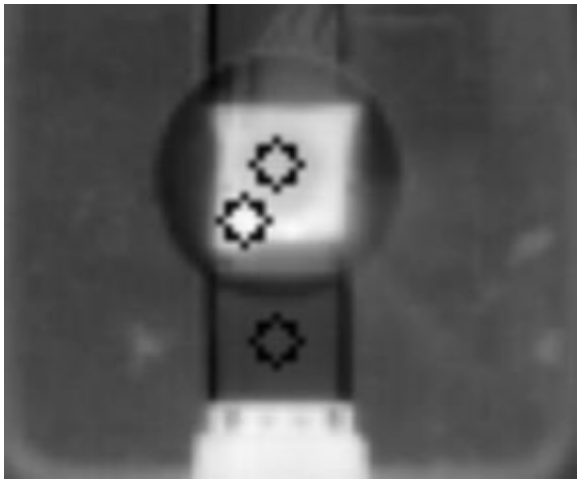

Figure 5.4 Thermal image of SAW device with chamber and germanium lens

Figure 5.5 shows an example of a few cycles of PCR temperature cycling (between 60°C and 90°C). In a PCR reaction this routine normally lasts for 40 cycles [158].

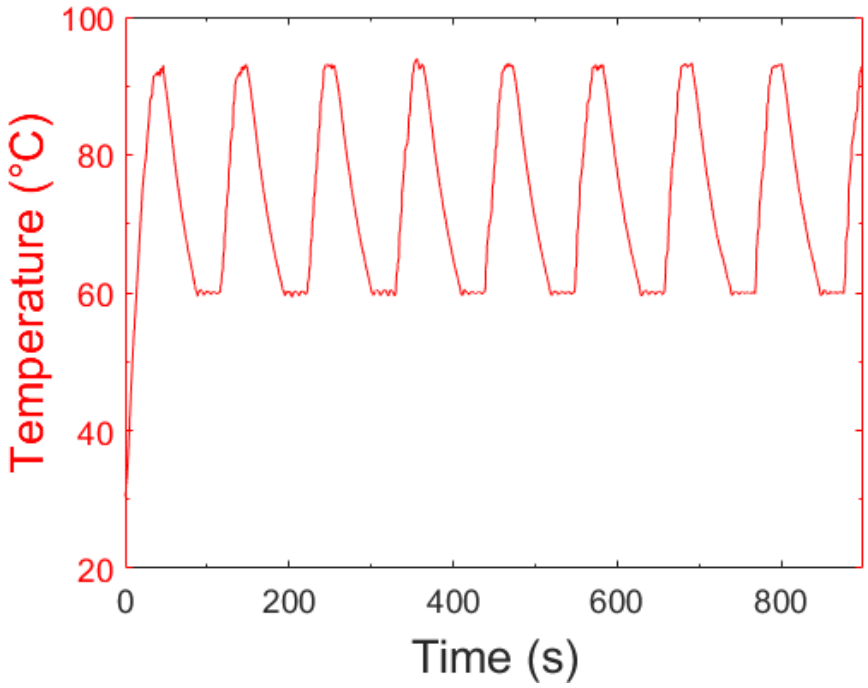

Figure 5.5 Example of droplet temperature control simulated PCR thermal cycling [191]

5.4. LAMP Temperature PID control

In LAMP reactions, the sample is typically heated to 65°C for 20 to 30 minutes [161]. Figure 5.6 shows an example of the LAMP process, and the device reached and maintained at 65°C, demonstrating the control function of droplet heating using the PID controller. The droplet was heated to the temperature of 65°C and maintained for 2 minutes. The time taken to reach the target temperature from 30°C took 35 to 40 seconds. The settling time took another 10 to 20 seconds with an overshoot of 2%. Once at the targeted temperature, the algorithm was able to stabilise and maintain the temperature with an accuracy ±0.3°C. The accuracy of the temperature was similar to that of a certified thermal cycler. LAMP reactions are normally operated efficiently between 60°C and 70°C, making this platform easily suitable for DNA amplification assays. From the thermal-requirements point of view, LAMP is simpler than PCR as only one fixed lower temperature is required. The requirement of only 65 ºC instead

of 90 ºC reduced the overall demands on the power outputs of the system. The Raspberry Pi only needs to read and maintain one targeted temperature, therefore the PID controller can be tuned for this specifically targeted temperature. The power required from the amplifier can be much lower.

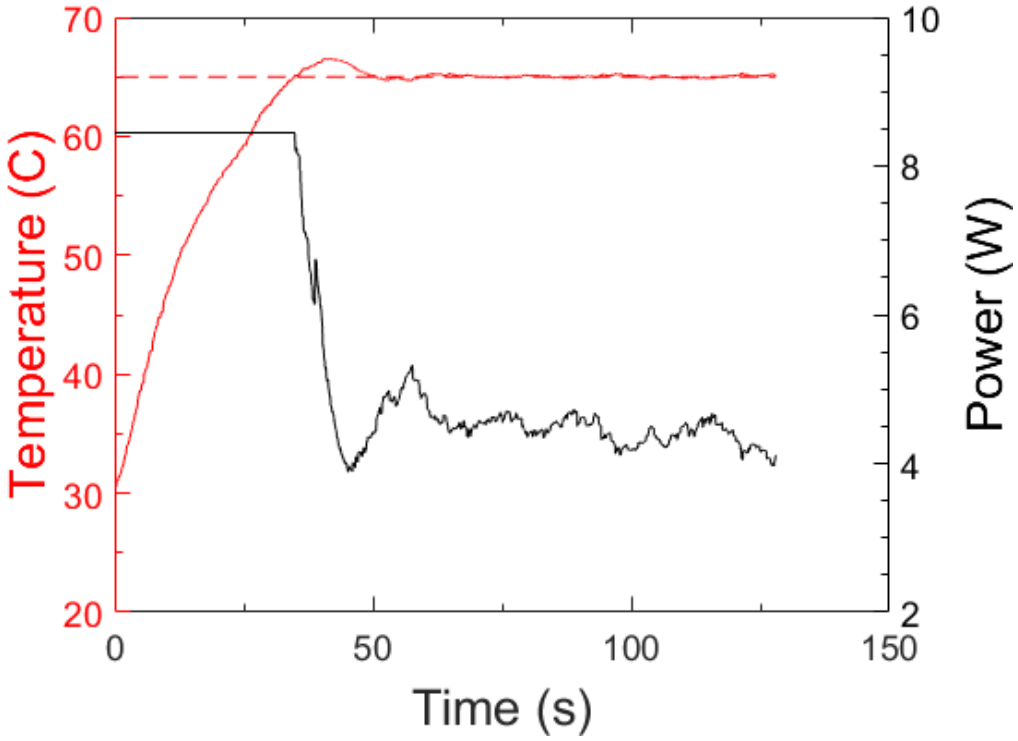

Figure 5.6 Example of droplet temperature control simulated LAMP thermal process [191]

5.5. Fluorescence detection

Figure 5.7 shows the fluorescence signals of droplets with different volumes, indicating varied fluorescent levels. Adjusting the volume of the droplet affected the recorded brightness obtained by the camera. This variation could be as large as 15% of the maximum intensity, because of the difference in the area to absorb UV light and emit blue light. As the

concentration of quinine was increased, the measured fluorescence signal was increased. As the solution was further diluted with the DI water below 20 ppm, the fluorescence intensity began to rapidly decrease down to 8 ppm quinine (e.g., 10% of the initial quinine concentration). At this point, with the current camera and settings, it was no longer possible to distinguish the droplet from the pure DI water.

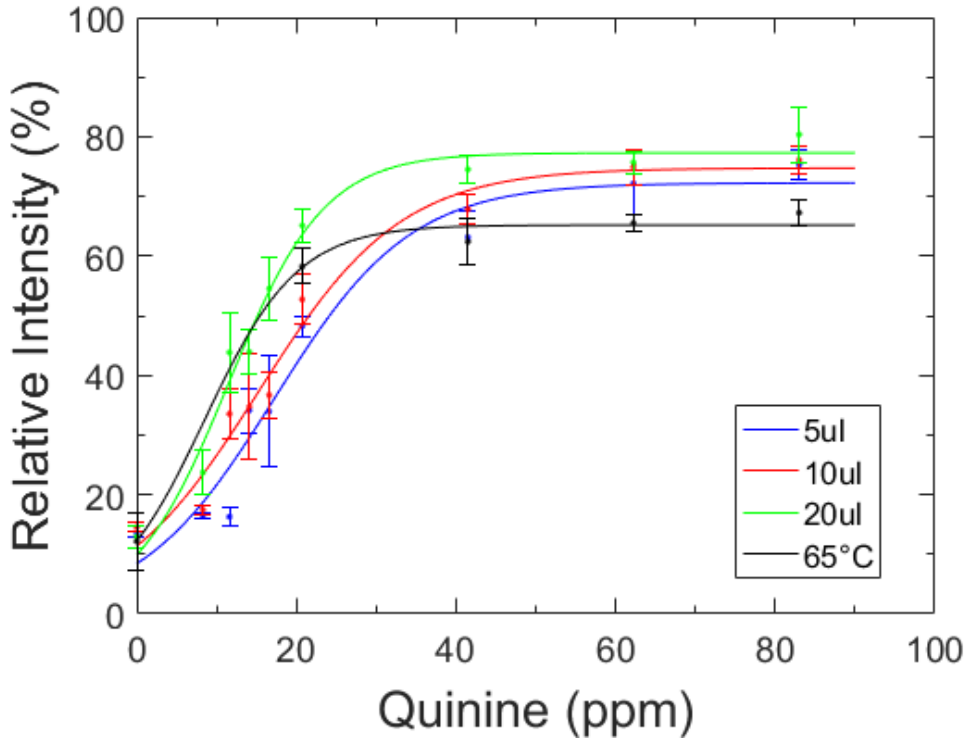

Figure 5.7 Fluorescence concentration and relative intensity, measured at room temperature and 10 µl at 65 ºC [191]

Figure 5.8 shows the measurement results for the real time mixing. Starting with 5 µl DI water, the digital filter detected no value of the signal. When a 5 µl of Quinine solution was mixed with the water driven by the SAW from one side, the brightness was increased. The growth of intensity was more significant for the first mixing of solution, and further introduction of solutions resulted in stagnated increase of intensity (because of the increase of total volume of the droplet). There were also noise signals introduced as the droplets were

merged and mixed before settling. Increasing the quantity in the solution also reached a point where further increasing the concentration did not yield further fluorescent intensity. This shows the systems capability of mixing and measuring fluorescence simultaneously

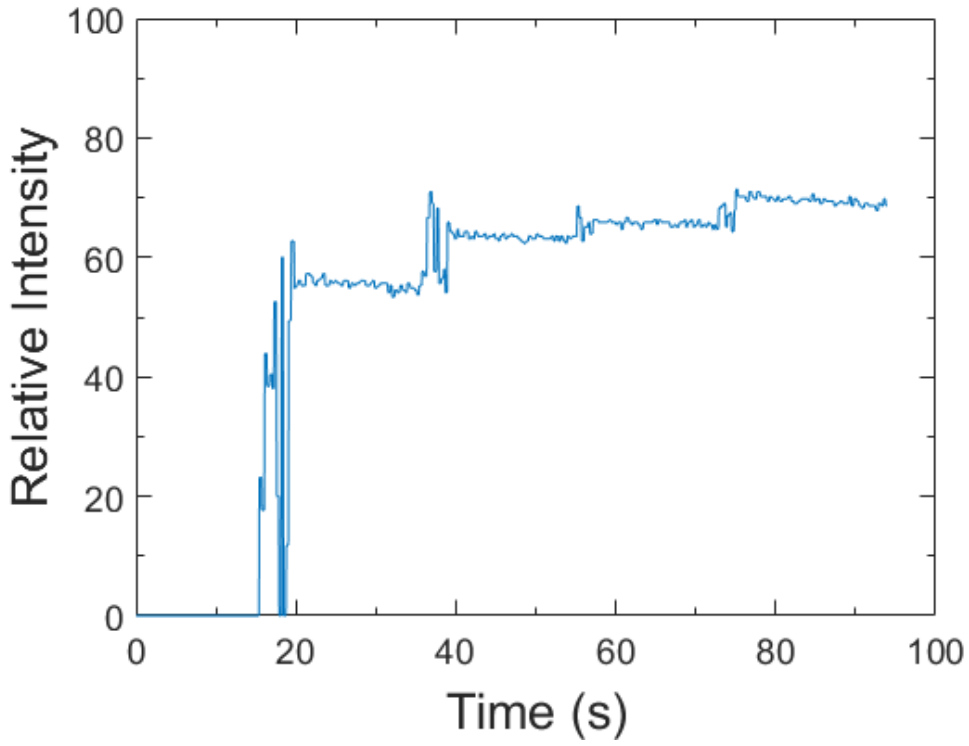

Figure 5.8 example mixing of fluorescent droplets over time. [191]

5.6. Summary

In this chapter, we have provided a methodology for thermal control and fluorescent detection using open-source electronics, surface acoustic wave device and a Raspberry Pi as the basis for the platform. The acoustic energy from the SAW devices was capable of heating small sample sizes to meet the requirements for LAMP and PCR with a high degree of accuracy. During droplet heating, the thermal imaging camera was used to monitor the SAW device itself, adjusting the frequency output leading to more efficient use of the acoustic waves.

The temperature difference between the surface and the droplet opens up the possibility to control temperature without the need for a thermal imaging camera. Using the surface temperature or even the frequency shift and the TCF equation, [12] the temperature at the droplet can be monitored precisely.

Anchoring the droplet in place during high powered heating was difficult due to the acoustic wave propagation causing the droplet to move. An alternative method to a chamber could be engaging multiple IDT from different directions to stabilise the droplet's position.

Whilst the temperature of the droplet is being controlled the system is also able to monitor the droplet fluorescence using the Raspberry Pi camera. This was done using digital filters removing the need for expensive optical filters which would also need to be exchanged for different fluorescing wavelengths. The digital filters were able to be tuned in the software using HSU colour values and camera settings.

The next stage in this project would be to reduce the cost by removing large components such as the signal generator. Being able to use a DDS module or even a signal directly from the raspberry pi would lower the cost of building significantly and allow for the platform to be potentially portable.

A recent low costs PCR system proposes using Raspberry Pi, a camera, an optical filter setup, LEDs and Peltiers [201]. This system has a low cost of approximately £271.97

because of the use of Raspberry Pi, and LEDs, there setup requires manual preparation and mixing of reagents similar to started laboratory based assays. Whereas the most expensive part of our setup is currently the signal generator and amplifier uses to power the SAW device for both the mixing and heating of the samples.. for the cost to be reduced further in our setup, the signal generation should be addressed, by replacing the generator with either a DDS module or directly generator a signal from the raspberry pi and potentially using a smaller amplifier.

Chapter 6. Breath monitoring, sleep disorder detection and tracking using SAW devices combined with open-source electronics

6.1. Introduction

In this chapter, we investigate the ability of the SAW-Raspberry Pi platform to track and analyse breathing and its potential to detect breathing disorders. We will aim to understand the components in breathing that use the SAW devices and look to combine this understanding with embedded electronics.

We will use the SAW-raspberry pi platform to interface with a vector network analyser (as explained in Chapter 3), record the frequency spectra and automatically track the changes in the frequencies.

The system concept is suitable for any SAW device regardless of its fabrication and composition. We employ thin film SAW devices with bimorph Al/ZnO structure due to its potential to fabricate flexible SAW devices [202][18]. Such SAW devices made with Al foil can be made to be flexible and mounted on the upper lip of the patient, fitting comfortably and allowing adequate SAW humidity sensing during sleep. The device can also be designed to attach to the upper lip in a breathing mask [80][202]. Wireless connections to the embedded controller unit can be applied. Further advantages of thin film SAW technology include industrial scalability and ultra-low-cost fabrication potential. In addition, thin film

SAW devices have been shown as good temperature and humidity sensors for human breathing monitoring applications [88].

A description of the platform is in Chapter 3

6.2. Frequency responses to humidity and temperature

6.2.1. Effects of a singular breath to humidity

Figure 6.1 is an example of the recorded data from one prolonged exhale onto both the SAW device and the commercial sensor DHT22. This example is typical of what will happen when a patient is asked to take a deep breath, then exhales towards the SAW device. The SAW device has a rapid change in its frequency, taking ~1.4 seconds to shift 50 KHz and taking ~11 seconds to return back to the fundamental frequency of 14.276 MHz. The DHT22 sensor takes a much longer time to respond to the same breath cycle. For example, it takes 7 seconds to respond to the exhale, and ~35 seconds to return back to the relative humidity of the ambient environment. For the reference, the peak value of the relative humidity in the breath is 77 %, which is an increase of 25 % from the ambient value of 52 %. It is worth noting that according to the DHT22 data sheet, it is not possible to monitor breathing responses using the DHT22 sensor, as it takes on average 5 seconds to reach the maximum humidity values [203].

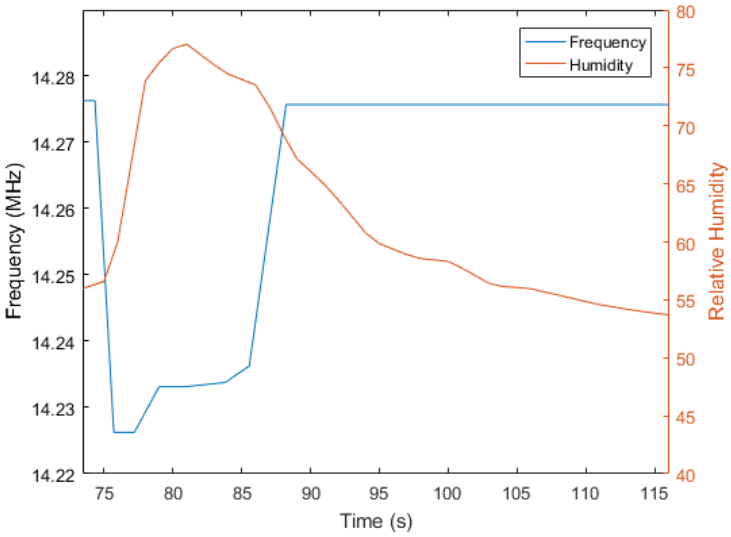

Figure 6.1 A singular breath, the effect of humidity on frequency

6.2.2. Multiple breaths

The following recorded test consisted of 10 breaths. Figure 6.2 shows the obtained frequency results for 10 breaths as functions of humidity and temperature. Humidity values have significant variations for each breath, with an increase of 10 to 20% relative humidity values as shown in Figure 6.2 (a). Temperature values shown in Figure 6.2 (b), on the other hand, have a minimal change during breath cycles over the duration of the tests. Longer duration of a breath affects the change in temperature, and the recorded largest change value is an increase of 2 ºC.

There are two possible factors that could affect the temperature readings on the SAW device. One of them is the temperature of the patients breathing. The temperature inside a typical healthy human body is 37 ºC. A breath that is exhaled can be around 34 ºC [204]. The temperature of the SAW device was around 21 degrees Celsius and every breath onto the SAW device had an influence on the temperature increase. The other factor is the

environment temperature changes. The increase of ambient temperatures caused the device's temperature changes, as this group of results were recorded on a warm-summer day of around 25 ºC in a room without any temperature regulation (Figure 6.2 (b)). This can be clearly seen that even with a small pause between tests the temperature continued to rise without any sign of drops between different recordings. Although the ambient temperature changes do not appear to greatly affect the frequency changes during the breathing cycle over time this could become an issue. Any significant or rapid changes in ambient temperature could add problems for tracking these breaths. Additional temperature control or calibration using the raspberry pi would prevent this problem.

In these initial tests, the device was held below the volunteer's nose perpendicular to the flow direction. Ideally, the device should be mounted parallel to the air flow directly below the nose. These tests show the results which belonged to slower but deeper breaths. When exhaling longer or harder breaths a greater amount of gas and water vapour was expelled from the volunteer. The moisture droplets were deposited on the surface of the SAW device, which took some time to clear, thus increasing the signal recovery time to the fundamental frequency.

It is clear from these results that the SAW device responded much quicker to humidity change in comparison to that from the commercial DHT22 sensor, possibly due to the larger surface area of the DHT22 sensor for moisture to accumulate and then evaporate. When

breathing longer or stronger, the DHT22 sensor became saturated, whereas the SAW device showed a larger shift in frequency.

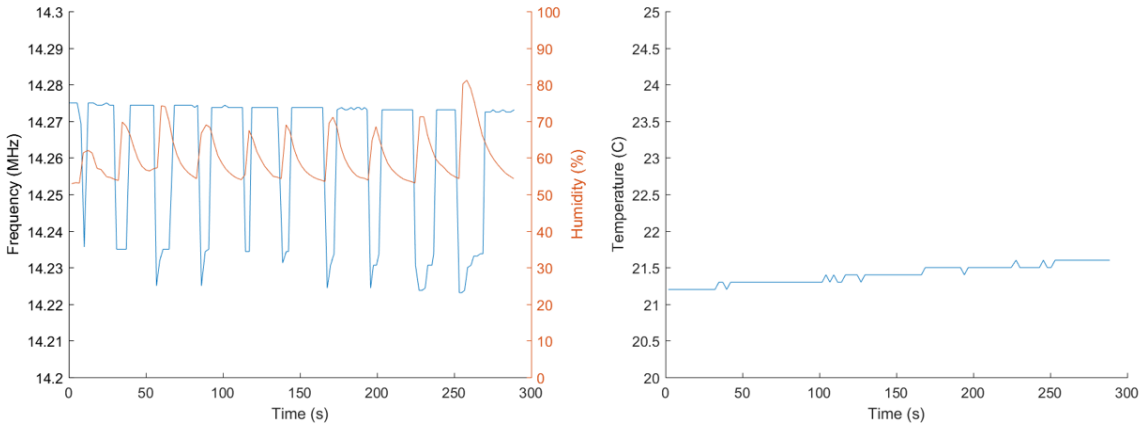

Figure 6.2 (a) 10 exhale breaths of approximate same duration and strength (b) temperature over test duration [192]

6.2.3. Effect of deep and shallow breaths

In Figure 6.3 (a) there are 11 breaths recorded over 5 minutes. The results shown in Figure 6.2 (a) and Figure 6.3 (a) are aiming to check the consistency. They are very similar, with the maximum frequency shifts varied by 13 kHz. This is most probably due to human error recreating the same exhale strength and duration every time, as well as the minor differences in distance and position of the SAW device and DHT22 relative to the user's nose.

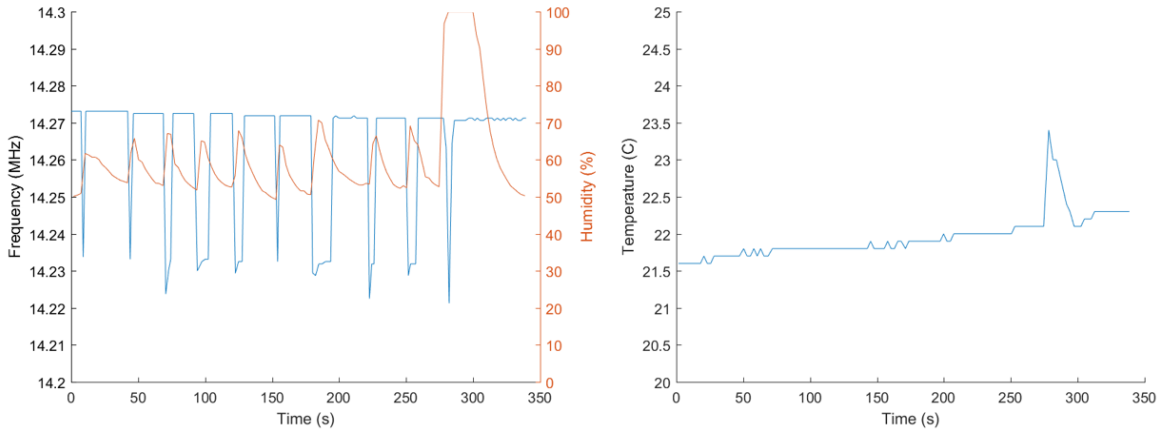

Figure 6.3 (a) 11 deep breaths including saturated humidity sensor (b) temperature over time of 11 deep breaths

The 11th breath in Figure 6.3 shows both saturation in humidity and a noticeable spike in temperature. This is likely a human where the exhale was to close the the DHT22 and not the SAW sensor. This has the largest change in frequency with a value of 50 KHz but has one of the quicker recoveries, whilst the humidity and temperature show the largest recorded peaks and recovery times. The main reason is that the temperature and humidity readings were obtained from the commercial sensor (which was very slow to respond), whereas the frequency signal was from the SAW device which is much faster.

The commercial DHT22 sensor is useful for reference and data logging environmental changes throughout the tests. In comparison, the SAW device is able to react much quicker to the fluctuations in both temperature and humidity, making it much more suitable for monitoring breathing.

6.2.4. Changing humidity and temperature with hot air

In order to observe the effect of humidity, hot air was applied to the device's surface in order to reduce any moisture on the device. However, this also largely increased the device's temperature. Figure 6.4 shows the frequency shift of the SAW device, and changes of temperature and humidity obtained from the DHT22 sensor. Using the previous method and the TCF values, the temperature fluctuations were removed, and we obtained the data of yellow-coloured "filtered" signal results shown in Figure 6.4. As the temperature caused the device to expand, the speed of the waves decreased, therefore, the fundamental frequency of the device decreased. Reducing the humidity, on the other hand, increased the frequency by enhancing the wave propagation with less water mass loading on the surface. After the filtering, the resultant signals clearly showed increases in the frequency due to the removal of humidity effect (Figure 6.4).

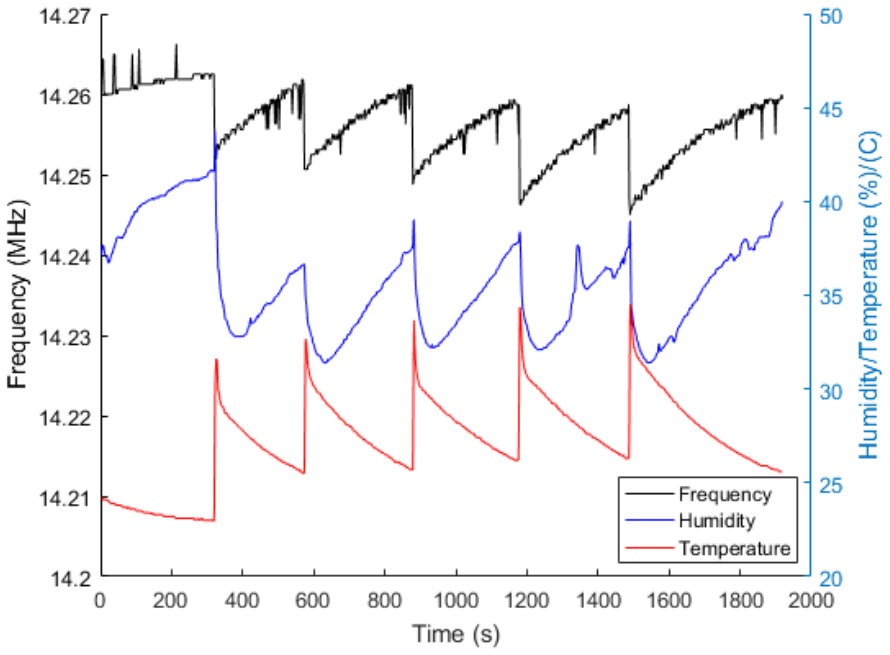

Figure 6.4 Effects of hot air to the frequency shifts of the SAW device

6.3. Humidity effects on Frequency

Error! Reference source not found. shows data of frequency and humidity extracted from t he deep breathing and heating results, recorded with the SAW device and DHT22 for the humidity. Both parts recorded on different days produces a gap in data between both sets. There are only minor changes of frequencies when the humidity is below 50%. Above 50% relative humidity, the frequency data was recorded from the deep breathing. This half of the data clearly showed a trend of a rapid increase in frequency shift as the humidity approached 80%.

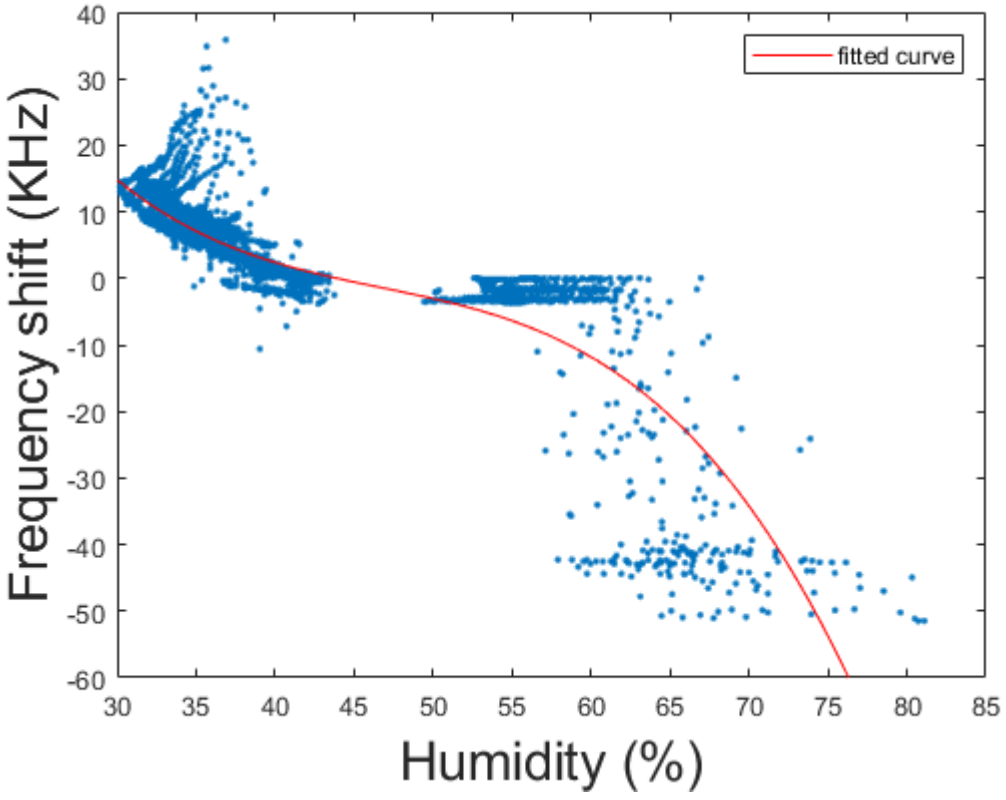

Figure 6.5 Combined heating and breathing tests to calculate humidity effect on frequency

This data was acquired in the field during breath tests, instead of in a controlled humidity chamber, there were other factors affecting the frequency shifts such as temperature.

Temperature had a much stronger influence in the hot air tests, which can be clearly seen from the results below 45% relative humidity. As the humidity level lowered, the change in frequency appeared to increase. Calculations to filter the effects of temperature were performed, however it is reasonable to assume that the calculations were not perfect due to potential data errors. Other contributing factors could have been the response time of the commercial sensor. The humidity was constantly changed, which affected the commercial sensor, as it required 1 or 2 minutes to produce accurate readings. Equation (6-1) was derived from Figure 6.5.

The trend of frequency shifts (Δf) as a function of humidity levels (X) can be fitted using the following equation:

$$\Delta f = -0.001717\text{x3} + 0.2409\text{x2} - 11.75\text{x} + 197 \quad (6\text{-}1)$$

Figure 6.6 shows an example of relative humidity effect trend on the SAW device's frequency. This device was placed in a chamber where the relative humidity was increased by increasing the nitrogen flow rate though a water tank and then flowing over the SAW device. Compared to the results shown in **Error! Reference source not found.**, Figure 6.6 reveals that they both have a similar nonlinear relationship, indicating that this device can be used to monitor the relative humidity changes caused by breathing.

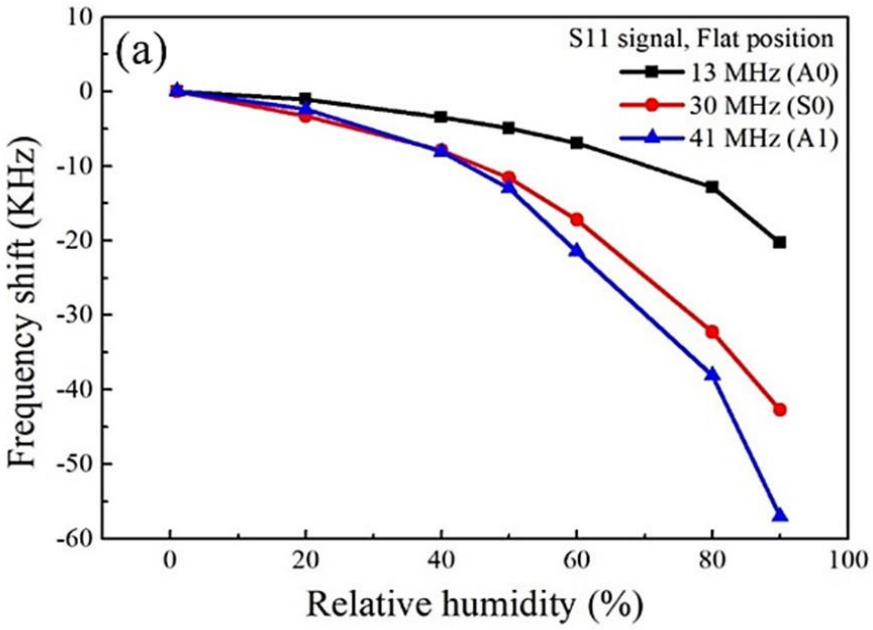

Figure 6.6 Frequency shifts of various vibrating modes in response to changes of relative humidity, graph from sameer [205]

6.2.5. Different frequencies and reflection/transmission modes

A SAW device with a frequency of 42 MHz was tested in both reflection and transmission modes. When compared to the 14 MHz device, this device's frequency had been shifted by 200 KHz as shown in Figure 6.7, which is 5 times as much as that of a single breath shown in Figure 6.1. This frequency change happened in 2 seconds but took 20 seconds to recover. This device had a smaller area between IDTs and much finer IDT finger structures, which will possibly affect the device's response time.

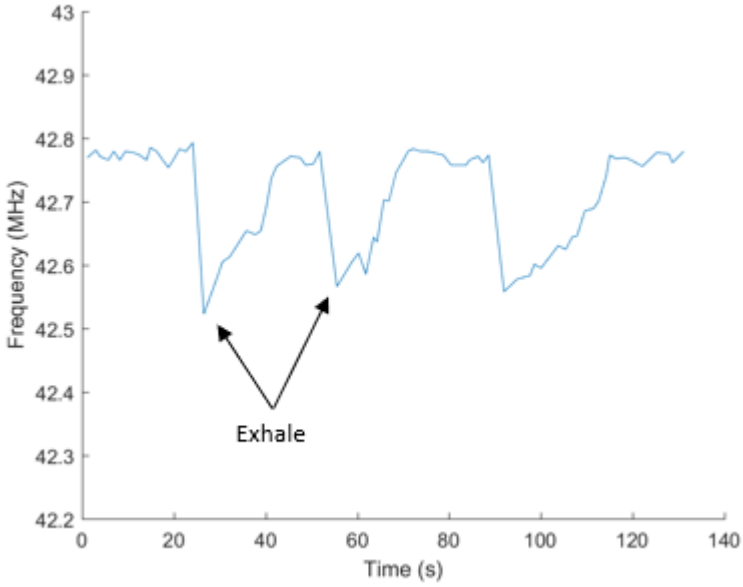

Figure 6.7 42MHz SAW frequency shift caused by breathing

The base line signals during these experiments have a higher level of noise (see Figure 6.8). This is because of the quality of the IDT used the S11 peak (Figure 6.8) has a relatively poor quality, therefore, finding the lowest point to track the signals becomes more difficult.

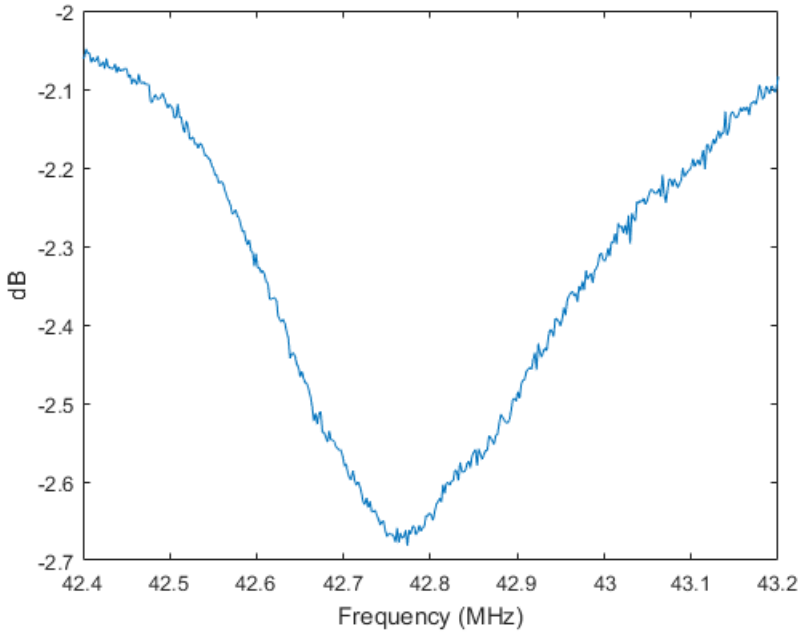

Figure 6.8 S11 spectrum of 42 MHz SAW device

The frequency spectrum for S12 transmission signals is shown in Figure 6.9. It also shows a low quality peak, which causes apparent noises during frequency measurement of the breathing process.

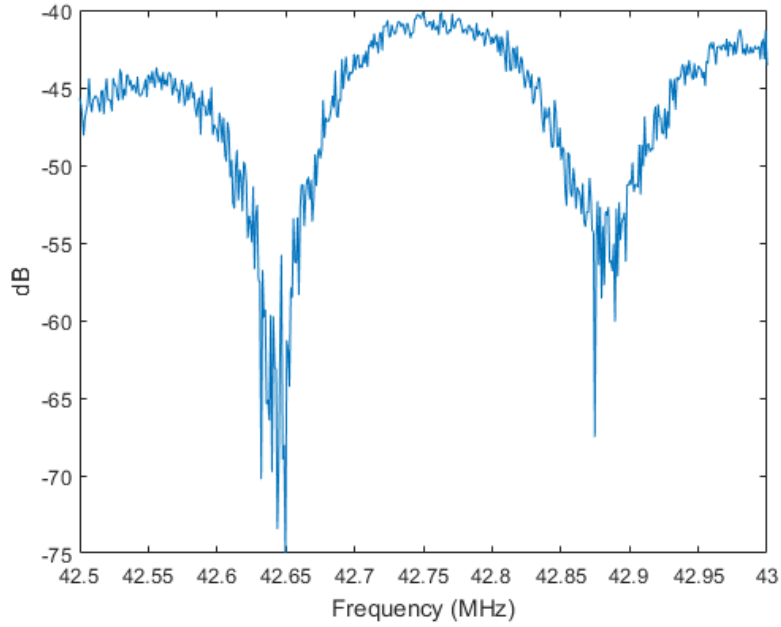

Figure 6.9 S12 spectrum of 42 MHz SAW device

Figure 6.10 shows five cycles of exhales whilst measurements are taken from the S12 transmission mode. The frequency change is ~200 KHz. These measurement data also show that it takes 2 seconds for the frequency shifts, and then takes 20 seconds to return to the original signals. Because the signal quality of S12 has greater noise when compared to the S11 signal, it is easily the cause of fluctuations in the data. The possible cause is a miss match in IDT frequencies.

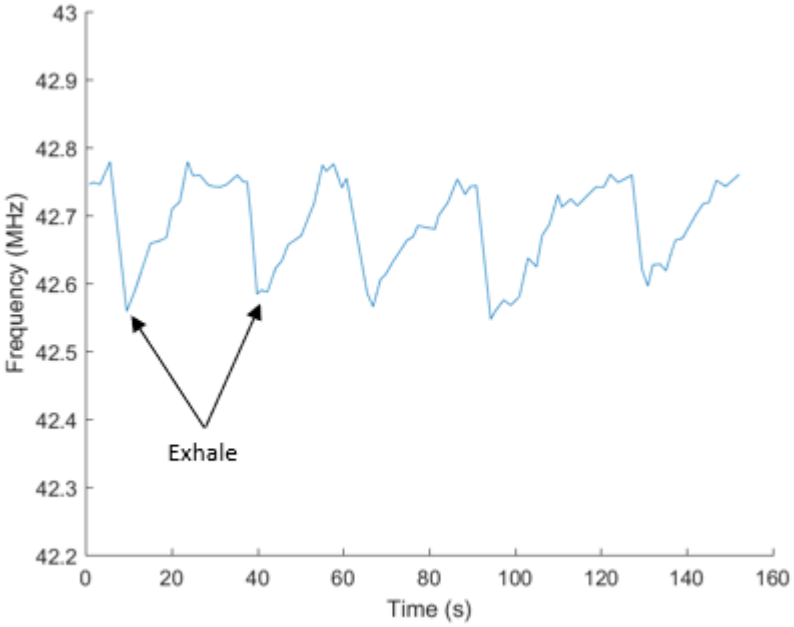

Figure 6.10 42MHz SAW device S12 breath detection

The test with 42 MHz showed that using this higher frequency would result in a more sensitive measurement setup, potentially being able to detect much weaker breathing. However, this particular device took a longer time to recover, meaning quick breaths may not be detected easily.

6.3. Temperature compensation

In order to obtain the actual frequency shift caused by humidity changes, the TCF of the device was used to estimate the frequency shift caused by temperature. This enabled the frequency changes from temperature to be calculated and deducted from the original signal. This could also be employed in real time on the embedded system when sensing is underway.

Figure 6.11 (a) is frequency and temperature data alongside the calculated changes in frequency of the SAW devices for 5 breath cycles. Figure 6.11 (b) shows the results of 10 breaths over a longer period. As the test is underway the recorded temperature is gradually increased by approximately 0.5 degrees over 5 minutes. Using the calculated TCF of the device, it is possible to deduct the effects of temperature on the frequency shift. This will remove the effect ambient temperature changes have on the signal, thus allowing for easier signal processing to detect each breath.

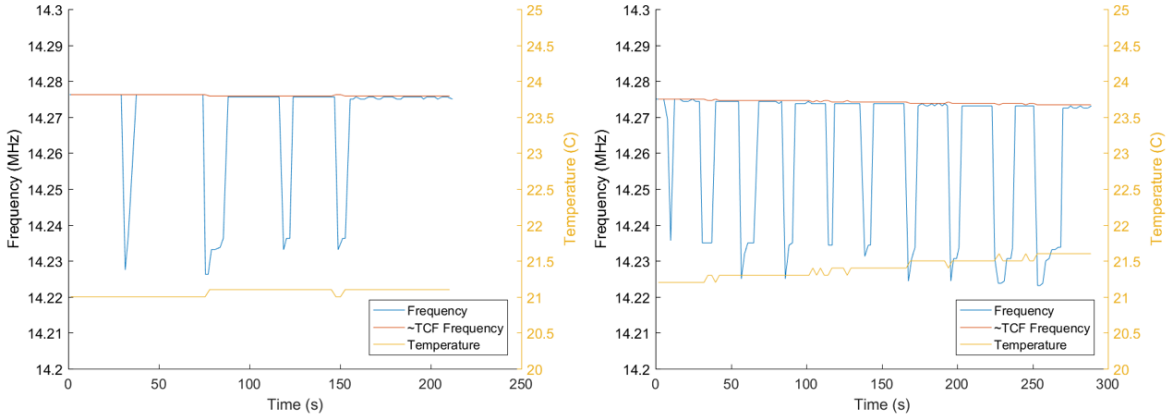

Figure 6.11 Frequency, temperature and TCF (a) 5 breaths test (b) 10 breaths test

6.4. Continuous breath detection and monitoring

Figure 6.12 shows recorded data and the points (plotted as asterisks) that the python script detected as a breath. The bpm was calculated based on the time recorded between peaks and averages out over 1 minute. This fairly simple breath detection method looks for the falling

edge of each breath, running live as the breathing is happening. The time before the next breath is recorded and the estimated breaths per minute is calculated. The data is then averaged out as there are variations between breaths within one minute. These calculation data results are shown in Figure 6.13. The most common method of monitoring breathing is to manually count the number of breaths over one minute. Our method is proven to be as accurate as manually counting within 1 breath per minute. The peak detection requires to set the thresholds for rising and falling edges of the breaths. If the range at which the frequency shift changes then this method does not work robustly. This is where the compensations for other aspects such as temperature are required to maintain a flat baseline frequency.

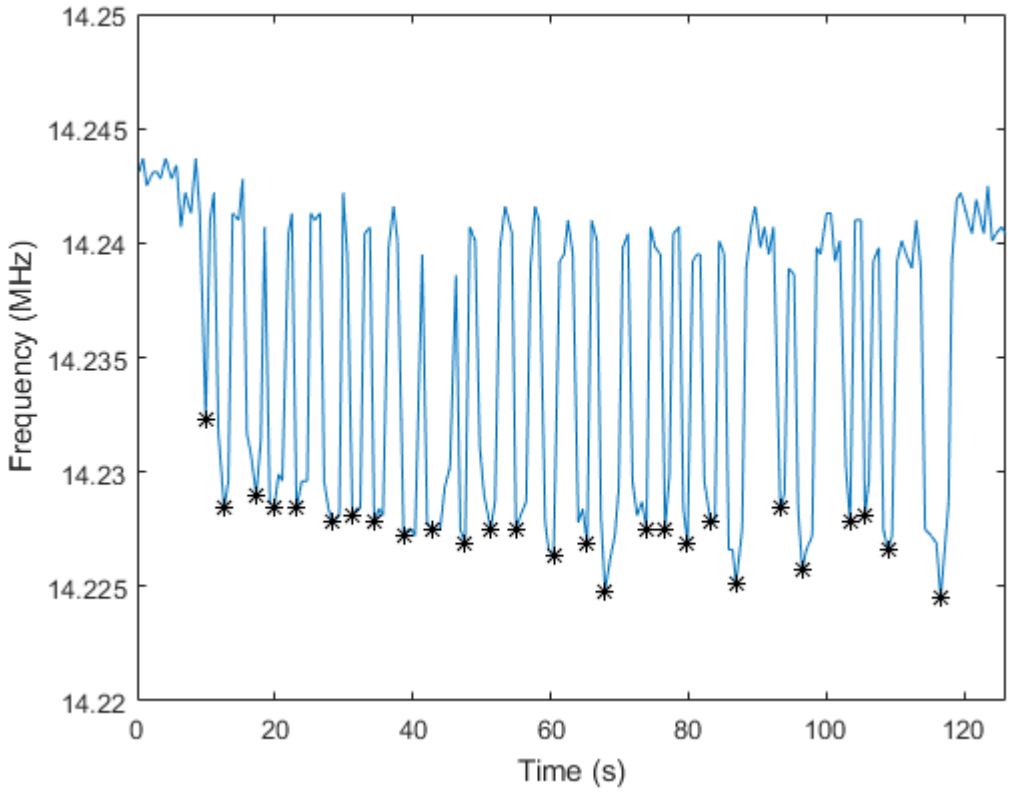

Figure 6.12 Continuous normal breathing and detected exhales

Figure 6.13 shows the respiration rate and average calculated over the 1-minute period test. These calculations are run in real time as the frequency is recorded. This enables the Raspberry Pi to detect any chances to the patient and check if the breathing is within a typical range. Counting the number of breaths in 1 minute window from Figure 6.12 reveals 15 to 16 breaths per minute, showing the average calculated is the same as those from the manual methods.

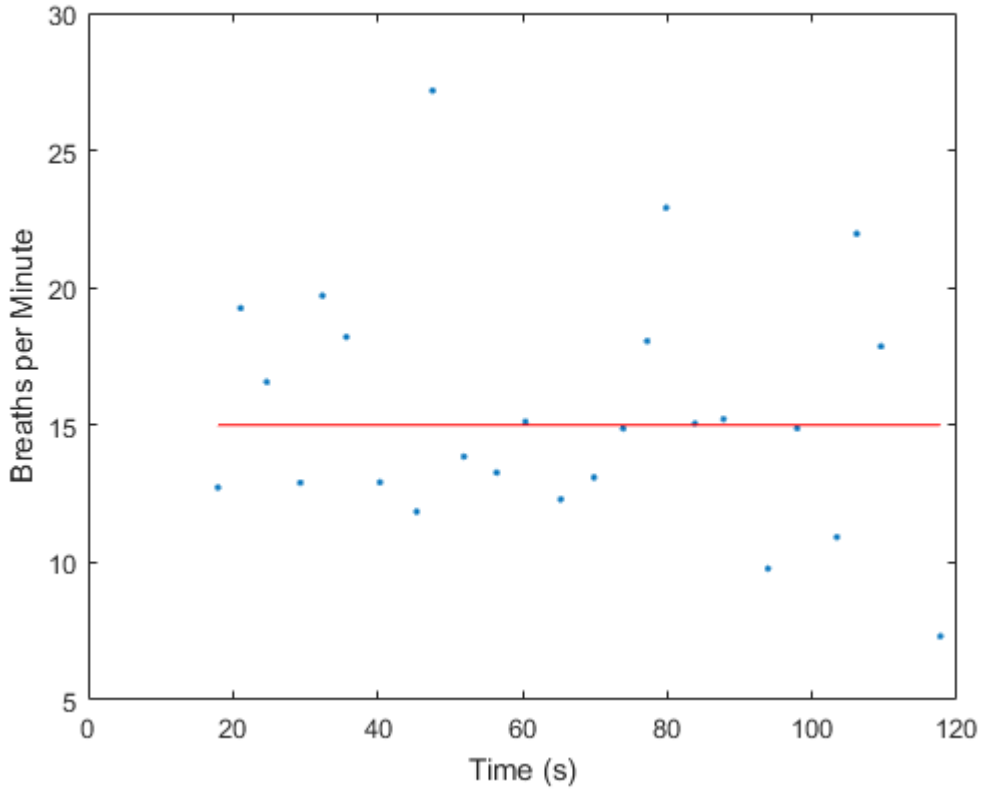

Figure 6.13 Calculated breaths per minute

Figure 6.14 represents a phenomenon of breathing disorder such as apnoea. It shows that breathing is normal with a period of 30 to 50 seconds, when no breathing has occurred. This is the raw frequency data captured from the SAW device and the calculated breaths per

minute. It is visually shown when the user has stopped breathing and when the breath is resumed. The detection algorithm shows that the data of breaths per minute momentarily drops below the average breathing rate or completely to zero. This could be used to trigger the alarms for a person's health when the breathing is beyond the user's normal range. There is also the potential for machine learning algorithms to be implemented in order to learn the normal breath behaviour of a patient, further increasing the accuracy and detecting when the patient may require medical attention.

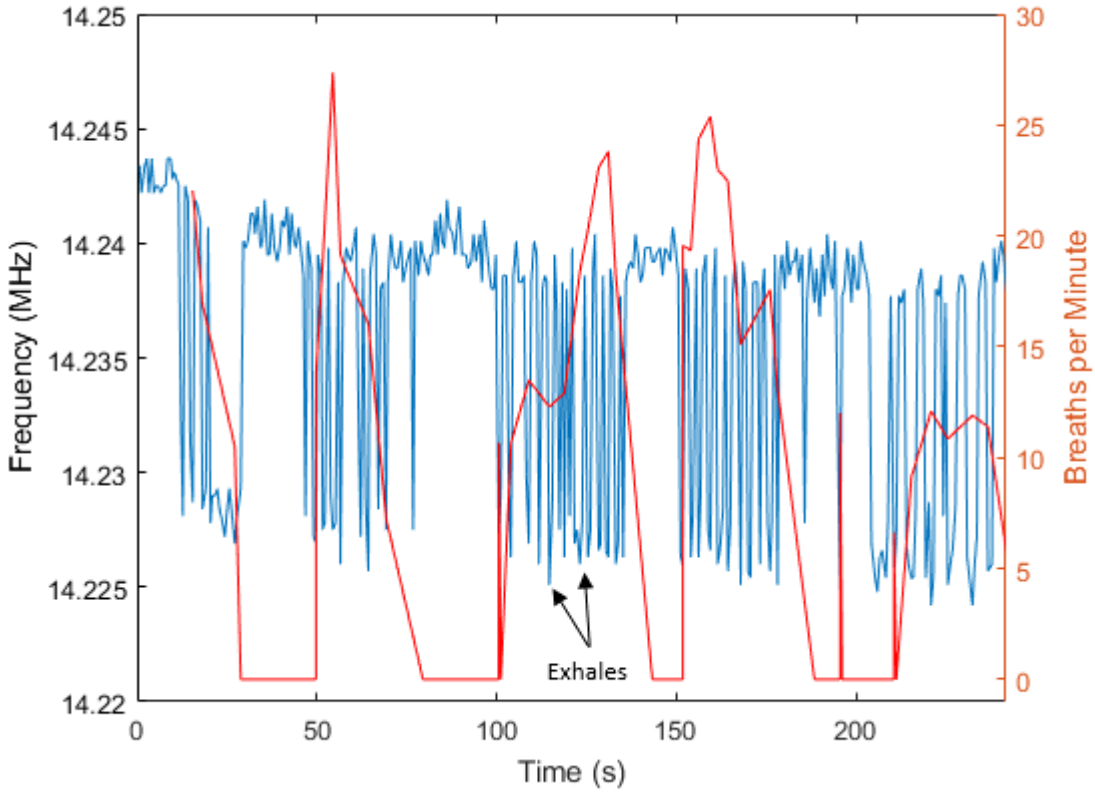

Figure 6.14 Demonstration of a breathing disorder and calculated breaths per minute

6.6. Summary

In this chapter the thin film SAW platform has been demonstrated for the application of breath detection and monitoring. The effects of breath are shown to be largely caused by humidity, temperature will also influence the SAW device.

Visible changes can be seen from the data of deep breaths to multiple normal breaths leading to the potential to analyse how a patient is breathing. Deep breaths are shown to be significantly linked to the changes in relative humidity, while small spikes in temperature also influences it. Using the raspberry pi in combination with a commercial sensor such as the DHT22, the platform has the potential to filter the environmental effects such as temperature influence from the signal in real time.

Once the environment is filtered out, there is a potential to automatically calculate the respiration rate of the patient in a non-invasive way. The time between breath is recorded and the average rate of breathing is calculated in 1 minute. The Raspberry Pi is connected to the internet, meaning the recorded data can be sent to the cloud or recorded on board the Raspberry Pi and the alerts or alarms can be sent when the respiration drops below the average breath per minute for the patient.

The next stage in this project to reduce cost further would be eliminating the use of a network analyser. One method when working with reflection method would be to implement bidirectional coupler circuitry to measure transmitted and reflected signal send to and from

the SAW device. The implementation of a frequency counter circuit would allow for measuring the transmitted SAW signal, when sensing.

Chapter 7. Cell stimulation and growth with SAWs

7.1. Introduction

When SAW is active during cell culturing, there are a few major effects on the cells during their growth. The first is the mechanical waves propagating on the SAW device's substrate and the wave energy is transferred via ultrasound gel onto the cells adhered on substrate or in the liquid. When the mechanical excitation stimulates the cells, the temperature is also increased during the SAW operation. The cells used require a temperature of 37 °C. Increase of this temperature will reduce the growth rate of cells and increasing too much will damage the cells where they can't be recovered, killing off more cells.

In this chapter we investigate the application of thin film SAWs in cell culturing. Surface acoustic waves will be applied to living cells at various intensities and durations to understand the effect on the proliferation rate of cells. The SAW is implemented and controlled using the raspberry pi platform.

A description of the platform is in Chapter 3

7.2. Cell excitation and temperature

Table 7.1 lists all the SAW devices and their frequencies, and the cell types used. Multiple aluminium foil SAW devices were used with most of frequencies at around 13 MHz.

Table 7.1 SAW devices and cell types used in cell stimulation

Cell type	**SAW device**	**Frequency**
C2C12 myoblast	Al foil 50 um	13.209
C2C12 myoblast	Al foil 50 um	13.044
C2C12 myoblast	Al foil 50 um	13.125
Fibroblast	AL plate 200um	14.035
Fibroblast	AL plate 200um	14.193
Fibroblast	AL plate 200um	9.489
Fibroblast	AL plate 200um	27.071

As shown in Figure 7.1, when applying SAW, the heat is generated on the SAW substrate and distributed outward across the culture plate. With a constant SAW activation, the temperature is increased up to 10 °C. The cells are kept in an incubator already at 37 °C and therefore any major increases in the SAW power affect the cells and the experiments. The temperature range is from room temperature of 17.1 ºC which shows up in dark blue. The scale goes up to 21.2 ºC, and anything beyond this point is bright white. Sp1 is a spot which highlights the central well above the SAW IDT. The SAW device is situated below a 96 well plate. The connecting wires from the amplifier can be seen at the top left of the image. Figure 7.1 also shows the temperature distribution through the plate when SAW is agitated. The

SAW substrate is the main source of heat, especially centrally located over the source of the acoustic waves. The temperature changes fairly rapidly, and it is near room temperature for the 2 wells approximately 2 to 3 cm away from the centre.

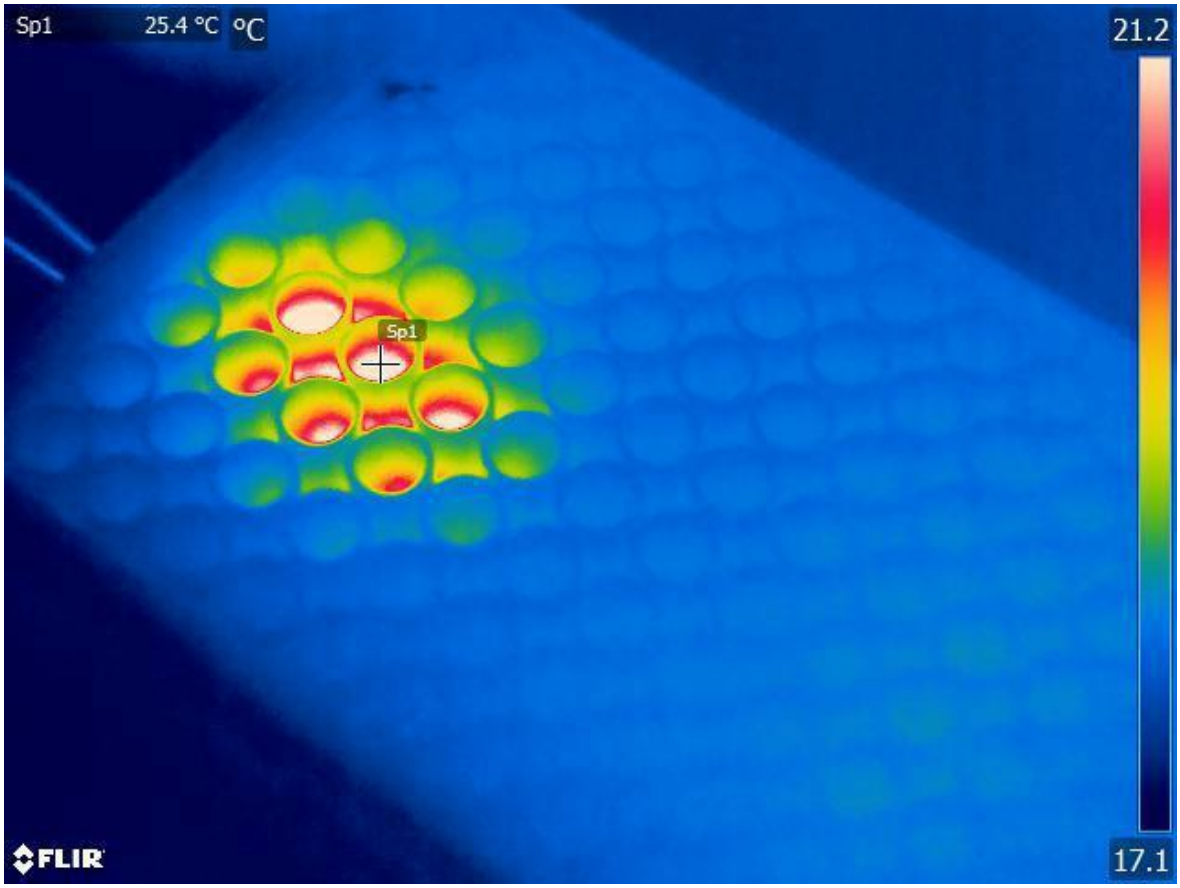

Figure 7.1 SAW temperature distribution over a 96 well cell culture plate

To combat this issue, SAW waves emitted from the device are pulsed to limit the duration. Figure 7.2 shows a duty cycle of 1 minute powered on and 4 minutes off. Having the power on for 1 minute allows the utilisation of full acoustic wave strength to stimulate the cells with 4 minutes for the wells and cell temperature to dissipate. This results in less than a degree change in temperature, allowing the cells to be in normal growth conditions.

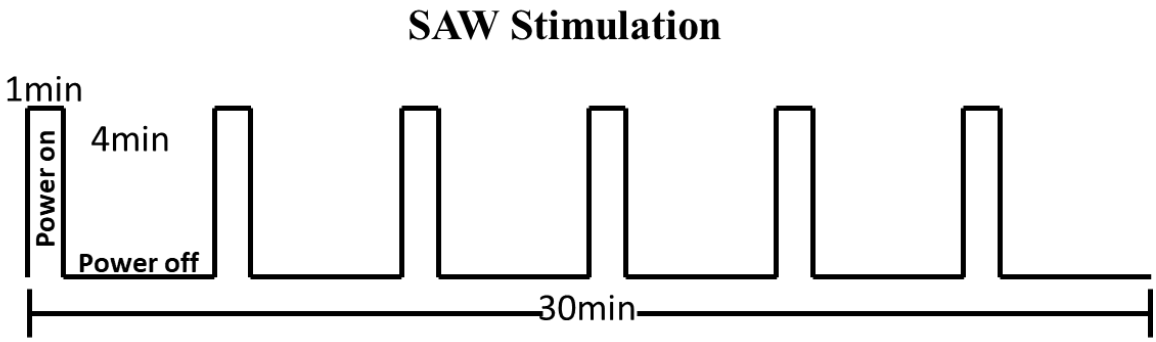

Figure 7.2 SAW duty cycle

Table 7.2 lists the timetable for cell stimulation over two days. The cells were seeded just before the first stimulation, and then they are grown over two days and counted after the seconds day.

Table 7.2 Example timetable for two days of saw stimulation

	Day 1 Stimulation										
	07:00	08:00	09:00	10:00	11:00	12:00	13:00	14:00	15:00	16:00	17:00
Sample 8											
Sample 9											
Sample 10											

	Day 2 Stimulation										
	07:00	08:00	09:00	10:00	11:00	12:00	13:00	14:00	15:00	16:00	17:00
Sample 8											
Sample 9											
Sample 10											

7.3. Cell growth actuation

7.3.1 Cell growth with 1000 cells seeded per well

The first two samples had the signal generator set to 5 V. Whereas sample 1 had 3 stimulations per day and sample 2 had 2 stimulations per day with approximately 1000 cells

initially per well. In this instance that cells were fixed and stained. Figure 7.3 shows the cells grown using the sample 1.

Figure 7.3 (a) shows the layout of cells grown above the SAW device. B2 is the well behind the IDT but above the electrode pads, where the wires are bonded to the device. This is in line with the wave propagation path in the reverse direction. C1 is the well which is at the left side of the device centre. C2 is the central well which has the strongest influence from the SAW. C3 is the well to the right of the SAW device. D2 is in front of the IDT in the propagation path of the SAW along the substrate.

Figure 7.3 (b) shows one image taken of the stained cells in well B2.

Figure 7.3 (c) is the image taken of the stained control cells that have no SAW influence.

Figure 7.3 (d) is the image taken of the stained cells in well C1

Figure 7.3 (e) is the image taken of the stained cells in well C2

Figure 7.3 (f) is the image taken of the stained cells in well C3

Figure 7.3 (g) is the image taken of the stained cells in well D2

Clearly from these images, the largest surface area of blue is in the central well directly above the IDT (Figure 7.3 (e)), where the SAW actuation is strongest. The next well with the most stained area is Figure 7.3 (g). This well is directly in front of the IDT, and it is along the propagation path of the SAW. The other wells show very similar stained areas, but they are all slightly more than the control cells in Figure 7.3 (c). Together with the losses of SAW strength along the length of the substrate, the coupling with ultrasonics gel may cause some level of attenuation. The cells grown either side or perpendicular to the SAW

propagation direction may also have experienced sideway leakage of waves through the base of the culture plate causing the stimulation of growth.

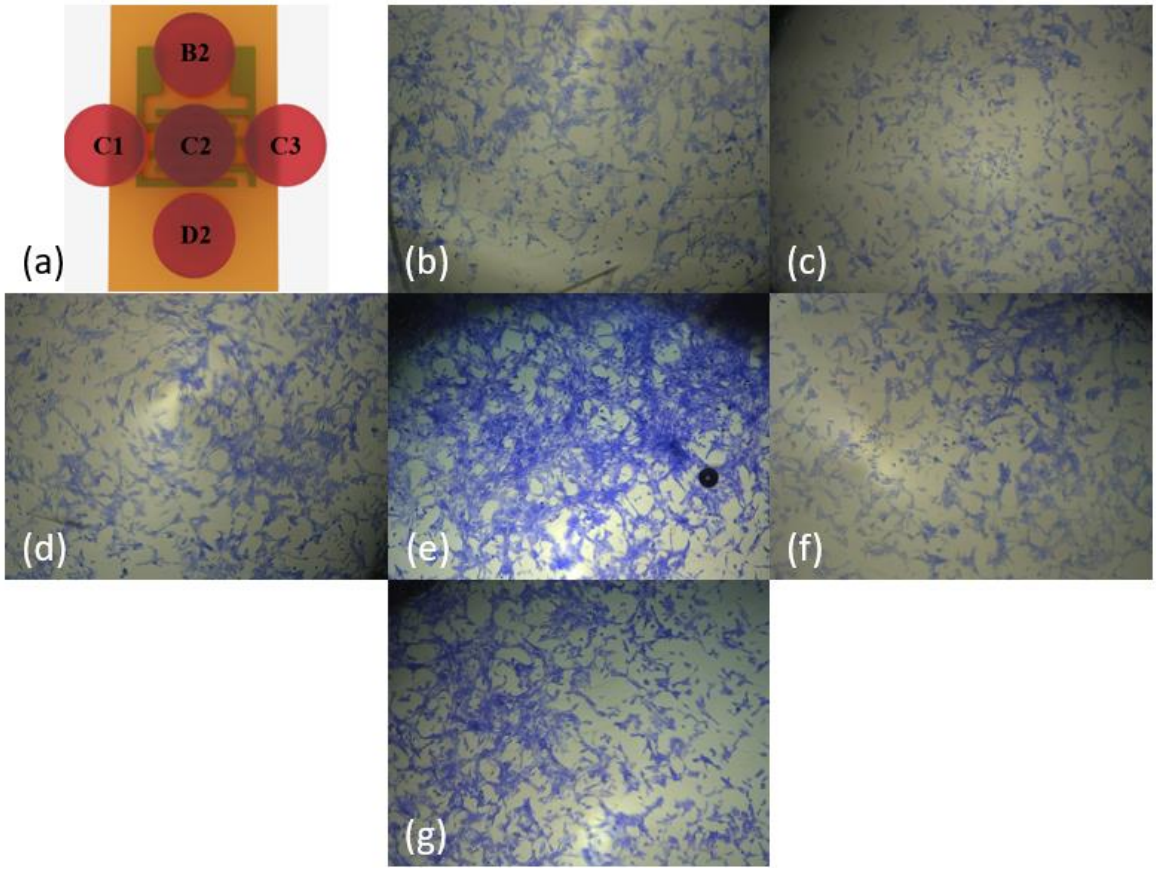

Figure 7.3 sample 1: 3 stimulations per day (a) well's location in reference to SAW device (b) well B2 behind IDT (c) Control well (d) well C1 left of IDT (e) well C2 epicentre of SAW (f) well C3 right of IDT (g) well D2 in front of IDT

Sample 2 shown in Figure 7.4 has one less stimulation than was performed in sample 1.

Figure 7.4 (a) again is a reference for the layout of cell growing above the SAW device.

Figure 7.4 (b) is the image taken of the stained cells in well B2.

Figure 7.4 (c) is the image taken of the stained control cells that have no SAW influence.

Figure 7.3 (d) is the image taken of the stained cells in well C1.

Figure 7.4 (e) is the image taken of the stained cells in well C2.

Figure 7.4 (f) is the image taken of the stained cells in well C3.

Figure 7.4 (g) is the image taken of the stained cells in well D2.

Whilst first looking at the images, there appears to be the occurrence of enhanced cell growth. This is likely due to error when seeding the initial 1000 cells in each well. Therefore, in these experiments, individual wells can only be compared with each other in the same group of samples. When comparing to the control well (Figure 7.4 (c)), there are larger areas of cells but, not as much increased compared to the increased ones shown in Figure 7.3. The differences in the outside of the centre region are also much closer in quantity of cells to the central well as shown in Figure 7.4 (e).

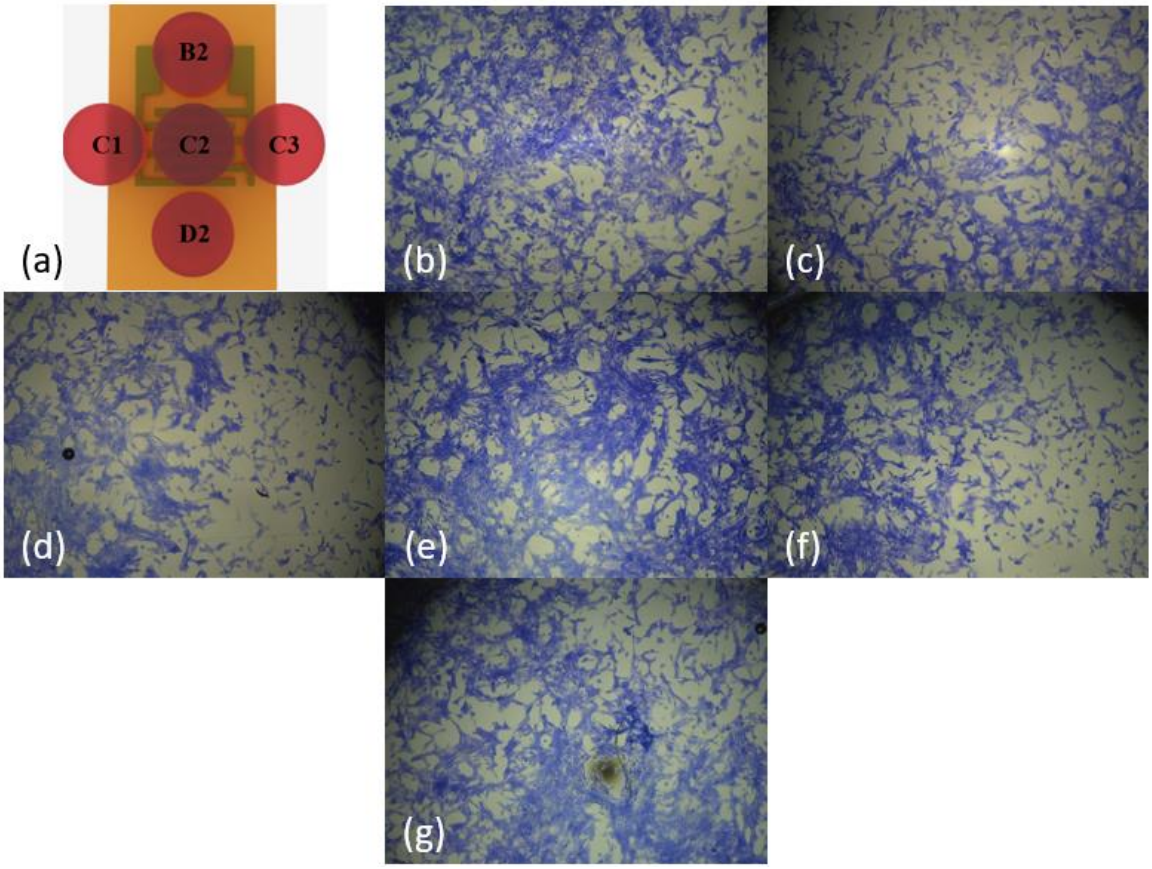

Figure 7.4 sample 2: 2 stimulations per day (a) well's location in reference to SAW device (b) well B2 behind IDT (c) Control well (d) well C1 left of IDT (e) well C2 epicentre of SAW (f) well C3 right of IDT (g) well D2 in front of IDT

7.3.2 Cell growth with 600 cells seeded per well

The next set of cell growth experiments was run with 600 cells seeded per well, as the cells grown exponentially unfortunately by the end of the proliferation duration not enough cells were grown and we could not visualise any growth. Figure 7.5 shows the results of SAW stimulation for 3 times for 30 minutes per day.

Figure 7.5 (a) is a reference for the layout of cell growing above the SAW device.

Figure 7.5 (b) is the image taken of the stained cells in well B2.

Figure 7.5 (c) is the image taken of the stained control cells that have no SAW influence.

Figure 7.5 (d) is the image taken of the stained cells in well C1.

Figure 7.5 (e) is the image taken of the stained cells in well C2.

Figure 7.5 (f) is the image taken of the stained cells in well C3.

Figure 7.5 (g) is the image taken of the stained cells in well D2.

Figure 7.5 (e) is the central well C2 where the cells receive the strongest acoustic wave interactions. With this level of cells, there are very little visual differences between the stimulated cells and the control group as shown in Figure 7.5 (c). As the cell growth is exponential, it is too early to say at this stage for a proper conclusion.

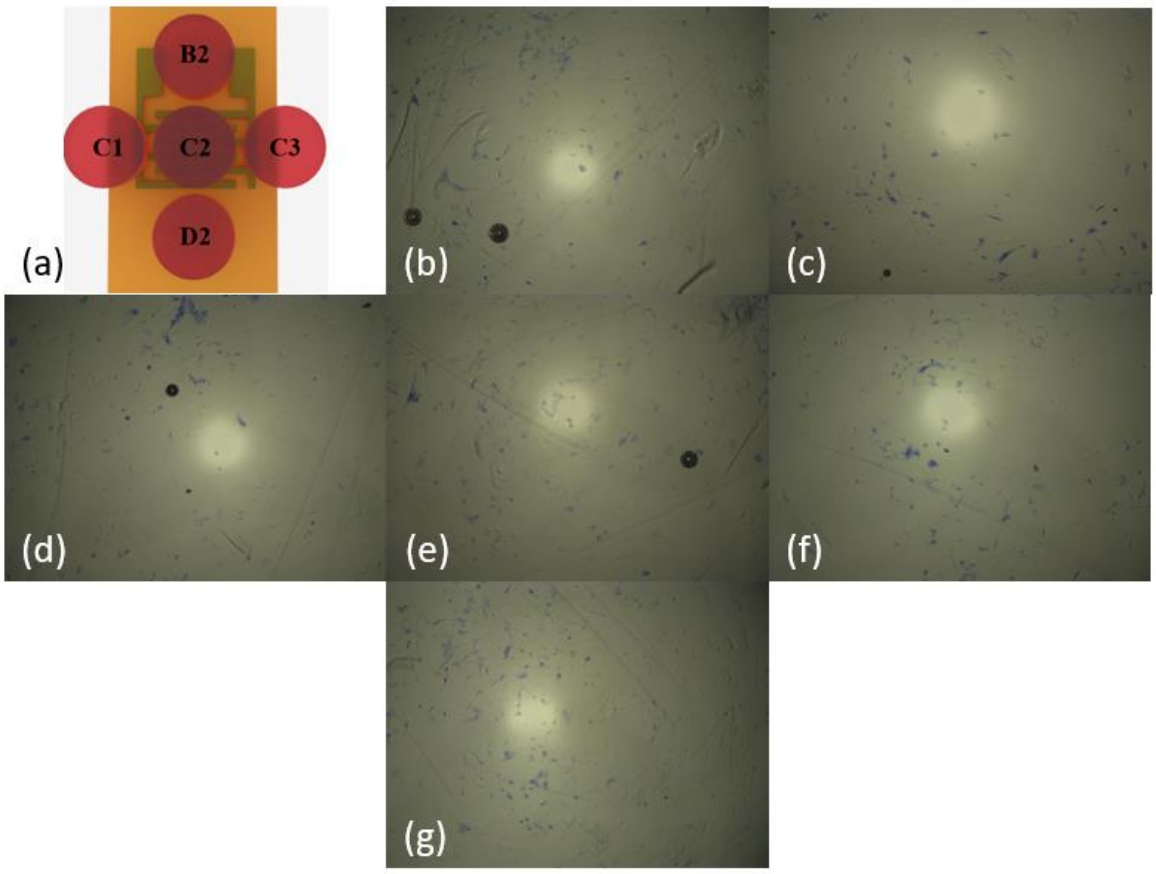

Figure 7.5 sample 3: 3 stimulations per day (a) well's location in reference to SAW device (b) well B2 behind IDT (c) Control well (d) well C1 left of IDT (e) well C2 epicentre of SAW (f) well C3 right of IDT (g) well D2 in front of IDT

Figure 7.6 represents stimulation of 2 time for over 2 days.

Figure 7.6 (a) is a reference for the layout of cell growing above the SAW device.

Figure 7.6 (b) is the image taken of the stained cells in well B2.

Figure 7.6 (c) is the image taken of the stained control cells that have no SAW influence.

Figure 7.6 (d) is the image taken of the stained cells in well C1.

Figure 7.6 (e) is the image taken of the stained cells in well C2.

Figure 7.6 (f) is the image taken of the stained cells in well C3.

Figure 7.6 (g) is the image taken of the stained cells in well D2.

Again, there are very few cells after the SAW stimulation, but they are slightly more visible when compared to those in Figure 7.5. This is likely attributed to the approximate numbers of cells seeded being slightly higher when compared to those in Figure 7.5. Although difficult to distinguish, there appear to be a slightly larger area of stained cells as shown in Figure 7.6 (e) than those in Figure 7.6 (c). This indicates that at this stage during the cell proliferation, the SAW stimulation may be starting to take effect.

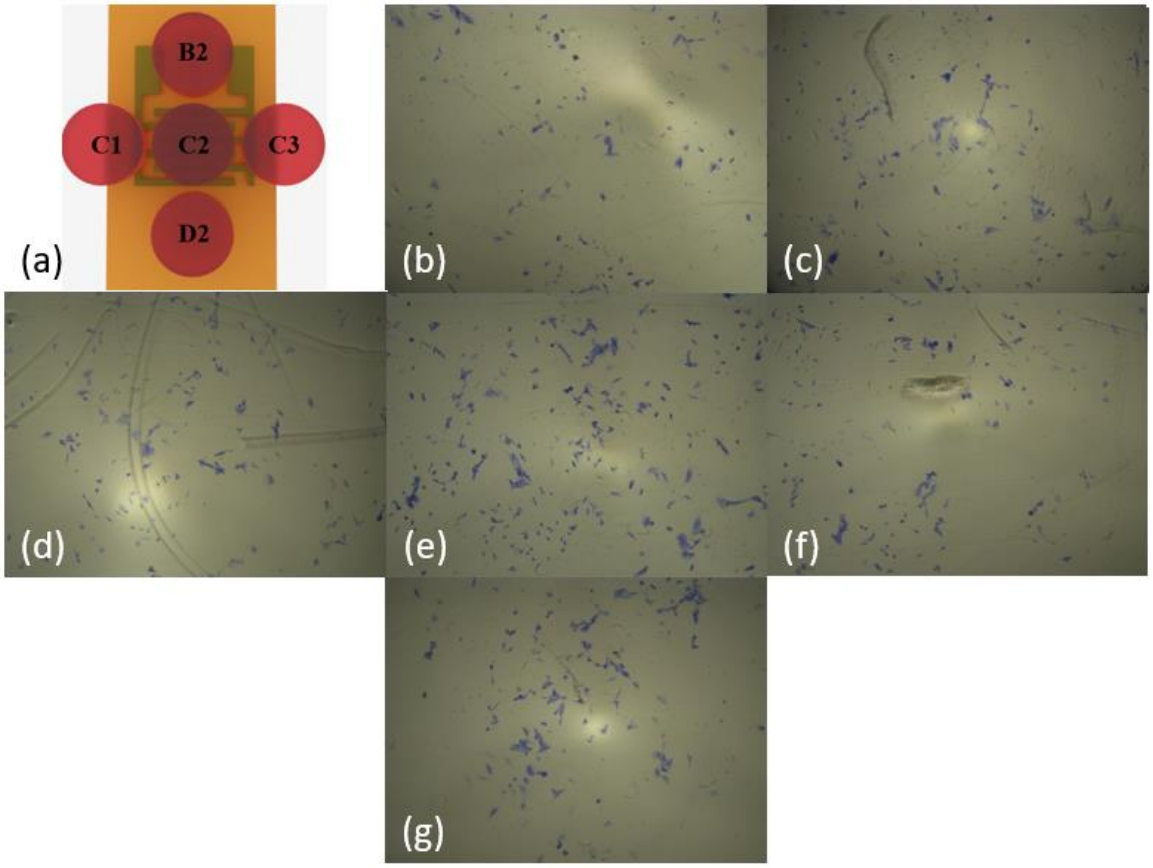

Figure 7.6 sample 4: 2 stimulations per day (a) well's location in reference to SAW device (b) well B2 behind IDT (c) Control well (d) well C1 left of IDT (e) well C2 epicentre of SAW (f) well C3 right of IDT (g) well D2 in front of IDT

7.3.3 Cell counting using hemocytometer

In the next set of experiments, I used a hemocytometer to count the cells. During these experiments, the cell count was performed using a hemocytometer shown in Figure 7.7. Figure 7.7 (a) shows that the cells are spread throughout the quadrant, and 4 of these sections are counted to estimate the number of cells in the well where it was extracted from. Figure 7.7 (b) shows that when the cell population is overly dense, they are harder to count. As the cells are more likely to group up, a higher dilution factor should be used. There are a higher number of alive and dead cells. The dead cells are stained blue as the dye penetrates the cell walls once they have died. Figure 7.7 (c) shows a high proportion of dead cells, possibly due to over stimulation by the SAW.

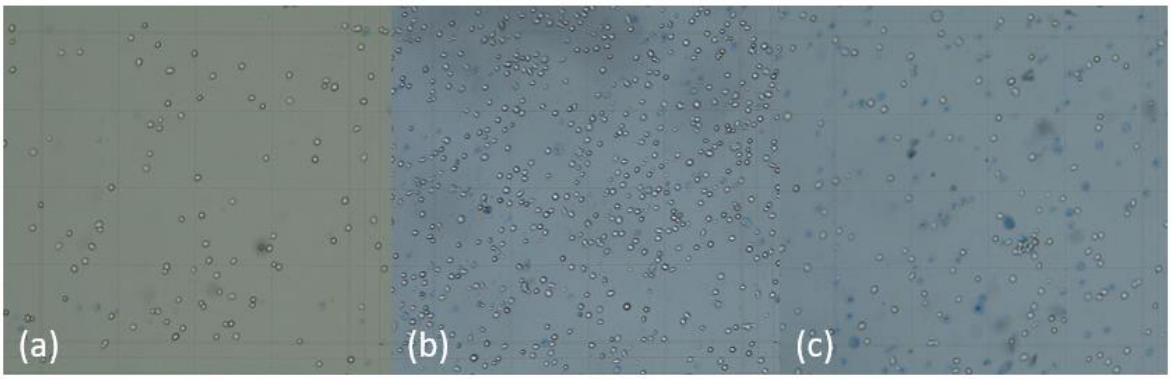

Figure 7.7 Cells in one quadrant of the Hemocytometer (a) Cells spread througout (b) highly populated cell count (c) high amount of dead cells

7.3.4 Cell stimulation at higher voltages

The next 3 experiments were set to change the voltage applied of 10 Vpp, a higher voltage using an amplifier (up to 24 Vpp) and 4 stimulations per day at 10 Vpp. Table 7.3 summarises the counting results of each well used on the 96 well plate for sample 8 shown in Figure 7.8. A portion of cell solutions were extracted from each well and placed in the hemocytometer. The quadrants of the hemocytometer were labelled as A, B C and D. The number of alive and dead cells were counted in each quadrant. This was proportional to the total amount in each well. Wells B2, C1, C2, C3, D2 and E2 were stimulated by the SAW device. These wells had the same arrangement as previous experiments shown in Figure 7.3 to Figure 7.6 with the addition of E2. E2 was on the edge of the substrate in front of C2 in the propagation path of the acoustic wave. This well was the furthest away from the SAW device in the propagation path.

Table 7.3 Sample 8 Cell count of results with a SAW source of 10Vpp

Sample8	A		B		C		D	
	Alive	Dead	Alive	Dead	Alive	Dead	Alive	Dead
B2	172	68	103	22	123	52	215	60
C1	138	16	93	14	141	27	91	9
C2	148	21	32	10	52	13	25	10
C3	176	13	178	15	102	5	186	15
D2	73	10	59	8	127	14	98	7
E2	80	7	109	6	84	3	44	6
B12	98	74	113	73	125	40	67	55
C12	139	49	88	26	166	43	122	35
D12	184	49	194	34	173	47	151	34
E12	191	16	143	16	173	9	171	14
F12	163	8	196	8	192	75	189	199
G12	114	72	119	101	98	145	96	91

The cell proliferation is best evaluated as a percentage increase using the SAW when compared to that of the control samples. The increase in voltage appeared to be too high for the cells to proliferate effectively. Although the acoustic wave energy had the most interactions with the cells, unfortunately the lowest number of cells were observed as shown in Figure 7.8. The well B2 had 106 % increase when compared to the unstimulated well, but it also had the highest number of dead cells. The best outcome was from the well C3 as this showed an increase of 11 % more cells than the control group, and also had ~78 % less dead cells. Due to the design of the SAW device, the IDT location was towards the back of the device. In this case, the majority of the contact area on the substrate was in front. Those behind, left and right of the central stimulation point were only partially coupled with the SAW device, likely causing greater attenuation. This showed that the voltage was in fact too high in the cases we studied, and a lower value was more affective. The left and right wells, e.g., C3 and C1, have shown further attenuation due to the wave propagation direction.

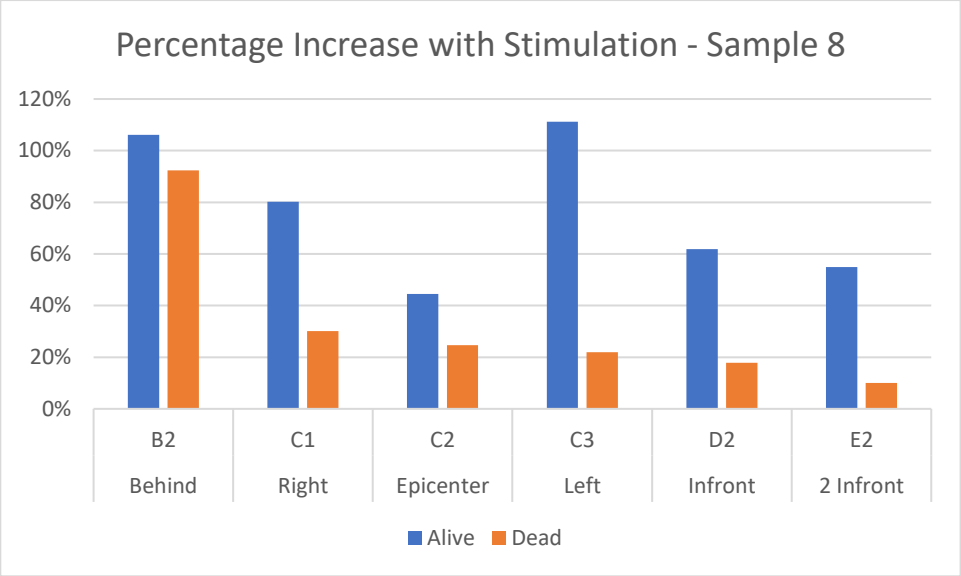

Figure 7.8 SAW stimulation results with a SAW source of 10Vpp

During the same test, a sample was also applied with 24 Vpp. Based on the knowledge of 10 Vpp this was far too much, and the results in Figure 7.9 show a very high ratio of dead cells. As with the previous sample shown in Figure 7.8, behind (e.g., well B2), left and right (wells C3 and C1) were the only samples to have shown increases in the number of living cells, with the left of the IDT being the highest increase again.

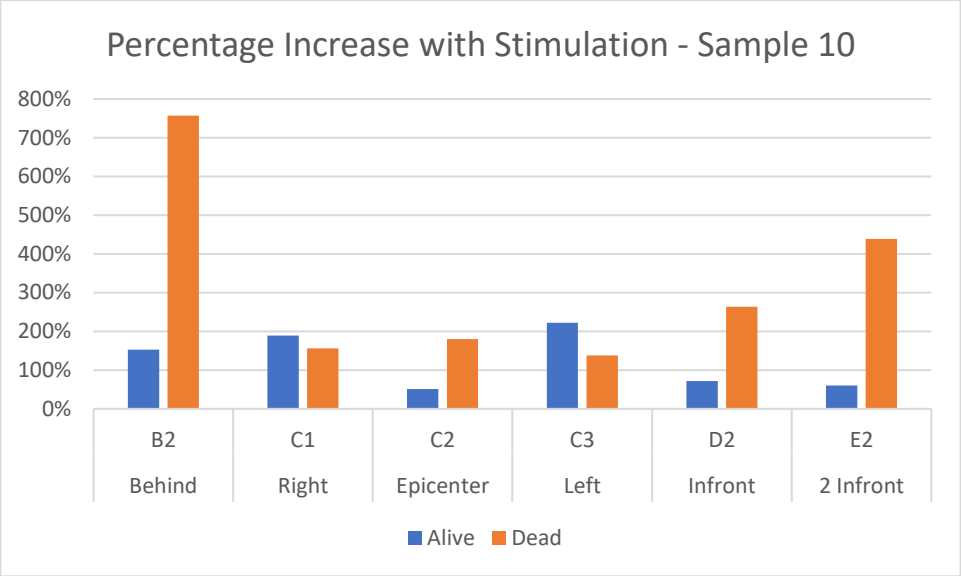

Figure 7.9 SAW stimulation with 24Vpp

Previously we found that 3 stimulations per day revealed a better proliferation when compared to 2 stimulations per day. In the experiment shown in Figure 7.10, we attempted 4 stimulations to compare with the previous two samples. This sample has four evenly spaced stimulations each day and is applied with 10 Vpp in the same way as Figure 7.8. The results again highlight the wells C1 and C3 being consistent among the higher percentage increases. In this sample, the wells in front (e.g., wells D2 and E2) have achieved around 100 %, meaning that they have very little or no increase compared with the unstimulated or control group of cells. Cells grown directly above the IDT (i.e., well C2) and behind (i.e., well B2) yet again show high ratios of dead cells, likely killed due to too much acoustic energy interactions.

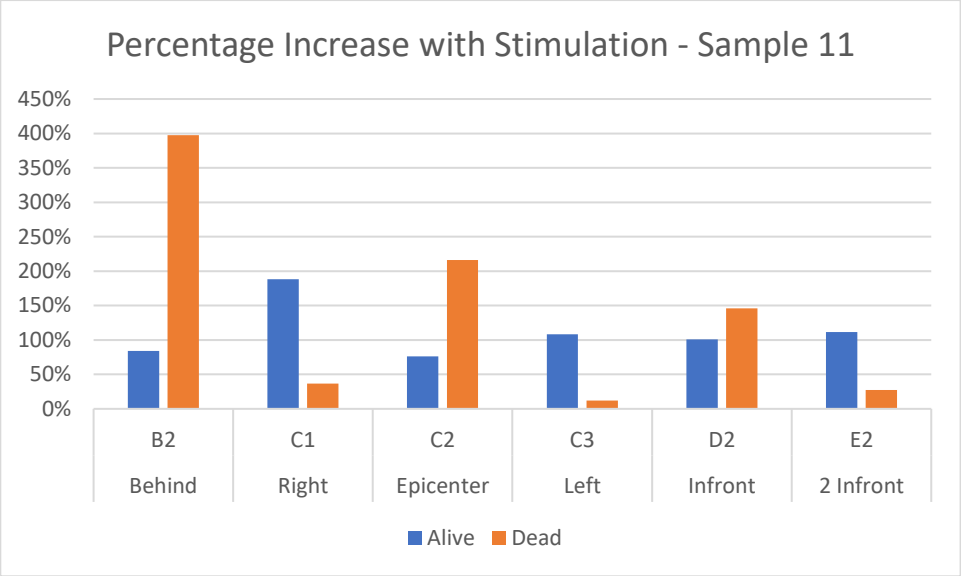

Figure 7.10 SAW with 4 stimulations per day

7.3.5 Cell stimulation with reduced SAW duty cycle

The next two experiments are performed with the knowledge of the power being too high to activate the cells. The first test reduces the duration of the SAW signal being active, by changing the pulse signal to 30 seconds on and 4.5 minutes off as shown in Figure 7.11.

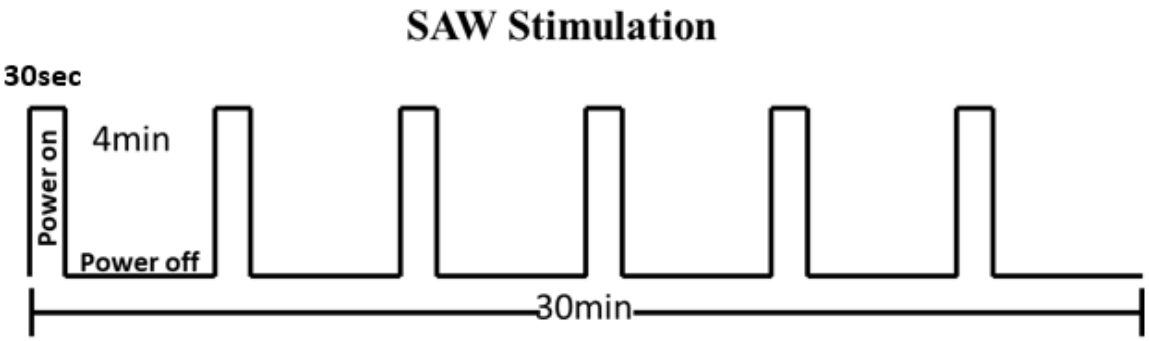

Figure 7.11 SAW half duty cycle

Once the sample growth period had ended, the cells were fixed and stained in the wells, instead of taking out for the hemocytometer. They were then transported to a microscope, then photos were taken, and cells were counted. This method did not reveal dead and alive cells, but showed cells in the state they were at the end of the stimulations. Figure 7.12 clearly shows the cells are adhered to the surface with their elongated morphologies. Any cells that are circular could either be dead or in the stages of splitting into two and re-adhering to the substrate.

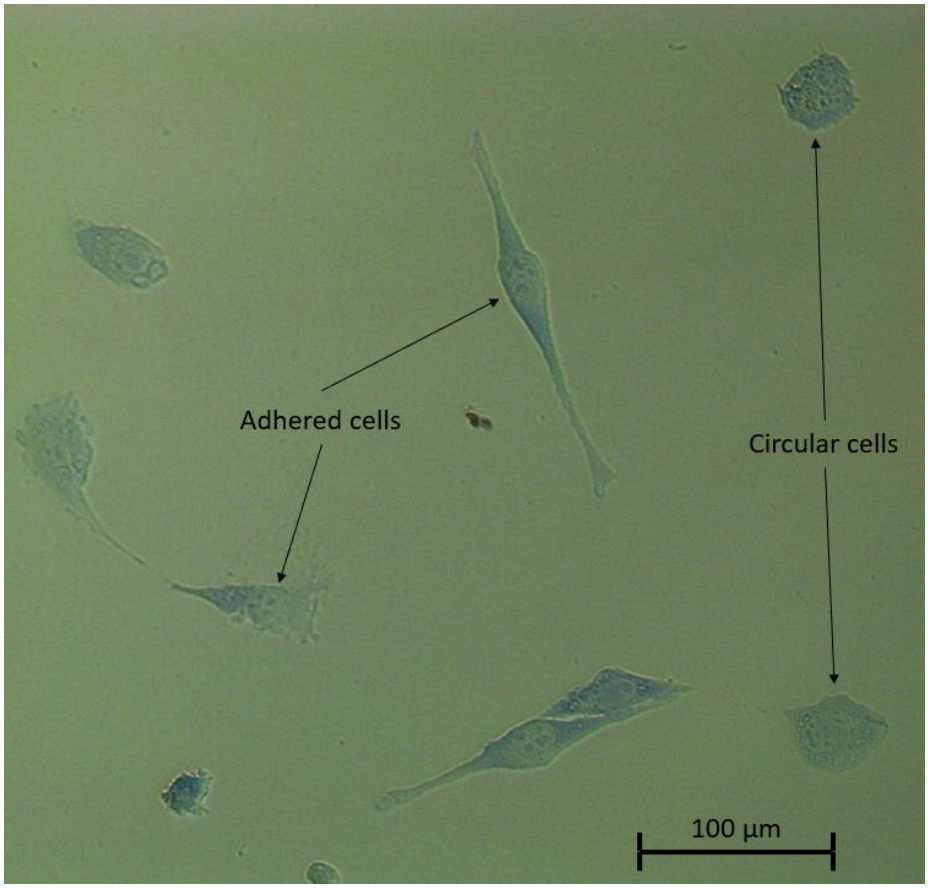

Figure 7.12 Microscope image of cells fixed in 96 wells

Figure 7.13 shows an increase in cell proliferation in all wells. Focusing specifically on the non-circular cells, we can see that there is an increase of 85 to 114% compared to the non-

stimulated ones. In this case in front of the IDT (i.e., the well E5) has the highest numbers of both cell shapes. The percentage increase is quite comparable to that at 5 Vpp shown in Figure 7.3, where the area of blue looks to cover a much higher percentage of the well. This could be due to the change of duration of the signal applied to the SAW device, which has been halved, i.e., the average power is halved applied to the cells.

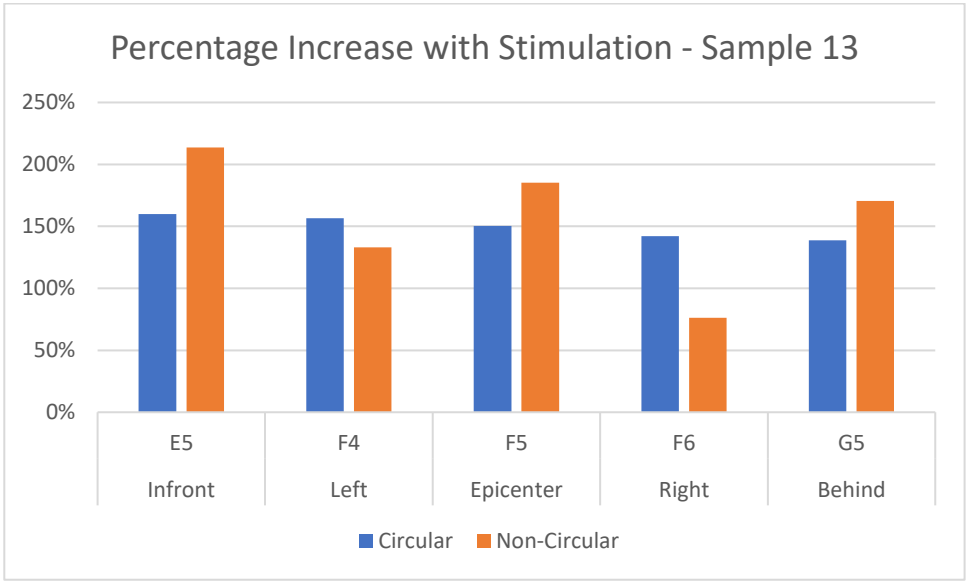

Figure 7.13 SAW with half duty cycle

7.3.6 Cell stimulation with various voltages

The next test was using the standard 3 stimulations per day but with 8 Vpp. The obtained results are shown in Figure 7.14. The wells have similar quantities of circular cells when compared with those shown in Figure 7.13. However, the amount of non-circular cells were significantly lower. This may indicate that 8 Vpp was still too high. It may increase the overall cell counts but could also kill more cells in the process.

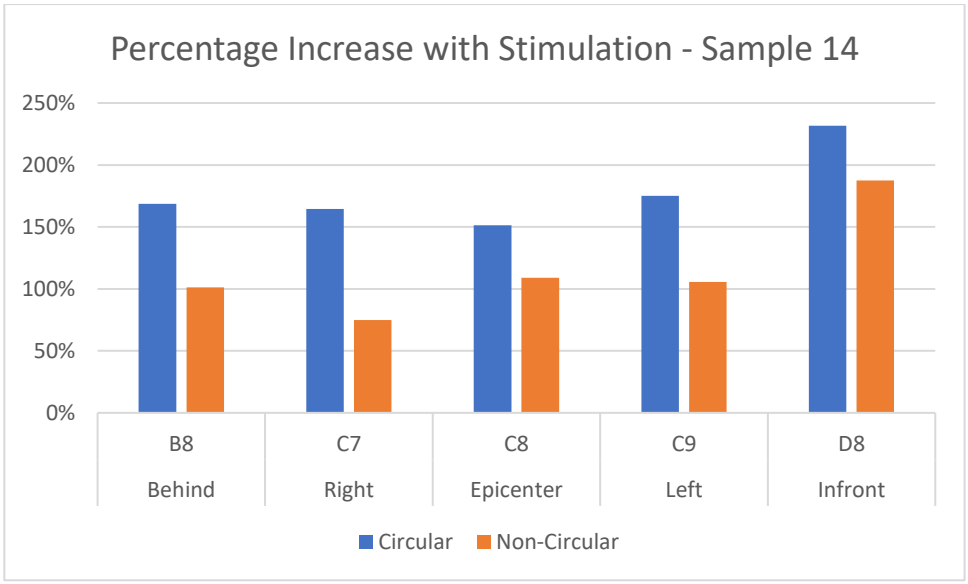

Figure 7.14 SAW with 8Vpp

After noticing that 10 Vpp and 24 Vpp are too high, a range of voltages were then applied to study the effect of the mechanical wave intensity on the cell proliferation. Figure 7.15 shows the results obtained by varying the voltage applied to the cells. Whilst all the voltages including 10 Vpp improved the proliferation, 7 Vpp shows an unusually high increase. This is most likely due to the seeding errors, therefore, further testing at 7 Vpp should be explored in future. Results of the majority of voltages show an increase of proliferation between 20 % and 100 %.

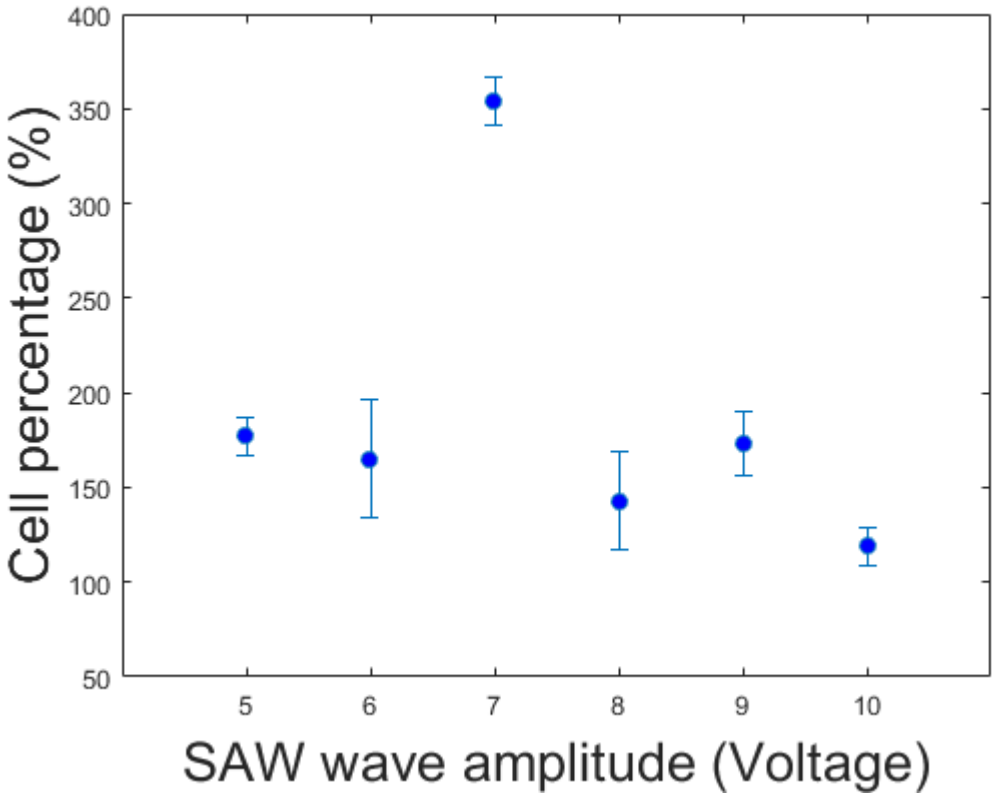

Figure 7.15 SAW excitation with increasing voltage applied

7.3.7 Stimulation of Normal Human Dermal Fibroblasts

All the above results show that SAW can increase the cell growth rate. In order to demonstrate that the thin film SAW system can be used for varied types of cells, I chose human dermal fibroblasts to be grown on a glass cover slip. This was performed on a different SAW device which cannot be fitted under the 90 well plate. Other frequencies were also explored to investigate the frequency effects.

Figure 7.16 shows that various SAW devices are used, which are 14 MHz, 9.5 MHz and 25 MHz. These devices are used in the cell growths with SAW stimulation using the same routine as before, e.g., 3 sets of stimulation per day. They were tested at 3, 5 and 7 Vpp,

respectively. There was too much attenuation through the 96 well plate when the voltage of 3 Vpp or lower is used. The new method I have used is a glass slide on the SAW device in front of the IDT, bonded with the ultrasound gel. This method along with the plate SAW devices allows the easy SAW propagation into the cell solutions. As shown in Figure 7.16, The increase in cell growth was observed with the increase of voltage, which is similar with the results from the myoblast cells as shown in Figure 7.15, with the exception of the second 14 MHz device.

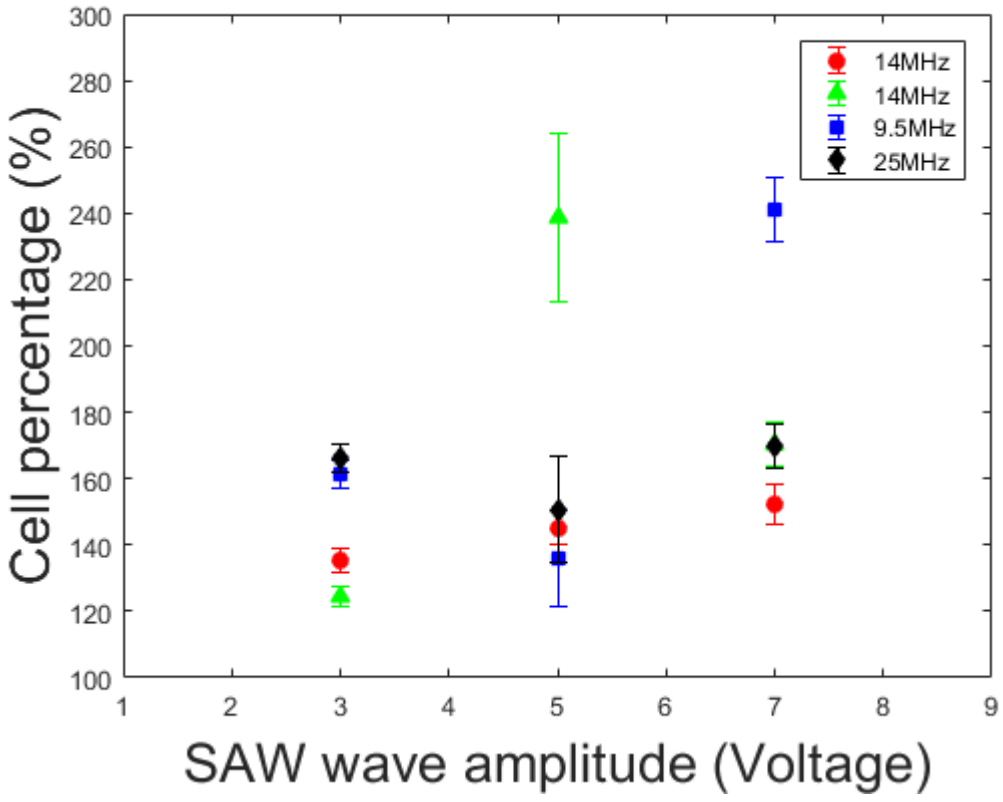

Figure 7.16 SAW excitation of Fibroblasts

7.4. Discussions on Cell growth and monitoring

During studying the effects of SAW stimulation of cells, the Raspberry Pi was used to control the time of stimulations, from the duty cycle to the schedule of the stimulations each day. The platform reduces the number of hours required by the operator to control the stimulations. This shows a great potential for an automated cell care system for the growth with controlled increased proliferation. Alongside the cell stimulation, SAW has been proven in droplet actuation and position control as reported in Chapter 4. The liquid movement could be employed in moving components such as fresh liquid medium used to feed the cells and other liquids such as PBS which is used to wash the cells. In addition to droplet control, the high quality camera of Raspberry Pi could be used along with objective lenses to monitor the cells and their growth. Using image filtering with the OpenCV library, as well as the blob detection, the number of cells can be easily counted. Figure 7.17 (a) shows the original microscope image of cells. Figure 7.17 (b) shows the image after filtering which only shows the cells. Figure 7.17 (c) shows that the blob detection is used to count the number of cells. Combining the idea using a transparent glass based SAW device, the potential for live monitoring of cell adhered to the surface is very promising in cell biology applications [206][207].

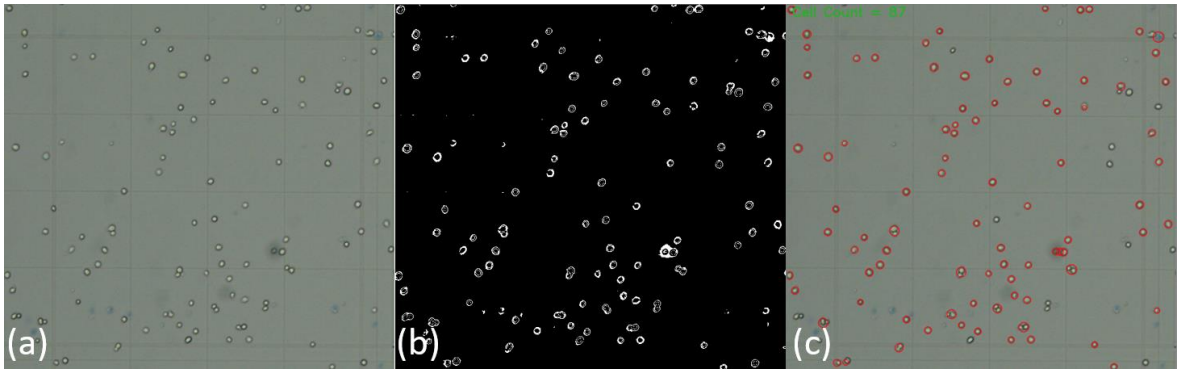

Figure 7.17 using Raspberry Pi to count cells (a) microscope image of cells (b) filtered image of cells (c) using blob detection to count cells

7.5. Summary

In this chapter, the effects of SAW on cell culture have been explored. SAW has been proven to increase cell proliferation of C2C12 cells by 20 % up to 100% depending on the wave amplitude. It has also been shown that too much energy input into the cells can have the reverse effect killing a large portion of cells. Potential contributing factors are the wave propagation through the base of the culture plate and the streaming induced into the medium covering the cells.

Human skin cells were also investigated. They had the same testing routine and procedures but using aluminium plate SAW devices with a PDMS chamber on a glass slide to contain the cells. These cells revealed a similar increase of between 20 % and 140 % of cells when compared to those unstimulated cell samples. This has shown a great potential for being used along with flexible devices for helping with human muscle growth and tissue repair [208][209][210][211].

Combining this work with the Raspberry Pi platform, there is a huge potential for an automated cell care system. This could reduce the hours required to maintain cells and reduce the change for cell contamination. This could be done by manipulating the liquids used in the cell culture, from the moving of medium to supply nutrients to cells, to mixing on PBS on the cells to wash away the old medium.

Chapter 8. Conclusion

8.1. Conclusions

SAW devices using thin film techniques are increasingly used in lab-on-a-chip and biomedical applications, however, there are some issues about the need for expert operators and bulky complicated benchtop lab equipment. To solve these issues, this thesis presents a modular platform that was developed with open source electronics utilising surface acoustic wave devices. This platform is able to utilise both the sensing and actuation functions autonomously in a range of biomedical applications, reducing the requirement of an operator and bringing down the cost of the overall system. Raspberry pi is the foundation for this platform, it is small scale, low cost, with ease of use and an open source nature. Combining Raspberry Pi with Python allows the system to be easily integrated with a range of lab equipment and sensors to manipulate SAW devices.

The first application of the modular system was digital acoustofluidics, we applied the SAW Raspberry Pi platform combined with Python and showed the ability to perform a number of acoustofluidic functions. We demonstrated successfully moving droplets across a substrate to a target position using PID controller and camera tracking in a feedback loop. These droplets can be varied in size, varied in liquid properties and even successfully moved on inclined, deformed, or sloped substrate. The results showed that even without optimal PID tuning, the droplet was able to be transported across the surface without significant changes in velocity in the event of a non-uniformly treated surface. The platform also moved a droplet on an XY plane by the implementation of multiple PID controllers running in parallel on separate axis. Controlling the droplet position by touchscreen further showed the

potential to handle biomedical or hazardous samples whilst reducing human contact preventing contamination or injury.

The next application built upon droplet manipulation, introducing temperature control and fluorescence measurements for in-field diagnostics. The thermal camera was used and allowed for temperature control in a similar manner to droplet movement. Another PID controller was implemented, which was able to adjust the power until a target temperature was met and maintained. The SAW devices were capable of heating small sample sizes to meet the requirements for LAMP and PCR with a high degree of accuracy, whereas typical thermal cyclers have thermal blocks with slots to place reaction vials. The thermal imaging camera was also used to monitor the SAW device itself, automatically adjusting the frequency output leading to more efficient use of the acoustic device. This technique combines the stages of sample preparation and thermal cycling into an automated process that has the potential to be scaled up with low sample volumes needed.

The thin film SAW platform has been demonstrated for the application of breath detection and monitoring. A combined humidity and temperature sensor was integrated and used to monitor ambient changes or compared with the SAW device response. A vector network analyser was controlled via the Raspberry Pi recording the frequency response. The effects of breath are shown to be largely caused by humidity, but temperature will also influence the SAW signal. The platform has the potential to filter the environmental effects such as temperature and then automatically calculate the respiration rate of the patient in a non-invasive way.

Finally, the platform was used in SAW stimulation of biological cells. A Raspberry Pi was used to control a signal generator and multiplex board to stimulate cells at specific intervals over multiple days. SAW has been proven to increase cell proliferation of C2C12 cells by 20 % up to 100% depending on the wave amplitude, and a similar increase of between 20 % and 140 % for the NHDF cells. Factors contributing to the cell growth include the wave propagation through the base of the culture plate and the streaming induced into the medium covering the cells.

8.2. Future work

The following future work has been proposed.

Further hardware alterations could be made further improving the platform:

- Replacing a signal generator with a direct digital synthesis module to generate the sinusoidal wave forms or using a square wave direct from the Raspberry Pi.
- Experimenting with Raspberry Pi alternatives that may offer better performance for machine learning and computer vision.
- Improve platform portability and adding more wireless functionality
- Replacing the network analyser with dedicated frequency counting circuitry or adapting a software defined radio into a spectrum analyser
- Preparing the platform and performing full PCR and LAMP assays with real samples

Software improvements for the platform:

- Training or machine learning for pid tuning and surface profiling to improve droplet transportation

- Additional PID controllers could be implemented, one for each IDT
- The code could be redone in C programming gaining large performance increases
- The temperature difference between the surface and the droplet opens up the possibility to control temperature without the need for a thermal imaging camera. Using the surface temperature or even the frequency shift and the TCF
- The Addition machine learning may be beneficial for breath tracking, helping identify breathing disorders. These could use existing medical data for detecting breathing disorders.

Further development of SAW devices:

- Experiment with different IDT type and patterns
- Software simulation of SAW sensor and acoustofluidics performance using the software such as COMSOL.
- Assess the ability to use SAW device deposited on metal core PCBs
- An alternative method to hold droplet position could be engaging multiple IDT from different directions to stabilise the droplet's position.
- Test with higher frequency devices with better sensitivity and suited to sensing humidity
- Design and testing of wireless SAW for breath monitoring
- Incorporate SAW device into breathing mask, test flexible devices for breathing
- Investigate more SAW parameters and their effect on cells for wound healing
- Develop cell culture system with cell counting and transparent SAW devices
- Investigate the integration of thin film temperature sensors on the same substrate

References

[1] Y. Q. Fu *et al.*, "Recent developments on ZnO films for acoustic wave based bio-sensing and microfluidic applications: a review," *Sensors and Actuators, B: Chemical*, vol. 143, no. 2, pp. 606–619, 2010, doi: 10.1016/j.snb.2009.10.010.

[2] M. Kim, Y. S. Wu, E. C. Kan, and J. Fan, "Breathable and flexible piezoelectric ZnO@PVDF fibrous nanogenerator for wearable applications," *Polymers (Basel)*, vol. 10, no. 7, Jul. 2018, doi: 10.3390/POLYM10070745.

[3] G. (Gustav) Gautschi, *Piezoelectric sensorics : force, strain, pressure, acceleration and acoustic emission sensors, materials and amplifiers*. Springer, 2002.

[4] S. J. Rupitsch, *Piezoelectric Sensors and Actuators*. 2019. doi: 10.1007/978-3-662-57534-5_1.

[5] Y. Liu *et al.*, "Flexible and bendable acoustofluidics based on ZnO film coated aluminium foil," *Sensors and Actuators, B: Chemical*, vol. 221, pp. 230–235, 2015, doi: 10.1016/j.snb.2015.06.083.

[6] G. Destgeer and H. J. Sung, "Recent advances in microfluidic actuation and micro-object manipulation via surface acoustic waves," *Lab on a Chip*, vol. 15, no. 13, pp. 2722–2738, Jun. 2015, doi: 10.1039/c5lc00265f.

[7] A. Barani *et al.*, "Microfluidic integrated acoustic waving for manipulation of cells and molecules," *Biosensors and Bioelectronics*, vol. 85, pp. 714–725, Nov. 2016, doi: 10.1016/j.bios.2016.05.059.

[8] G. L. Cote, R. M. Lec, and M. V. Pishko, “Emerging biomedical sensing technologies and their applications,” *IEEE Sensors Journal*, vol. 3, no. 3, pp. 251–266, Jun. 2003, doi: 10.1109/JSEN.2003.814656.

[9] J. Friend and L. Y. Yeo, “Microscale acoustofluidics: Microfluidics driven via acoustics and ultrasonics,” *Reviews of Modern Physics*, vol. 83, no. 2, pp. 647–704, Jun. 2011, doi: 10.1103/RevModPhys.83.647.

[10] L. Y. Yeo and J. R. Friend, “Ultrafast microfluidics using surface acoustic waves.,” *Biomicrofluidics*, vol. 3, no. 1, p. 12002, Jan. 2009, doi: 10.1063/1.3056040.

[11] L. Y. Yeo and J. R. Friend, “Surface Acoustic Wave Microfluidics,” *Annual Review of Fluid Mechanics*, vol. 46, no. 1, pp. 379–406, Jan. 2014, doi: 10.1146/annurev-fluid-010313-141418.

[12] Y. Q. Fu *et al.*, “Advances in piezoelectric thin films for acoustic biosensors, acoustofluidics and lab-on-chip applications,” *Progress in Materials Science*, vol. 89, pp. 31–91, 2017, doi: 10.1016/j.pmatsci.2017.04.006.

[13] A. Manbachi and R. S. C. Cobbold, “Development and Application of Piezoelectric Materials for Ultrasound Generation and Detection:,” *http://dx.doi.org/10.1258/ult.2011.011027*, vol. 19, no. 4, pp. 187–196, Nov. 2011, doi: 10.1258/ULT.2011.011027.

[14] J. Jacob, N. More, K. Kalia, and G. Kapusetti, “Piezoelectric smart biomaterials for bone and cartilage tissue engineering,” *Inflammation and Regeneration*, vol. 38, no. 1. BioMed Central Ltd., Feb. 27, 2018. doi: 10.1186/s41232-018-0059-8.

[15] C. Halperin *et al.*, “Piezoelectric effect in human bones studied in nanometer scale,” *Nano Letters*, vol. 4, no. 7, pp. 1253–1256, Jul. 2004, doi: 10.1021/nl049453i.

[16] A. Carter, K. Popowski, K. Cheng, A. Greenbaum, F. S. Ligler, and A. Moatti, "Enhancement of Bone Regeneration through the Converse Piezoelectric Effect, A Novel Approach for Applying Mechanical Stimulation," *Bioelectricity*, vol. 3, no. 4. Mary Ann Liebert Inc., pp. 255–271, Dec. 01, 2021. doi: 10.1089/bioe.2021.0019.

[17] Ü. Ozgur, D. Hofstetter, and H. Morkoç, "ZnO devices and applications: A review of current status and future prospects," *Proceedings of the IEEE*, vol. 98, no. 7, pp. 1255–1268, 2010, doi: 10.1109/JPROC.2010.2044550.

[18] R. Tao *et al.*, "Thin film flexible/bendable acoustic wave devices: Evolution, hybridization and decoupling of multiple acoustic wave modes," *Surface and Coatings Technology*, vol. 357, pp. 587–594, Jan. 2019, doi: 10.1016/J.SURFCOAT.2018.10.042.

[19] L. Zhang, Z. Tian, H. Bachman, P. Zhang, and T. J. Huang, "A Cell-Phone-Based Acoustofluidic Platform for Quantitative Point-of-Care Testing," *ACS Nano*, vol. 14, no. 3, pp. 3159–3169, 2020, doi: 10.1021/acsnano.9b08349.

[20] S. P. Zhang *et al.*, "Digital acoustofluidics enables contactless and programmable liquid handling," *Nature Communications*, vol. 9, no. 1, pp. 1–11, Dec. 2018, doi: 10.1038/s41467-018-05297-z.

[21] T. D. Nguyen, Y. Q. Fu, V. T. Tran, A. Gautam, S. Pudasaini, and H. Du, "Acoustofluidic closed-loop control of microparticles and cells using standing surface acoustic waves," *Sensors and Actuators B: Chemical*, vol. 318, p. 128143, Sep. 2020, doi: 10.1016/J.SNB.2020.128143.

[22] J. Matouš, A. Kollarčík, M. Gurtner, T. Michálek, and Z. Hurák, “Optimization-based Feedback Manipulation Through an Array of Ultrasonic Transducers,” 2019, [Online]. Available: http://arxiv.org/abs/1902.01328

[23] S. Alzuaga *et al.*, “A large scale X-Y positioning and localisation system of liquid droplet using SAW on LiNbO/sub 3/,” *IEEE Symposium on Ultrasonics, 2003*, vol. 2, no. c, pp. 1790–1793, 2004, doi: 10.1109/ultsym.2003.1293260.

[24] “What is a Raspberry Pi?” https://www.raspberrypi.org/help/what- is-a-raspberry-pi/ (accessed Nov. 22, 2021).

[25] V. A. Coleman and C. Jagadish, “Basic Properties and Applications of ZnO,” *Zinc Oxide Bulk, Thin Films and Nanostructures*, pp. 1–20, Jan. 2006, doi: 10.1016/B978-008044722-3/50001-4.

[26] Y. Liu *et al.*, “Flexible and bendable acoustofluidics based on ZnO film coated aluminium foil,” *Sensors and Actuators, B: Chemical*, vol. 221, pp. 230–235, Jul. 2015, doi: 10.1016/j.snb.2015.06.083.

[27] R. Tao *et al.*, “Flexible and Integrated Sensing Platform of Acoustic Waves and Metamaterials based on Polyimide-Coated Woven Carbon Fibers,” *ACS Sens*, vol. 5, no. 8, pp. 2563–2569, 2020, doi: 10.1021/acssensors.0c00948.

[28] J. P. Lata, F. Guo, J. Guo, P.-H. Huang, J. Yang, and T. J. Huang, “Surface Acoustic Waves Grant Superior Spatial Control of Cells Embedded in Hydrogel Fibers,” *Advanced Materials*, vol. 28, no. 39, pp. 8632–8638, Oct. 2016, doi: 10.1002/adma.201602947.

[29] M. Yousefi, O. Pourmehran, M. Gorji-Bandpy, K. Inthavong, L. Yeo, and J. Tu, “CFD simulation of aerosol delivery to a human lung via surface acoustic wave

nebulization," *Biomechanics and Modeling in Mechanobiology*, vol. 16, no. 6, pp. 2035–2050, Dec. 2017, doi: 10.1007/s10237-017-0936-0.

[30] K. M. Ang, L. Y. Yeo, J. R. Friend, Y. M. Hung, and M. K. Tan, "Nozzleless spray cooling using surface acoustic waves," *Journal of Aerosol Science*, vol. 79, pp. 48–60, Jan. 2015, doi: 10.1016/j.jaerosci.2014.10.004.

[31] H. Bachman *et al.*, "Open source acoustofluidics," *Lab on a Chip*, vol. 19, no. 14, pp. 2404–2414, Jul. 2019, doi: 10.1039/c9lc00340a.

[32] S. O. R. Moheimani and A. J. Fleming, *Piezoelectric Transducers for Vibration Control and Damping*. 2006.

[33] K. M. Ok, E. O. Chi, and P. S. Halasyamani, "Bulk characterization methods for non-centrosymmetric materials: second-harmonic generation, piezoelectricity, pyroelectricity, and ferroelectricity," *Chemical Society Reviews*, vol. 35, no. 8, pp. 710–717, Jul. 2006, doi: 10.1039/B511119F.

[34] A. M. Manjón-Sanz and M. R. Dolgos, "Applications of Piezoelectrics: Old and New," *Chemistry of Materials*, vol. 30, no. 24, pp. 8718–8726, 2018, doi: 10.1021/acs.chemmater.8b03296.

[35] C. K. O'sullivan and G. G. Guilbault, "Commercial quartz crystal microbalances-theory and applications," *Biosensors & Bioelectronics*, vol. 14, pp. 663–670, 1999, Accessed: Mar. 26, 2022. [Online]. Available: www.elsevier.com

[36] W. P. Mason, "Piezoelectricity, its history and applications," *J Acoust Soc Am*, vol. 70, no. 6, p. 1561, Aug. 1998, doi: 10.1121/1.387221.

[37] H. S. Kim, Y. Li, and J. Kim, “Electro-mechanical behavior and direct piezoelectricity of cellulose electro-active paper,” *Sensors and Actuators A: Physical*, vol. 147, no. 1, pp. 304–309, Sep. 2008, doi: 10.1016/J.SNA.2008.05.003.

[38] E. Fukada, “On the Piezoelectric Effect of Silk Fibers,” *Journal of the Physical Society of Japan*, vol. 11, no. 12, pp. 1301A-1301A, Dec. 1956, doi: 10.1143/JPSJ.11.1301A.

[39] J. Joseph, S. G. Singh, and S. R. K. Vanjari, “Leveraging Innate Piezoelectricity of Ultra-Smooth Silk Thin Films for Flexible and Wearable Sensor Applications,” *IEEE Sensors Journal*, vol. 17, no. 24, pp. 8306–8313, Dec. 2017, doi: 10.1109/JSEN.2017.2766163.

[40] E. Fukada and I. Yasuda, “On the Piezoelectric Effect of Bone,” *Journal of the Physical Society of Japan*, vol. 12, no. 10, pp. 1158–1162, Oct. 1957, doi: 10.1143/JPSJ.12.1158.

[41] D. Khare, B. Basu, and A. K. Dubey, “Electrical stimulation and piezoelectric biomaterials for bone tissue engineering applications,” *Biomaterials*, vol. 258, p. 120280, Nov. 2020, doi: 10.1016/J.BIOMATERIALS.2020.120280.

[42] F. Lucarelli, S. Tombelli, M. Minunni, G. Marrazza, and M. Mascini, “Electrochemical and piezoelectric DNA biosensors for hybridisation detection,” *Analytica Chimica Acta*, vol. 609, no. 2, pp. 139–159, Feb. 2008, doi: 10.1016/J.ACA.2007.12.035.

[43] A. L. Kholkin, N. A. Pertsev, and A. v. Goltsev, “Piezoelectricity and Crystal Symmetry,” *Piezoelectric and Acoustic Materials for Transducer Applications*, pp. 17–38, 2008, doi: 10.1007/978-0-387-76540-2_2.

[44] A. V. Carazo, “Piezoelectric Transformers: An Historical Review,” *Actuators 2016, Vol. 5, Page 12*, vol. 5, no. 2, p. 12, Apr. 2016, doi: 10.3390/ACT5020012.

[45] M. M. Vijatović, J. D. Bobić, and B. D. Stojanović, “History and challenges of barium titanate: Part I,” *Science of Sintering*, vol. 40, no. 2, pp. 155–165, 2008, doi: 10.2298/SOS0802155V.

[46] C. H. Allen, “A Small High Frequency Barium Titanate Microphone,” *J Acoust Soc Am*, vol. 22, no. 1, pp. 85–85, Jan. 1950, doi: 10.1121/1.1917156.

[47] X. Xing, X. Zhu, and J. Li, “Structure of Pb(Zr,Ti)O3(PZT) for Power Ultrasonic Transducer,” *Journal of Wuhan University of Technology-Mater. Sci. Ed. 2018 33:4*, vol. 33, no. 4, pp. 884–887, Jul. 2018, doi: 10.1007/S11595-018-1908-7.

[48] G. H. Haertling, “Ferroelectric Ceramics: History and Technology,” *Journal of the American Ceramic Society*, vol. 82, no. 4, pp. 797–818, Apr. 1999, doi: 10.1111/J.1151-2916.1999.TB01840.X.

[49] M. Siddiqui, J. J. Mohamed, and Z. A. Ahmad, “Structural, piezoelectric, and dielectric properties of PZT-based ceramics without excess lead oxide,” *Journal of the Australian Ceramic Society*, vol. 56, no. 2, pp. 371–377, Jun. 2020, doi: 10.1007/S41779-019-00337-3/FIGURES/5.

[50] R. Liang and Q. M. Wang, “High sensitivity piezoelectric sensors using flexible PZT thick-film for shock tube pressure testing,” *Sensors and Actuators A: Physical*, vol. 235, pp. 317–327, Nov. 2015, doi: 10.1016/J.SNA.2015.09.027.

[51] S. Watanabe, T. Fujiu, and T. Fujii, “PZT thin film actuator/sensor for atomic force microscope,” *IEEE International Symposium on Applications of Ferroelectrics*, vol. 1, pp. 199–204, 1996, doi: 10.1109/ISAF.1996.602735.

[52] M. G. Kang, W. S. Jung, C. Y. Kang, and S. J. Yoon, “Recent Progress on PZT Based Piezoelectric Energy Harvesting Technologies,” *Actuators 2016, Vol. 5, Page 5*, vol. 5, no. 1, p. 5, Feb. 2016, doi: 10.3390/ACT5010005.

[53] R. K. Gohite and M. Gohite, “Generation of electricity thorough PZT materials with the help footfall stress Introduction,” *International Journal Of Core Engineering & Management (IJCEM)*, vol. 1, no. 5, 2014.

[54] “Piezoelectricity From Dancing.” http://large.stanford.edu/courses/2010/ph240/winger1/ (accessed Mar. 27, 2022).

[55] M. Lukacs, M. Sayer, D. Knapik, R. Candela, and F. S. Foster, “Novel PZT films for ultrasound biomicroscopy,” *Proceedings of the IEEE Ultrasonics Symposium*, vol. 2, pp. 901–904, 1996, doi: 10.1109/ULTSYM.1996.584138.

[56] J. S. Pulskamp *et al.*, “Piezoelectric PZT MEMS technologies for small-scale robotics and RF applications,” *MRS Bulletin*, vol. 37, no. 11, pp. 1062–1070, Nov. 2012, doi: 10.1557/MRS.2012.269.

[57] P. H. Cazorla *et al.*, “Piezoelectric Micro-pump with PZT Thin Film for Low Consumption Microfluidic Devices,” *Procedia Engineering*, vol. 87, pp. 488–491, Jan. 2014, doi: 10.1016/J.PROENG.2014.11.402.

[58] M. Esquivel-Gaon *et al.*, “Bismuth-based nanoparticles as the environmentally friendly replacement for lead-based piezoelectrics,” *RSC Advances*, vol. 5, no. 35, pp. 27295–27304, Mar. 2015, doi: 10.1039/C5RA02151K.

[59] M. D. Maeder, D. Damjanovic, and N. Setter, “Lead Free Piezoelectric Materials,” *Journal of Electroceramics 2004 13:1*, vol. 13, no. 1, pp. 385–392, Jul. 2004, doi: 10.1007/S10832-004-5130-Y.

[60] H. Wei *et al.*, “An overview of lead-free piezoelectric materials and devices,” *Journal of Materials Chemistry C*, vol. 6, no. 46, pp. 12446–12467, Nov. 2018, doi: 10.1039/C8TC04515A.

[61] P. K. Panda, “Review: Environmental friendly lead-free piezoelectric materials,” *Journal of Materials Science*, vol. 44, no. 19, pp. 5049–5062, Oct. 2009, doi: 10.1007/S10853-009-3643-0/TABLES/15.

[62] D. Zhu *et al.*, “Integrated photonics on thin-film lithium niobate,” *Advances in Optics and Photonics, Vol. 13, Issue 2, pp. 242-352*, vol. 13, no. 2, pp. 242–352, Jun. 2021, doi: 10.1364/AOP.411024.

[63] Lord Rayleigh, “On waves propagated along the plane surface of an elastic solid,” *Proceedings of the London Mathematical Society*, vol. s1-17, no. 1, pp. 4–11, 1885, doi: 10.1112/PLMS/S1-17.1.4.

[64] R. M. White and F. W. Voltmer, “DIRECT PIEZOELECTRIC COUPLING TO SURFACE ELASTIC WAVES,” *Applied Physics Letters*, vol. 7, no. 12, p. 314, Nov. 1965, doi: 10.1063/1.1754276.

[65] M. J. Vellekoop, “Acoustic wave sensors and their technology,” *Ultrasonics*, vol. 36, no. 1–5, pp. 7–14, Feb. 1998, doi: 10.1016/S0041-624X(97)00146-7.

[66] R. C. Williamson, “CASE STUDIES OF SUCCESSFUL SURFACE-ACOUSTIC-WAVE DEVICES.,” *1977 Ultrasonics Symposium*, pp. 460–468, 1977, doi: 10.1109/ULTSYM.1977.196880.

[67] C. S. Hartmann, “Systems Impact of Modern Rayleigh Wave Technology,” pp. 238–253, 1985, doi: 10.1007/978-3-642-82621-4_17.

[68] C. Campbell, *Surface Acoustic Wave Devices and their Signal Processing Applications*. Elsevier, 1989. doi: 10.1016/B978-0-12-157345-4.X5001-2.

[69] L. T. de Bell and R. C. M. Li, "Surface-Acoustic-Wave Resonators," *Proceedings of the IEEE*, vol. 64, no. 5, pp. 711–721, 1976, doi: 10.1109/PROC.1976.10200.

[70] M. Farré, L. Kantiani, and D. Barceló, "Microfluidic Devices: Biosensors," *Chemical Analysis of Food: Techniques and Applications*, pp. 177–217, 2012, doi: 10.1016/B978-0-12-384862-8.00007-8.

[71] S. Shiokawa, Y. Matsui, and T. Moriizumi, "Experimental study on liquid streaming by SAW," *Japanese Journal of Applied Physics*, vol. 28, no. S1, pp. 126–128, Jan. 1989, doi: 10.7567/JJAPS.28S1.126/XML.

[72] J. H. Jung, G. Destgeer, B. Ha, J. Park, and H. J. Sung, "On-demand droplet splitting using surface acoustic waves," *Lab on a Chip*, vol. 16, no. 17, pp. 3235–3243, Aug. 2016, doi: 10.1039/C6LC00648E.

[73] Y. Wang *et al.*, "A rapid and controllable acoustothermal microheater using thin film surface acoustic waves," *Sensors and Actuators A: Physical*, vol. 318, p. 112508, Feb. 2021, doi: 10.1016/J.SNA.2020.112508.

[74] Y. Wang *et al.*, "A rapid and controllable acoustothermal microheater using thin film surface acoustic waves," *Sensors and Actuators, A: Physical*, vol. 318, p. 112508, Feb. 2021, doi: 10.1016/j.sna.2020.112508.

[75] S. Li, F. Ma, H. Bachman, C. E. Cameron, X. Zeng, and T. J. Huang, "Acoustofluidic bacteria separation," *Journal of Micromechanics and Microengineering*, vol. 27, no. 1, p. 015031, Jan. 2017, doi: 10.1088/1361-6439/27/1/015031.

[76] T. D. Luong, V. N. Phan, and N. T. Nguyen, “High-throughput micromixers based on acoustic streaming induced by surface acoustic wave,” *Microfluidics and Nanofluidics*, vol. 10, no. 3, pp. 619–625, Mar. 2011, doi: 10.1007/S10404-010-0694-0/FIGURES/8.

[77] W. K. Tseng, J. L. Lin, W. C. Sung, S. H. Chen, and G. bin Lee, “Active micro-mixers using surface acoustic waves on Y-cut 128° LiNbO3,” *Journal of Micromechanics and Microengineering*, vol. 16, no. 3, p. 539, Feb. 2006, doi: 10.1088/0960-1317/16/3/009.

[78] H. Bachman *et al.*, “Acoustofluidic devices controlled by cell phones,” *Lab on a Chip*, vol. 18, no. 3, pp. 433–441, 2018, doi: 10.1039/c7lc01222e.

[79] J. Bennès *et al.*, “Detection and high-precision positioning of liquid droplets using SAW systems,” *IEEE Transactions on Ultrasonics, Ferroelectrics, and Frequency Control*, vol. 54, no. 10, pp. 2146–2151, 2007, doi: 10.1109/TUFFC.2007.510.

[80] R. Tao *et al.*, “Hierarchical nanotexturing enables acoustofluidics on slippery yet sticky, flexible surfaces,” *Nano Letters*, vol. 20, no. 5, pp. 3263–3270, May 2020, doi: 10.1021/acs.nanolett.0c00005.

[81] J. Zhang *et al.*, “Surface acoustic waves enable rotational manipulation of Caenorhabditis elegans,” *Lab on a Chip*, vol. 19, no. 6, pp. 984–992, Mar. 2019, doi: 10.1039/C8LC01012A.

[82] K. Wang *et al.*, “Sorting of tumour cells in a microfluidic device by multi-stage surface acoustic waves,” *Sensors and Actuators, B: Chemical*, vol. 258, pp. 1174–1183, Apr. 2018, doi: 10.1016/j.snb.2017.12.013.

[83] B. Hu *et al.*, “Fabrications of L-band LiNbO3-based SAW resonators for aerospace applications,” *Micromachines (Basel)*, vol. 10, no. 6, Jun. 2019, doi: 10.3390/mi10060349.

[84] R. Tao *et al.*, “Bimorph material/structure designs for high sensitivity flexible surface acoustic wave temperature sensors,” *Scientific Reports*, vol. 8, no. 1, pp. 1–9, 2018, doi: 10.1038/s41598-018-27324-1.

[85] X. Ye, Q. Wang, L. Fang, X. Wang, and B. Liang, “Comparative study of SAW temperature sensor based on different piezoelectric materials and crystal cuts for passive wireless measurement,” in *Proceedings of IEEE Sensors*, 2010, pp. 585–588. doi: 10.1109/ICSENS.2010.5690462.

[86] S. Shiokawa and J. Kondoh, “Surface acoustic wave sensors,” *Japanese Journal of Applied Physics, Part 1: Regular Papers and Short Notes and Review Papers*, vol. 43, no. 5 B, pp. 2799–2802, 2004, doi: 10.1143/JJAP.43.2799.

[87] X. L. He *et al.*, “High sensitivity humidity sensors using flexible surface acoustic wave devices made on nanocrystalline ZnO/polyimide substrates,” *Journal of Materials Chemistry C*, vol. 1, no. 39, pp. 6210–6215, 2013, doi: 10.1039/c3tc31126k.

[88] H. Dong, D. Li, J. Pang, Q. Zhang, and J. Xie, “Highly Sensitive and Fast-Response Humidity Sensor Based on Saw Resonator and MoS for Human Activity Detection,” *Proceedings of the IEEE International Conference on Micro Electro Mechanical Systems (MEMS)*, vol. 2021-January, pp. 322–325, Jan. 2021, doi: 10.1109/MEMS51782.2021.9375370.

[89] E. Howe and G. Harding, “A comparison of protocols for the optimisation of detection of bacteria using a surface acoustic wave (SAW) biosensor,” 2000. [Online]. Available: www.elsevier.com/locate/bios

[90] K. Länge, B. E. Rapp, and M. Rapp, “Surface acoustic wave biosensors: A review,” *Analytical and Bioanalytical Chemistry*, vol. 391, no. 5. pp. 1509–1519, Jul. 2008. doi: 10.1007/s00216-008-1911-5.

[91] X. Y. Du, Y. Q. Fu, J. K. Luo, A. J. Flewitt, and W. I. Milne, “Microfluidic pumps employing surface acoustic waves generated in ZnO thin films,” *Journal of Applied Physics*, vol. 105, no. 2, p. 024508, Jan. 2009, doi: 10.1063/1.3068326.

[92] H. pang, j. K. Luo, and Y. Q. Fu, “Zno Thin Films and Nanostructures for Acoustic Wave-Based Microfluidic and Sensing Applications,” *Functional Materials and Electronics*, pp. 195–262, May 2018, doi: 10.1201/9781315167367-5.

[93] “Availability - ZINC Sustainability.” https://sustainability.zinc.org/availability/ (accessed Jul. 26, 2022).

[94] “What is software development? | IBM.” https://www.ibm.com/topics/software-development (accessed Nov. 16, 2021).

[95] N. Wirth, “A Brief History of Software Engineering,” *IEEE Annals of the History of Computing*, vol. 30, no. 3, pp. 32–39, 2008, doi: 10.1109/MAHC.2008.33.

[96] B. Perens and M. Sroka, “The Open Source Definition,” 2007.

[97] Python Software Foundation, “What is Python? Executive Summary | Python.org.” https://www.python.org/doc/essays/blurb/ (accessed Dec. 10, 2021).

[98] D. Phillips, *Python 3 Object-Oriented Programming Third Edition*. 2000.

[99] T. E. Oliphant, “Python for scientific computing,” *Computing in Science and Engineering*, vol. 9, no. 3, pp. 10–20, May 2007, doi: 10.1109/MCSE.2007.58.

[100] A. Spizhevoy and A. Rybnikov, *OpenCV 3 Computer Vision*. 2018.

[101] Y. (Hayden) Liu, *Python Machine Learning By Example*, vol. 91. 2017.

[102] “os — Miscellaneous operating system interfaces — Python 3.10.4 documentation.” https://docs.python.org/3/library/os.html (accessed Mar. 25, 2022).

[103] “RPi.GPIO · PyPI.” https://pypi.org/project/RPi.GPIO/ (accessed Mar. 25, 2022).

[104] Www.kivy.org, “Kivy Documentation,” 2012. https://kivy.org/doc/stable/

[105] “time — Time access and conversions — Python 3.10.4 documentation.” https://docs.python.org/3/library/time.html (accessed Mar. 25, 2022).

[106] “datetime — Basic date and time types — Python 3.10.4 documentation.” https://docs.python.org/3/library/datetime.html (accessed Mar. 25, 2022).

[107] “Welcome to pySerial’s documentation — pySerial 3.4 documentation.” https://pyserial.readthedocs.io/en/latest/ (accessed Mar. 25, 2022).

[108] “PyVISA · PyPI.” https://pypi.org/project/PyVISA/ (accessed Mar. 25, 2022).

[109] “simple-pid · PyPI.” https://pypi.org/project/simple-pid/ (accessed Mar. 25, 2022).

[110] “OpenPIV | openpiv-python.” http://www.openpiv.net/openpiv-python/ (accessed Mar. 25, 2022).

[111] “Pillow · PyPI.” https://pypi.org/project/Pillow/ (accessed Mar. 25, 2022).

[112] “NumPy.” https://numpy.org/ (accessed Mar. 25, 2022).

[113] “Matplotlib — Visualization with Python.” https://matplotlib.org/ (accessed Mar. 25, 2022).

[114] “pickle — Python object serialization — Python 3.10.4 documentation.” https://docs.python.org/3/library/pickle.html (accessed Mar. 25, 2022).

[115] “GitHub - groupgets/pylepton: Quick and dirty pure python library for interfacing with FLIR lepton.” https://github.com/groupgets/pylepton (accessed Mar. 25, 2022).

[116] “sys — System-specific parameters and functions — Python 3.10.4 documentation.” https://docs.python.org/3/library/sys.html (accessed Mar. 25, 2022).

[117] “decimal — Decimal fixed point and floating point arithmetic — Python 3.10.4 documentation.” https://docs.python.org/3/library/decimal.html (accessed Mar. 25, 2022).

[118] “threading — Thread-based parallelism — Python 3.10.4 documentation.” https://docs.python.org/3/library/threading.html (accessed Mar. 25, 2022).

[119] “picamera — Picamera 1.13 Documentation.” https://picamera.readthedocs.io/en/release-1.13/ (accessed Mar. 25, 2022).

[120] “pynput · PyPI.” https://pypi.org/project/pynput/ (accessed Mar. 25, 2022).

[121] “collections — Container datatypes — Python 3.10.4 documentation.” https://docs.python.org/3/library/collections.html (accessed Mar. 25, 2022).

[122] “math — Mathematical functions — Python 3.10.4 documentation.” https://docs.python.org/3/library/math.html (accessed Mar. 25, 2022).

[123] “GitHub - PyImageSearch/imutils: A series of convenience functions to make basic image processing operations such as translation, rotation, resizing, skeletonization,

and displaying Matplotlib images easier with OpenCV and Python." https://github.com/PyImageSearch/imutils (accessed Mar. 25, 2022).

[124] "argparse — Parser for command-line options, arguments and sub-commands — Python 3.10.4 documentation." https://docs.python.org/3/library/argparse.html (accessed Mar. 25, 2022).

[125] A. Tatnall, "HISTORY OF COMPUTER HARDWARE AND SOFTWARE DEVELOPMENT".

[126] J. M. Pearce, "Laboratory equipment: Cut costs with open-source hardware," *Nature*, vol. 505, no. 7485. Nature Publishing Group, p. 618, Jan. 29, 2014. doi: 10.1038/505618d.

[127] B. Wijnen, E. J. Hunt, G. C. Anzalone, and J. M. Pearce, "Open-source syringe pump library," *PLoS ONE*, vol. 9, no. 9, pp. 1–8, 2014, doi: 10.1371/journal.pone.0107216.

[128] J. Coburn, "Raspberry Pi History," *Build Your Own Car Dashboard with a Raspberry Pi*, pp. 1–12, 2020, doi: 10.1007/978-1-4842-6080-7_1.

[129] "Raspberry Pi Foundation - About Us." https://www.raspberrypi.org/about/ (accessed Mar. 28, 2022).

[130] A. K. Dennis, "Raspberry Pi Home Automation with Arduino Automate your home with a set of exciting projects for the Raspberry Pi!," 2013, Accessed: Dec. 10, 2021. [Online]. Available: www.it-ebooks.info

[131] Dr. S. L. Fernandes, *Raspberry Pi 3 Cookbook for Python Programmers*. 2018.

[132] G. En, U. S. B. Cc, V. I. N. Ldo, and V. I. N. Ldo, "Raspberry Pi 4 Model B Schematic, Revision 4.0," 2018.

[133] “MIPI Overview.” https://www.mipi.org/about-us (accessed Sep. 06, 2019).

[134] “Raspberry Pi Documentation - Raspberry Pi OS.” https://www.raspberrypi.com/documentation/computers/os.html (accessed Nov. 22, 2021).

[135] C. Edwards, “Not-so-humble Raspberry Pi gets big ideas,” *Engineering and Technology*, vol. 8, no. 3, pp. 30–33, Apr. 2013, doi: 10.1049/ET.2013.0301.

[136] “The life of Pi: Ten years of Raspberry Pi.” https://www.cam.ac.uk/stories/raspberrypi (accessed Apr. 02, 2022).

[137] S. Pandit *et al.*, “IOT BASED INDUSTRY AUTOMATION USING RASPBERRY PI,” vol. 2020, doi: 10.17485/ijst/2016/v9i39/90414.

[138] C. Wai Zhao, J. Jegatheesan, and S. Chee Loon, “Exploring IOT Application Using Raspberry Pi,” *International Journal of Computer Networks and Applications*, vol. 2, no. 1, Accessed: Apr. 02, 2022. [Online]. Available: http://www.digi.com

[139] “Raspberry Pi for industry – Raspberry Pi.” https://www.raspberrypi.com/for-industry/ (accessed Apr. 02, 2022).

[140] “Buy a Compute Module 4 – Raspberry Pi.” https://www.raspberrypi.com/products/compute-module-4/?variant=raspberry-pi-cm4001000 (accessed Mar. 28, 2022).

[141] W. Watanabe, R. Maruyama, H. Arimoto, and Y. Tamada, “Low-cost multi-modal microscope using Raspberry Pi,” *Optik (Stuttg)*, vol. 212, p. 164713, Jun. 2020, doi: 10.1016/J.IJLEO.2020.164713.

[142] A. Maia Chagas, L. L. Prieto-Godino, A. B. Arrenberg, and T. Baden, “The €100 lab: A 3D-printable open-source platform for fluorescence microscopy, optogenetics, and

accurate temperature control during behaviour of zebrafish, Drosophila, and Caenorhabditis elegans," *PLOS Biology*, vol. 15, no. 7, p. e2002702, Jul. 2017, doi: 10.1371/journal.pbio.2002702.

[143] T. Aidukas, R. Eckert, A. R. Harvey, L. Waller, and P. C. Konda, "Low-cost, sub-micron resolution, wide-field computational microscopy using opensource hardware," *Scientific Reports 2019 9:1*, vol. 9, no. 1, pp. 1–12, May 2019, doi: 10.1038/s41598-019-43845-9.

[144] Y. Temiz, "The lego microscope: A valuable lab tool began as a diy project - [Hands on]," *IEEE Spectrum*, vol. 57, no. 5, pp. 16–18, May 2020, doi: 10.1109/MSPEC.2020.9078448.

[145] M. Liu, Z. Tang, H. Monshat, Y. Zhao, and M. Lu, "Portable instrument for paper-based isothermal nucleic acid amplification tests," vol. 1, no. c, pp. 1–3.

[146] A. Marzo, T. Corkett, and B. W. Drinkwater, "Ultraino: An Open Phased-Array System for Narrowband Airborne Ultrasound Transmission," *IEEE Transactions on Ultrasonics, Ferroelectrics, and Frequency Control*, vol. 65, no. 1, pp. 102–111, Jan. 2018, doi: 10.1109/TUFFC.2017.2769399.

[147] H. Bachman *et al.*, "Open source acoustofluidics," *Lab on a Chip*, vol. 19, no. 14, pp. 2404–2414, 2019, doi: 10.1039/c9lc00340a.

[148] A. Huang *et al.*, "Practical microcircuits for handheld acoustofluidics," *Lab on a Chip*, pp. 1352–1363, 2021, doi: 10.1039/d0lc01008a.

[149] J. Matouš, A. Kollarčik, M. Gurtner, T. Michálek, and Z. Hurák, "Optimization-based feedback manipulation through an array of ultrasonic transducers," in *IFAC-*

PapersOnLine, Sep. 2019, vol. 52, no. 15, pp. 483–488. doi: 10.1016/j.ifacol.2019.11.722.

[150] H. Fangohr, "A Comparison of C, MATLAB, and Python as Teaching Languages in Engineering," *Lecture Notes in Computer Science (including subseries Lecture Notes in Artificial Intelligence and Lecture Notes in Bioinformatics)*, vol. 3039, pp. 1210–1217, 2004, doi: 10.1007/978-3-540-25944-2_157.

[151] F. B. Serum, "Cell line profile C2C12 (ECACC catalogue no . 91031101)," vol. 12, no. 91031101, pp. 5–6, 1977.

[152] L. Liaw *et al.*, "The Adhesive and Migratory Effects of Osteopontin Are Mediated via Distinct Cell Surface Integrins Role of av433 in Smooth Muscle Cell Migration to Osteopontin In Vitro."

[153] L. E. Tracy, R. A. Minasian, and E. J. Caterson, "Extracellular Matrix and Dermal Fibroblast Function in the Healing Wound," *Advances in Wound Care*, vol. 5, no. 3, pp. 119–136, Mar. 2016, doi: 10.1089/WOUND.2014.0561.

[154] Y. Hassan and L. T. L. Than, "Loop-Mediated Isothermal Amplification (LAMP): Comparative Advances over Conventional PCR and Other Molecular Techniques," *Annual Research & Review in Biology*, vol. 35, no. 8, pp. 33–44, Aug. 2020, doi: 10.9734/arrb/2020/v35i830257.

[155] A. Raghunathan, H. R. Ferguson, C. J. Bornarth, W. Song, M. Driscoll, and R. S. Lasken, "Genomic DNA Amplification from a Single Bacterium," *APPLIED AND ENVIRONMENTAL MICROBIOLOGY*, vol. 71, no. 6, pp. 3342–3347, 2005, doi: 10.1128/AEM.71.6.3342-3347.2005.

[156] A. Barakat *et al.*, "Diagnostic testing for SARS-CoV-2," 2020.

[157] B. Schermer *et al.*, “Rapid SARS-CoV-2 testing in primary material based on a novel multiplex RT-LAMP assay,” *PLOS ONE*, vol. 15, no. 11, p. e0238612, Nov. 2020, doi: 10.1371/JOURNAL.PONE.0238612.

[158] A. Evrard, N. Boulle, and G. s Lutfalla, “Real-Time PCR,” in *Boisseau P., Houdy P., Lahmani M. (eds) Nanoscience*, Springer, Berlin, Heidelberg, 2009, pp. 841–869. doi: 10.1007/978-3-540-88633-4_15.

[159] T. J. Moehling, G. Choi, L. C. Dugan, M. Salit, and R. J. Meagher, “LAMP Diagnostics at the Point of Care: Emerging Trends and Perspectives for the Developer Community,” *Expert Review of Molecular Diagnostics*, p. 14737159.2021.1873769, Jan. 2021, doi: 10.1080/14737159.2021.1873769.

[160] “Peltiers in PCR matter! - Eppendorf Handling Solutions.” https://handling-solutions.eppendorf.com/sample-handling/amplification/productivity/detailview-productivity/news/peltiers-in-pcr-matter/ (accessed Aug. 22, 2022).

[161] T. Notomi *et al.*, “Loop-mediated isothermal amplification of DNA.,” *Nucleic Acids Res*, vol. 28, no. 12, p. 63, Jun. 2000, doi: 10.1093/nar/28.12.e63.

[162] M. C. Giuffrida and G. Spoto, “Integration of isothermal amplification methods in microfluidic devices: Recent advances,” *Biosensors and Bioelectronics*, vol. 90. Elsevier Ltd, pp. 174–186, Apr. 15, 2017. doi: 10.1016/j.bios.2016.11.045.

[163] J. Reboud *et al.*, “Shaping acoustic fields as a toolset for microfluidic manipulations in diagnostic technologies,” *Proc Natl Acad Sci U S A*, vol. 109, no. 38, pp. 15162–15167, Sep. 2012, doi: 10.1073/pnas.1206055109.

[164] G. Xu, R. N. Gunson, J. M. Cooper, and J. Reboud, “Rapid ultrasonic isothermal amplification of DNA with multiplexed melting analysis-applications in the clinical

diagnosis of sexually transmitted diseases," *Chemical Communications*, vol. 51, no. 13, pp. 2589–2592, Feb. 2015, doi: 10.1039/c4cc08389j.

[165] G. Papadakis *et al.*, "3D-printed Point-of-Care Platform for Genetic Testing of Infectious Diseases Directly in Human Samples Using Acoustic Sensors and a Smartphone," *ACS Sensors*, vol. 4, no. 5, pp. 1329–1336, 2019, doi: 10.1021/acssensors.9b00264.

[166] K. Tsougeni *et al.*, "Lab-on-Chip platform and protocol for rapid foodborne pathogen detection comprising on-chip cell capture, lysis, DNA amplification and surface-acoustic-wave detection," *Sensors and Actuators, B: Chemical*, vol. 320, p. 128345, Oct. 2020, doi: 10.1016/j.snb.2020.128345.

[167] Z. Ramshani *et al.*, "Extracellular vesicle microRNA quantification from plasma using an integrated microfluidic device", doi: 10.1038/s42003-019-0435-1.

[168] H. Zhang, Y. Xu, Z. Fohlerova, H. Chang, C. Iliescu, and P. Neuzil, "LAMP-on-a-chip: Revising microfluidic platforms for loop-mediated DNA amplification," *TrAC - Trends in Analytical Chemistry*, vol. 113. Elsevier B.V., pp. 44–53, Apr. 01, 2019. doi: 10.1016/j.trac.2019.01.015.

[169] J. Hill *et al.*, "Loop-mediated isothermal amplification assay for rapid detection of common strains of Escherichia coli," *Journal of Clinical Microbiology*, vol. 46, no. 8, pp. 2800–2804, Aug. 2008, doi: 10.1128/JCM.00152-08.

[170] J. R. Lakowicz, "Introduction to Fluorescence," *Principles of Fluorescence Spectroscopy*, pp. 1–23, 1999, doi: 10.1007/978-1-4757-3061-6_1.

[171] Invitrogen, "SYBR ® Green I Nucleic Acid Gel Stain - Useful Tips," *Molecular probes*, pp. 1–5, 2003.

[172] Invitrogen, “Propidium Iodide Nucleic Acid Stain,” 2006.

[173] F. Q. Al-Khalidi, R. Saatchi, D. Burke, H. Elphick, and S. Tan, “Respiration rate monitoring methods: A review,” *Pediatric Pulmonology*, vol. 46, no. 6, pp. 523–529, Jun. 2011, doi: 10.1002/PPUL.21416.

[174] P. H. Charlton *et al.*, “Breathing Rate Estimation from the Electrocardiogram and Photoplethysmogram: A Review,” *IEEE Reviews in Biomedical Engineering*, vol. 11, pp. 2–20, Oct. 2018, doi: 10.1109/RBME.2017.2763681.

[175] N. Sadr and P. de Chazal, “A comparison of three ECG-derived respiration methods for sleep apnoea detection,” *Biomedical Physics & Engineering Express*, vol. 5, no. 2, p. 025027, Jan. 2019, doi: 10.1088/2057-1976/AAFC80.

[176] P. J. Strollo and R. M. Rogers, “Obstructive Sleep Apnea,” *New England Journal of Medicine*, vol. 334, no. 2, pp. 99–104, Jan. 1996, doi: 10.1056/NEJM199601113340207.

[177] “Hyperventilation | Johns Hopkins Medicine.” https://www.hopkinsmedicine.org/health/conditions-and-diseases/hyperventilation (accessed Mar. 28, 2022).

[178] D. Fan *et al.*, “Breathing rhythm analysis in body centric networks,” *IEEE Access*, vol. 6, pp. 32507–32513, Jun. 2018, doi: 10.1109/ACCESS.2018.2846605.

[179] T. Young, M. Palta, J. Dempsey, J. Skatrud, S. Weber, and S. Badr, “The Occurrence of Sleep-Disordered Breathing among Middle-Aged Adults,” *New England Journal of Medicine*, vol. 328, no. 17, pp. 1230–1235, Apr. 1993, doi: 10.1056/nejm199304293281704.

[180] D. J. Eckert, A. S. Jordan, P. Merchia, and A. Malhotra, “Central sleep apnea: Pathophysiology and treatment,” *Chest*, vol. 131, no. 2, pp. 595–607, 2007, doi: 10.1378/chest.06.2287.

[181] A. Crivello, P. Barsocchi, M. Girolami, and F. Palumbo, “The Meaning of Sleep Quality: A Survey of Available Technologies,” *IEEE Access*, vol. 7, pp. 167374–167390, 2019, doi: 10.1109/ACCESS.2019.2953835.

[182] H. Zhang *et al.*, “Waist-wearable wireless respiration sensor based on triboelectric effect,” *Nano Energy*, vol. 59, pp. 75–83, May 2019, doi: 10.1016/J.NANOEN.2019.01.063.

[183] S. Kwon, H. Kim, and W. H. Yeo, “Recent advances in wearable sensors and portable electronics for sleep monitoring,” *iScience*, vol. 24, no. 5, p. 102461, May 2021, doi: 10.1016/J.ISCI.2021.102461.

[184] S. Ahmadzadeh, J. Luo, and R. Wiffen, “Review on Biomedical Sensors, Technologies and Algorithms for Diagnosis of Sleep Disordered Breathing: Comprehensive Survey,” *IEEE Reviews in Biomedical Engineering*, vol. 15, pp. 4–22, 2022, doi: 10.1109/RBME.2020.3033930.

[185] B. Feng, K. Zhao, Q. Su, Z. Yu, and H. Jin, “Passive wireless respiratory sensor,” *Electronics Letters*, vol. 57, no. 19, pp. 730–731, Sep. 2021, doi: 10.1049/ELL2.12248.

[186] M. van Gastel, S. Stuijk, S. Overeem, J. P. van Dijk, M. M. van Gilst, and G. de Haan, “Camera-Based Vital Signs Monitoring during Sleep - A Proof of Concept Study,” *IEEE Journal of Biomedical and Health Informatics*, vol. 25, no. 5, pp. 1409–1418, May 2021, doi: 10.1109/JBHI.2020.3045859.

[187] J. Allen, “Photoplethysmography and its application in clinical physiological measurement,” *Physiological Measurement*, vol. 28, no. 3, p. R1, Feb. 2007, doi: 10.1088/0967-3334/28/3/R01.

[188] H. Jin *et al.*, “Flexible surface acoustic wave respiration sensor for monitoring obstructive sleep apnea syndrome,” *Journal of Micromechanics and Microengineering*, vol. 27, no. 11, p. 115006, Oct. 2017, doi: 10.1088/1361-6439/aa8ae0.

[189] X. Tao *et al.*, “Three-Dimensional Tetrapodal ZnO Microstructured Network Based Flexible Surface Acoustic Wave Device for Ultraviolet and Respiration Monitoring Applications,” *ACS Applied Nano Materials*, vol. 3, no. 2, pp. 1468–1478, 2020, doi: 10.1021/acsanm.9b02300.

[190] X. Tao *et al.*, “Three-Dimensional Tetrapodal ZnO Microstructured Network Based Flexible Surface Acoustic Wave Device for Ultraviolet and Respiration Monitoring Applications,” *ACS Applied Nano Materials*, vol. 3, no. 2, pp. 1468–1478, Feb. 2020, doi: 10.1021/ACSANM.9B02300/SUPPL_FILE/AN9B02300_SI_001.PDF.

[191] J. Vernon *et al.*, “Acousto-Pi: An Opto-Acoustofluidic System using Surface Acoustic Waves controlled with Open Source Electronics for Integrated In-Field Diagnostics,” *IEEE Transactions on Ultrasonics, Ferroelectrics, and Frequency Control*, pp. 1–1, 2021, doi: 10.1109/TUFFC.2021.3113173.

[192] J. Vernon, P. Canyelles-Pericas, H. Torun, R. Binns, W. P. Ng, and Y. Q. Fu, “Apnoea-Pi: Sleep disorder monitoring with open-source electronics and acoustics,” 2021. doi: 10.23919/ICAC50006.2021.9594073.

[193] “S-Parameter - MATLAB & Simulink.” https://uk.mathworks.com/discovery/s-parameter.html (accessed Aug. 09, 2022).

[194] P. J. Pupalaikis, *S-parameters for signal integrity*.

[195] J. F. Henriques, R. Caseiro, P. Martins, and J. Batista, “High-speed tracking with kernelized correlation filters,” *IEEE Transactions on Pattern Analysis and Machine Intelligence*, vol. 37, no. 3, pp. 583–596, 2015, doi: 10.1109/TPAMI.2014.2345390.

[196] S. Varagnolo, G. Mistura, M. Pierno, and M. Sbragaglia, “Sliding droplets of Xanthan solutions: A joint experimental and numerical study,” *European Physical Journal E*, vol. 38, no. 11, pp. 1–8, 2015, doi: 10.1140/epje/i2015-15126-0.

[197] J. Reboud *et al.*, “Shaping acoustic fields as a toolset for microfluidic manipulations in diagnostic technologies”, doi: 10.1073/pnas.1206055109/-/DCSupplemental.

[198] ATCC, “C2C12 (ATCC® CRL-1772™).”

[199] Z. Guttenberg *et al.*, “Planar chip device for PCR and hybridization with surface acoustic wave pump,” *Lab on a Chip*, vol. 5, no. 3, pp. 308–317, Feb. 2005, doi: 10.1039/B412712A.

[200] W. S. Mielczarek, E. A. Obaje, T. T. Bachmann, and M. Kersaudy-Kerhoas, “Microfluidic blood plasma separation for medical diagnostics: is it worth it?,” *Lab on a Chip*, vol. 16, no. 18, pp. 3441–3448, Aug. 2016, doi: 10.1039/C6LC00833J.

[201] H. L. Ngo, H. D. Nguyen, V. N. Tran, and H. T. Ngo, “Development of a Low-Cost and Portable Real-Time PCR Machine for Developing Countries,” in *IFMBE Proceedings*, 2022, vol. 85, pp. 69–83. doi: 10.1007/978-3-030-75506-5_6.

[202] Y. Wang *et al.*, “Flexible/Bendable Acoustofluidics Based on Thin-Film Surface Acoustic Waves on Thin Aluminum Sheets,” *ACS Applied Materials and Interfaces*,

vol. 13, no. 14, pp. 16978–16986, Apr. 2021, doi: 10.1021/ACSAMI.0C22576/SUPPL_FILE/AM0C22576_SI_009.PDF.

[203] T. Liu, "Digital-output relative humidity & temperature sensor/module DHT22 (DHT22 also named as AM2302) Capacitive-type humidity and temperature module/sensor."

[204] J. M. Cowan, J. M. Burris, J. R. Hughes, and M. P. Cunningham, "The relationship of normal body temperature, end-expired breath temperature, and BAC/BrAC ratio in 98 physically fit human test subjects," *J Anal Toxicol*, vol. 34, no. 5, pp. 238–242, 2010, doi: 10.1093/JAT/34.5.238.

[205] S. Ahmad Hasan, "Flexible ZnO thin film-based surface acoustic wave devices for environmental and biomedical sensing applications," 2019.

[206] J. Wu *et al.*, "Ultrathin Glass-Based Flexible, Transparent, and Ultrasensitive Surface Acoustic Wave Humidity Sensor with ZnO Nanowires and Graphene Quantum Dots," *ACS Applied Materials and Interfaces*, vol. 12, no. 35, pp. 39817–39825, Sep. 2020, doi: 10.1021/ACSAMI.0C09962/SUPPL_FILE/AM0C09962_SI_001.PDF.

[207] J. Zhou *et al.*, "Transparent surface acoustic wave devices on Zno/Glass using Al-doped Zno as the electrode," *IEEE Electron Device Letters*, vol. 34, no. 10, pp. 1319–1321, 2013, doi: 10.1109/LED.2013.2276618.

[208] S. G. Mattyasovszky *et al.*, "Exposure to radial extracorporeal shock waves modulates viability and gene expression of human skeletal muscle cells: A controlled in vitro study," *Journal of Orthopaedic Surgery and Research*, vol. 13, no. 1, Apr. 2018, doi: 10.1186/s13018-018-0779-0.

[209] N. A. Dumont, C. F. Bentzinger, M. C. Sincennes, and M. A. Rudnicki, “Satellite cells and skeletal muscle regeneration,” *Compr Physiol*, vol. 5, no. 3, pp. 1027–1059, Jul. 2015, doi: 10.1002/cphy.c140068.

[210] G. R. Adams, “Satellite cell proliferation and skeletal muscle hypertrophy,” *Applied Physiology, Nutrition, and Metabolism*, vol. 31, no. 6, pp. 782–790, 2007, doi: 10.1139/h06-053.

[211] D. C. M. Simoes and I. Vogiatzis, “Can muscle protein metabolism be specifically targeted by exercise training in COPD?,” *Journal of Thoracic Disease*, vol. 10, no. Suppl 12, pp. S1367–S1376, 2018, doi: 10.21037/jtd.2018.02.67.